Facies-Based and Anhydrite-Controlled Petrophysical Properties of the Upper Clear Fork Formation in the Permian Basin in West Texas, USA

by:

Cody Line

Presented to the Faculty of the Graduate School of

The University of Texas at Arlington

of the Requirement for the Degree of

MASTER OF SCIENCE IN GEOLOGY

THE UNIVERSITY OF TEXAS AT ARLINGTON

May 2020

Acknowledgements

I would like to thank Dr. Qinhong Hu for his guidance throughout my graduate program at UTA. I would also like to thank my committee members, Drs. John Wickham and Matthew Loocke for their knowledge and support.

I would also like to thank Texland Petroleum for providing core samples and data for this research project, especially Jim Martin and Megan Loyd for all their assistance. I would like to thank Qiming Wang for his guidance in the lab. Finally, I would like to thank my family for their constant support and encouragement throughout my life.

Abstract

Facies-Based and Anhydrite-Controlled Petrophysical Properties of the Upper Clear Fork Formation in the Permian Basin of West Texas, USA

Cody Line, MS

The University of Texas at Arlington, 2020

Supervising Professor: Qinhong Hu

The Leonardian-aged dolomite of the upper Clear Fork Formation in the Palm Sunday field of West Texas exhibits a wide range of facies that vary during deposition due to environmental factors such as water depth, wave energy, salinity, and oxygen availability. Variations in facies and associated mineralogy play a role on the petrophysical characteristics such as porosity, permeability, and water absorption.

This study intends to provide a better understanding on the petrophysical properties of the upper Clear Fork by facies type. Seven core samples with different facies from two wells in the Palm Sunday field were tested to determine how the pore structure of each facies will affect fluid flow and hydrocarbon production. Laboratory experiments included x-ray diffraction (XRD) for minerology, TOC, pyrolysis, vacuum saturation for porosity, mercury intrusion capillary pressure (MICP) for pore structure characteristics, and imbibition and vapor absorption for fluid flow behavior; in addition vacuum saturation, liquid pycnometry, and imbibition-vapor absorption tests used two different fluids of hydrophilic and hydrophobic characteristics. XRD

analyses indicate all samples are composed of predominately dolomite and anhydrite with a minimal quartz content. Results show that all samples are organic-lean with TOC ranging from 0.04-0.51%. The sample taken from the massive carbonaceous mudstone facies exhibits the highest porosity at ~4% from both MICP and vacuum saturation, while the porosity from the other samples range from 0.24-3.57%. Dominant pore types from all samples are determined to be probably intergranular pores from MICP analyses with most pore-throat diameters in the 0.1-10 μm range. Low pore connectivity for most samples is determined from fluid imbibition. Well log analysis was performed to create curves for porosity, permeability, and water saturation. Porosity values from well log analyses match well with core analysis, however permeability and water saturation did not match as well.

Table of Contents

List of Figures

List of Tables

Nomenclature

BS: boundstone

cm: centimeters

DIW/ DI Water: deionized water

DT2: n-decane:toluene at 2:1 in volumetric ratio

Eq: Equation

GS: grainstone

Hr/Hrs: hours

MICP: mercury intrusion capillary pressure

m: meters

nm: nanometers

PS: packstone

sec: seconds

TOC: total organic carbon

WS: wackestone

XRD: X-ray diffraction

µm: micrometer

Chapter 1: Introduction

Existing carbonate reservoirs in the United States still hold large quantities of oil and gas, despite declining production rates. For these carbonate reservoirs, conventional data-collection methodologies may be insufficient for understanding the small-scale characteristics of these reservoirs. In particular, the Clear Fork reservoirs have exhibited a low-end recovery efficiency of all carbonate reservoirs in the Permian Basin of west Texas. At the time of discovery it is estimated that Leonardian reservoirs contains more than 14.5 billion barrels of oil yet have only accounted for more than 3.2 billion barrels of oil production putting the recovery efficiency at about 22 percent, that is short of the 32 percent average of carbonate reservoirs in the Permian Basin (Tyler and Banta, 1989; Holtz and Garrett, 1990). An efficient recovery of hydrocarbons in the Clear Fork reservoirs is made difficult due to the reservoirs' wide-range geologic and petrophysical properties (Ruppel and Harrington, 2012). Upper Clear Fork strata comprise of shoaling-upward carbonate sequences deposited on a broad shallow marine shelf behind shelf margin bank complexes. Further landward, evaporite deposition occurred in supratidal brine pans within extensive tidal flat and sabkha environments (Silver and Todd, 1969). An understanding of the Clear Forks facies variability from these depositional environments and their petrophyscial properties are thus critical to hydrocarbon recovery. For this study, 7 core samples from 2 wells were collected from the upper Clear Fork and tested with a range of experiments to gain a better understanding of the facies and mineralogy effect (anhydrite in particular) on pore structure of, and fluid flow through the formation.

Chapter 2: Geological Background

2.1 Geological Setting

The Permian Basin is located primarily in west Texas and stretches westward into southeast New Mexico. As shown in Figure 1, the Permian Basin is commonly divided up by the Central Basin Platform into the Midland Basin to the east, the Delaware Basin to the west and the Val Verde Basin to the South. The study area is the Palm Sunday field in the Permian Basin, along the border of the Midland Basin in the Northern Shelf (Figure 2).

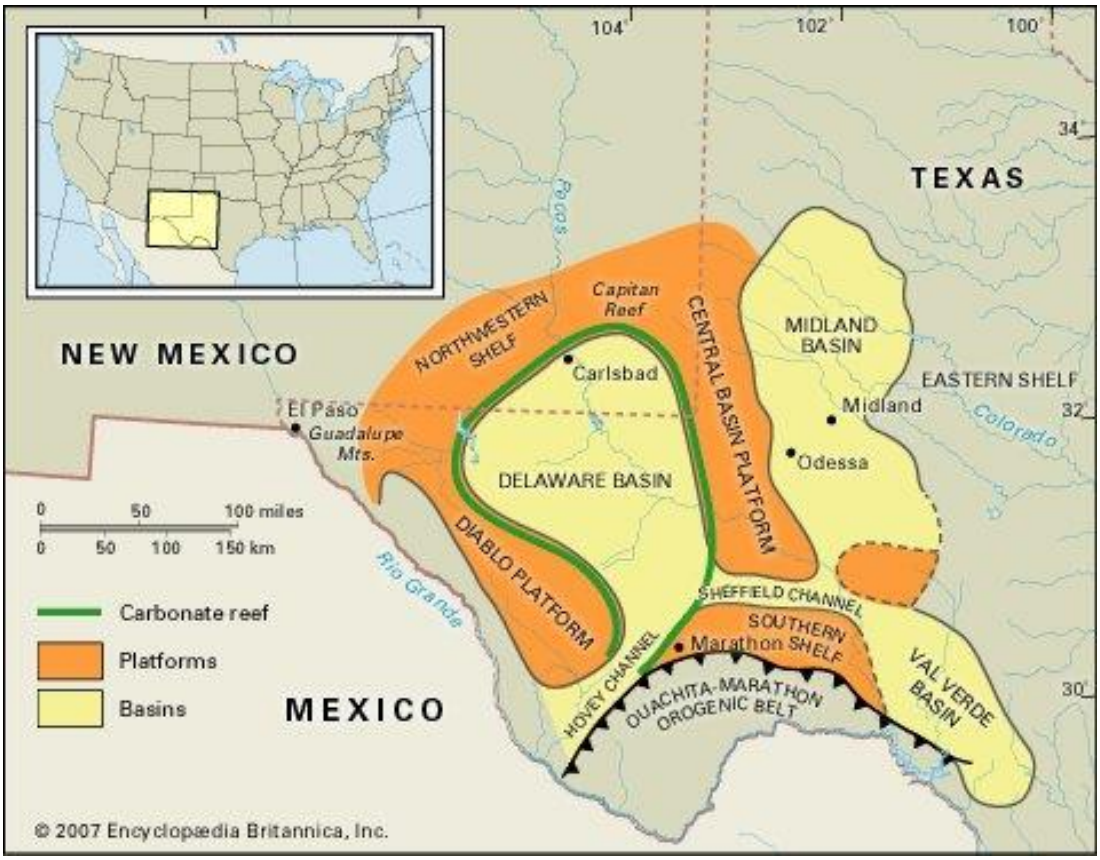

Figure 1: Map of the separate basins within the Permian Basin of west Texas and southeast New Mexico (https://www.britannica.com/place/Permian-Basin).

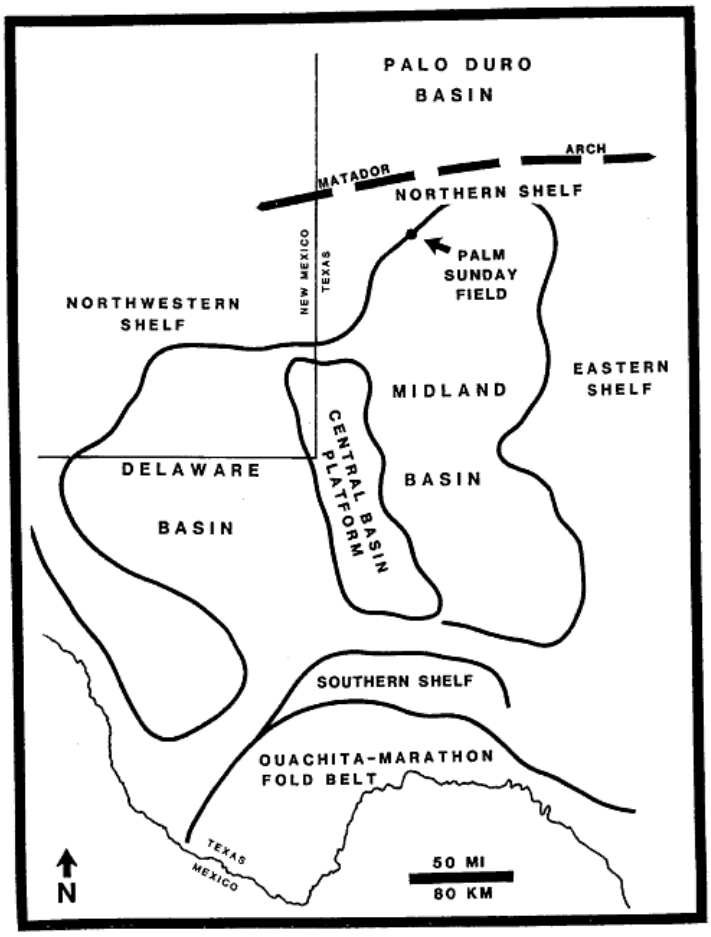

Figure 2: Map of Permian Basin showing the northern shelf north of the Midland basin just south of the Matador Arch (modified after Silver and Todd, 1969).

During the late Paleozoic, the Permian Basin formed from the collision of Gondwana and Laurentia, known as the Marathon-Ouachita orogeny (Dorobek, 1995). Prior to the collision, sediments were accumulating in the Tobosa Basin, an ancestral province of the Permian Basin. From the Cambrian into the Pennsylvanian, primarily carbonates were deposited into the basin where a periodic deposition of clastic sediments from eroded surrounding structural highs deposited into the basin (Yang and Dorobek, 1995). The Permian Basin experienced a rapid subsidence from the Pennsylvanian into the Wolfcampian where the subsidence slowed

throughout the rest of the Permian (Oriel et al., 1967; Robinson, 1988; Yang and Dorobek, 1995).

2.2 Stratigraphy

Initially the Clear Fork group was described for the exposures of limestone, sandstone, and calcareous clay near the Clear Fork of the Brazos River in Jones and Shakelford counties, Texas. Usage of the term "Clear Fork" for upper Leonardian shelf deposits from the northern Midland Basin has grown as well as the informal subdivision of Clear Fork strata into the upper, middle and lower units (Fig. 3; Silver and Todd, 1969; Jeary, 1978; Mazzullo, 1982). Thicknesses of these units range from approximately 400 ft for the lower Clear Fork in Hockley County to more than 2000 ft for the middle Clear Fork in Lubbock County (Jeary, 1978). Middle and lower Clear Fork carbonate strata are characterized as shallow shelf/lagoonal deposits of bedded micritic-skeletal dolomite with nodular anhydrite. Shelf facies grade basinward into shelf-margin beds composed of oolite bars and localized skeletal buildups (Russell, 1990). The shelf margin grades basinward into fore-slope deposits containing debris flow and turbidity transported shelf lithoclasts. These fore-slope deposits appear darker in color and contain silicified fossils (Silver and Todd, 1969). The Glorieta Formation conformably overlies the Clear Fork with carbonate and siliciclastic deposits, as shown in Figure 3 (Jeary 1978).

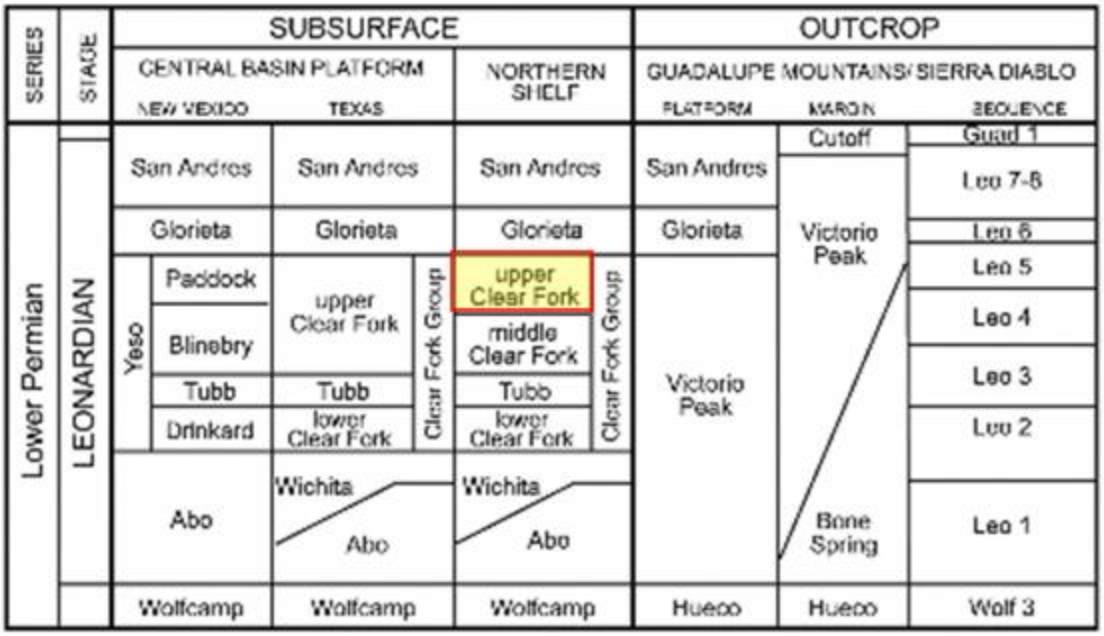

Figure 3: Stratigraphic Columns of the Central Basin Platform, Northern Shelf and Guadalupe Mountains (Ruppel and Harrington, 2012).

The upper Clear Fork Formation of the Midland Basin was deposited during the Leonardian Epoch of the Permian. Previous work by Mann (2017) was performed on the Paddock Formation of the Northwest Shelf deposited simultaneously as the upper Clear Fork of the Northern Shelf. Upper Clear Fork shelf deposits are characterized as bedded micritic-skeletal dolomites which grade laterally into marginal bank deposits. The lower sections of the upper Clear Fork shelf are silty and shaly and become exclusively carbonate upwards (Jeary, 1978). The upper Clear Fork inner shelf consists of burrowed and churned dolomitic wackestones and packstones deposited in subtidal-intertidal environments while algal-laminated dolomitic mudstones contain desiccation features and nodular anhydrite (Lucia, 1969). Brine pan and salt flat systems deposited landward of the inner shelf consist of laminated dolomite, nodular mosaic anhydrite, laminated anhydrite with halite-filled molds of vertically oriented gypsum crystals, massive halite deposits, and halite and red-brown mudstone (Presley and McGillis, 1981).

Chapter 3: Methods

3.1 Sample acquisition & preparation

After deciding to focus my research on the upper Clear Fork of the Permian Basin, I searched through a catalog of whole core samples available from Texland Petroleum and decided on the Palm Sunday field in Hockley County, Texas. Two wells of the Palm Sunday field have log and core data (Table 1). In addition, Mosley (1990) previously determined seven facies types within the cored intervals of these two wells, C. M. Anderson 1 (API: 42-219-34718) and C. M. Anderson 2 (API: 42-219-34775). As shown in Table 2, samples were selected in order to cover all facies types described by Mosley (1990). Core Laboratories performed the core analyses for both wells (Table 3). I then drove out to Texland Petroleum's offsite storage where the core was stored to secure a total of seven whole core samples from these two wells. One sample was taken from C. M. Anderson 1 and six samples from C. M. Anderson 2 (Table 2).

Table 1: Logs and core data available on Texland Petroleum wells of the Palm Sunday field.

Well Name	**County**	**Available logging and samples type**	**Cored Interval (ft)**	**Samples**
C.M. Anderson 1	Hockley	Gamma ray, resistivity, neutron porosity, density porosity, whole core	6383-6414	1
C.M. Anderson 2			6328-6417	6

Table 2: Depths and facies of each sample.

Well Name	**Sample ID**	**Sample Depth (ft.)**	**Mass (g)**	**Facies designation by Mosley (1990)**
C.M. Anderson 1	Anderson 1-6403	6403	1106.6	Massive Mudstone
C.M. Anderson 2	Anderson 2-6335	6335	1385.91	Bryozoan-Crinoid-Tubiphytes Wackestone/Packstone
C.M. Anderson 2	Anderson 2-6355	6355	1307.1	Parachaetetes Tubiphytes Boundstone/Grainstone
C.M. Anderson 2	Anderson 2-6367	6367	1189.5	Bryozoan-Sponge-Tubiphytes Boundstone
C.M. Anderson 2	Anderson 2-6376	6376	1488.9	Crinoid-Bryozoan Packestone/Grainstone

C.M. Anderson 2	Anderson 2-6385	6385	976.2	Bryozoan-Sponge-Tubiphytes Boundstone
C.M. Anderson 2	Anderson 2-6402	6402	1309	Bioclastic Wackestone/Packstone

Table 3: Core Analysis results performed by Core Laboratories.

Sample ID	**Particle Density (g/cm3)**	**Porosity (%)**	**Permeability (mD)**	**Water Saturation (%)**	**Oil Saturation (%)**
Anderson 1-6403	2.86	5.60	0.4	40.7	25.9
Anderson 2-6335	2.85	1.60	1.4	80.6	6.5
Anderson 2-6355	2.83	3.10	0.76	81.5	3.7
Anderson 2-6367	2.84	0.80	1.5	89.7	6.9
Anderson 2-6376	2.83	1.40	0.41	89.4	4.3
Anderson 2-6385	2.83	1.40	2.5	92.3	0
Anderson 2-6402	2.83	6.30	1.5	39.7	23.1

Once the samples were collected, the first test for the whole core (Figure 4) was conducted for vacuum saturation. Then the samples were cored for plugs of 2.54 cm in diameter, cut into 1cm-sized cubes, and grinded down for different tests. Core plugs were taken at both horizontal and transverse directions with respect to core length, for vacuum saturation experiments as well. A total of 15 1-cm sided cubes were prepared using a Hi-Tech Diamond Rock Saw (Figure 5) for vacuum saturation, imbibition, and vapor absorption, involving two fluids of DI (deionized water) and DT2 (n-decane : toluene = 2:1 in volume). After plugs and cubes were cut, the remainder of the core fragments were broken down with a hammer and the small pieces were placed into an electric grinder (Figure 6). The samples were then placed into a stacked sieve system to separate sample into six different granular sizes (Figure 7). The sample sizes collected were #8/#12 (locally called as GRI+), #12/#20 (Size A), #20/#35 (GRI), #35/#80 (Size B), #80/#200 (Size C), and <#200 (Powder) as shown in Figure 8. These various sample

sizes were used to analyze for TOC, pyrolysis, particle-bulk density, and liquid pycnometry through different experiments.

A)

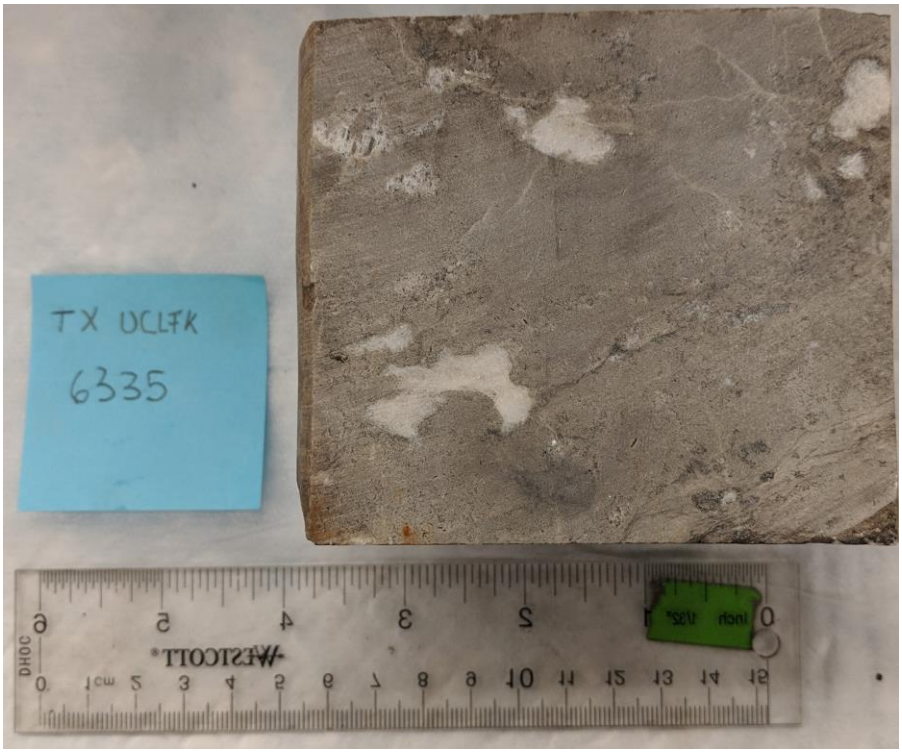

B)

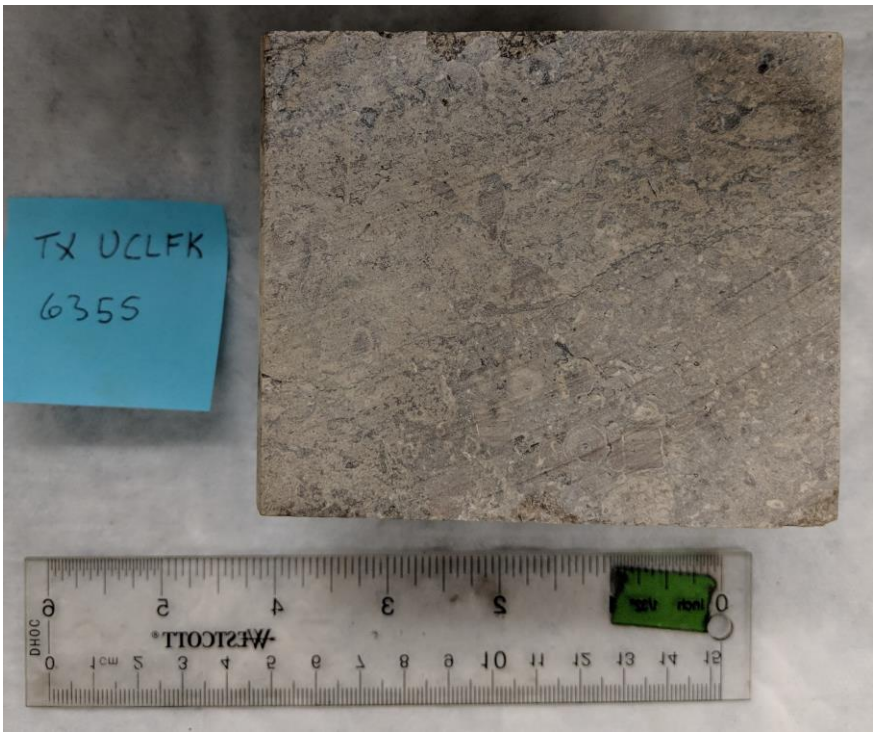

C)

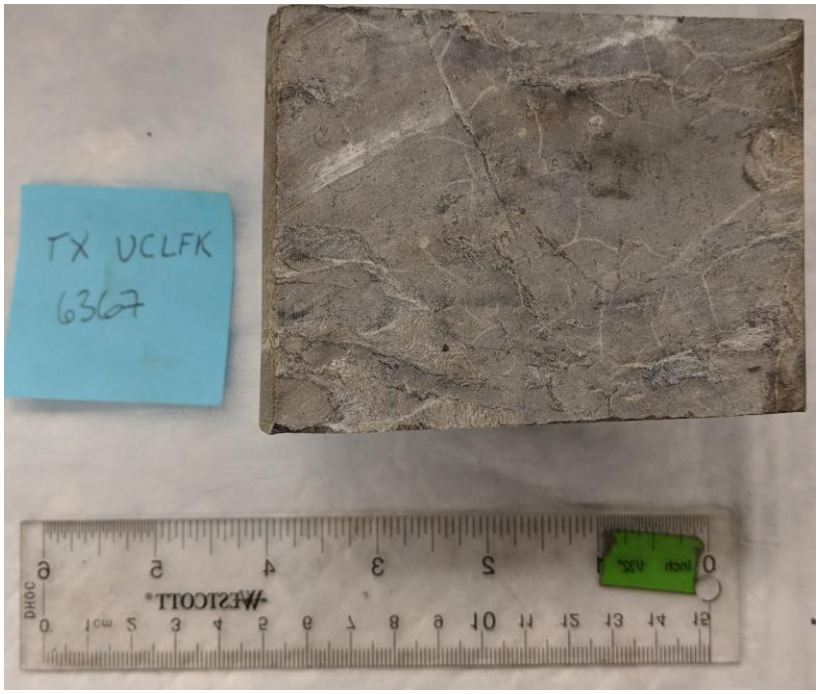

D)

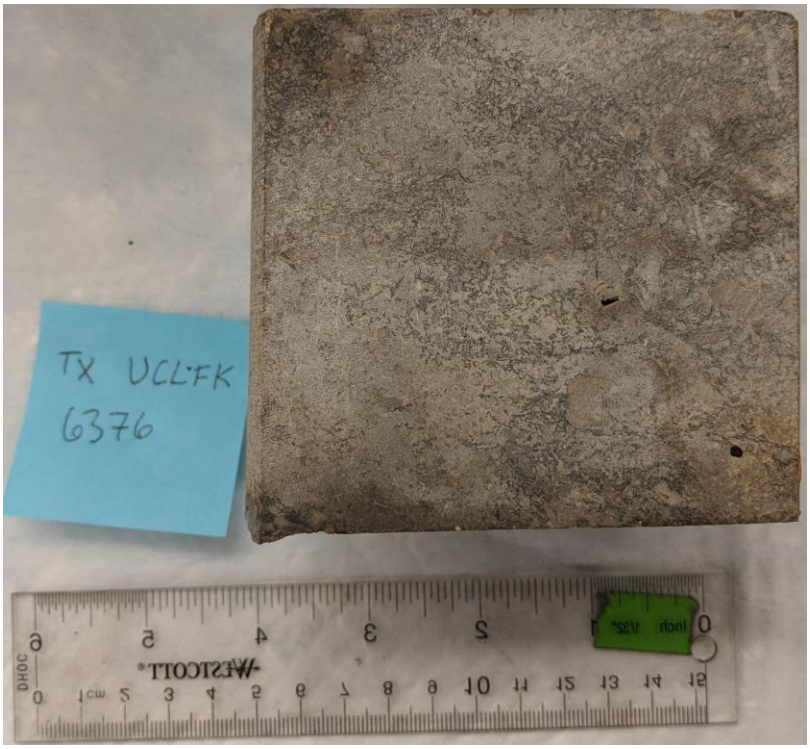

E)

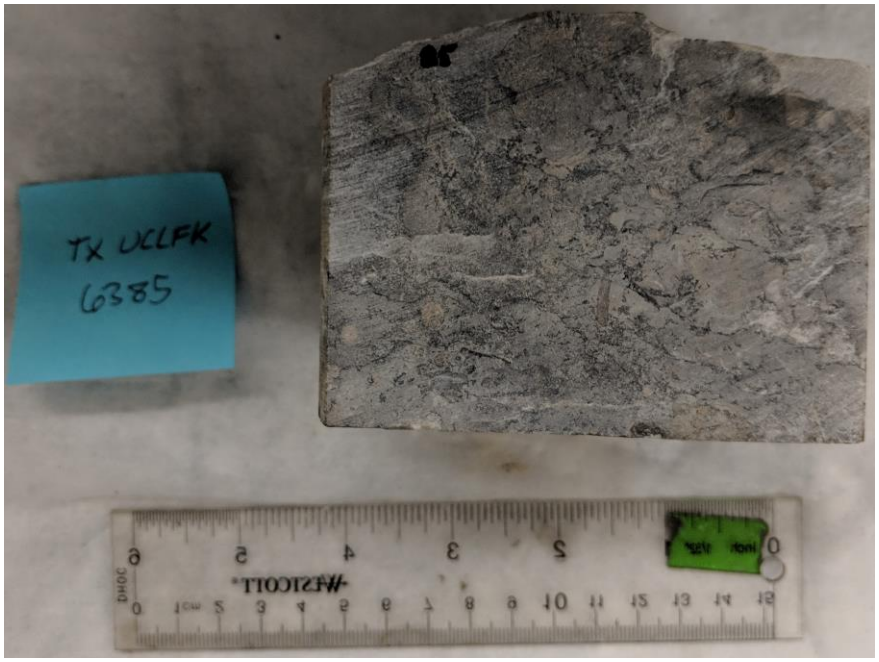

F)

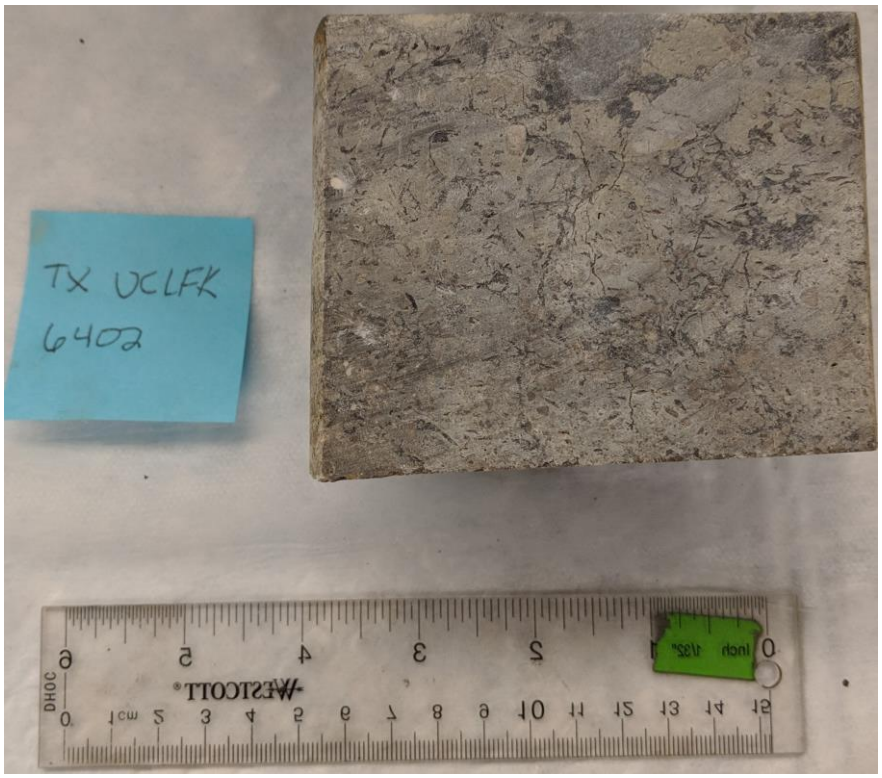

G)

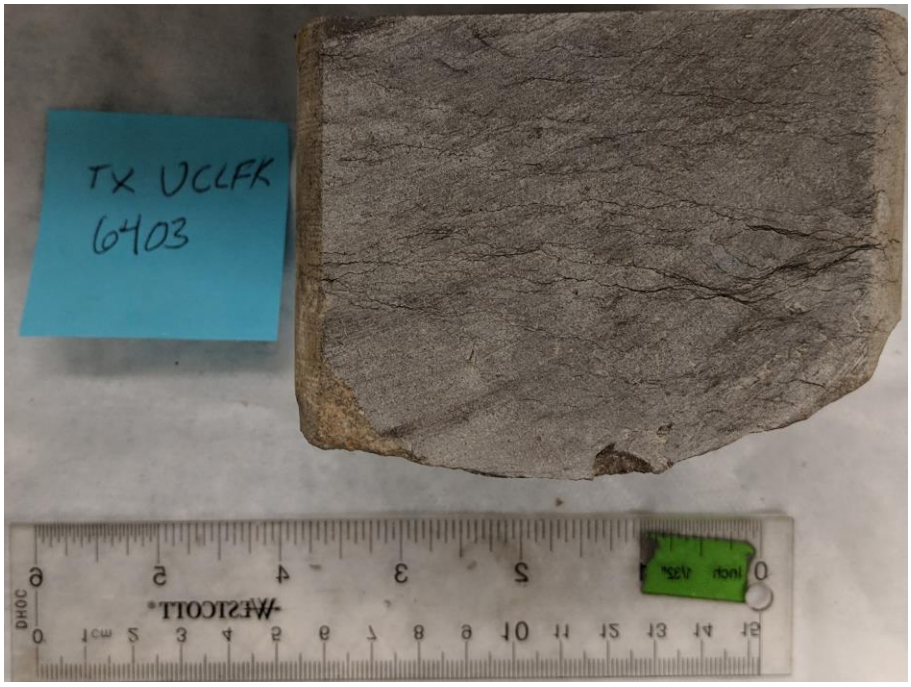

Figure 4: (A-G) Side views of whole core samples used in this work; TX: Texas; UCLFK: upper Clear Fork.

Figure 5: Hi-Tech diamond saw.

Figure 6: Electric grinder.

Figure 7: Stacked sieve system.

Figure 8: Different sample sizes for sample Anderson 2-6376.

3.2 X-ray Diffraction, TOC, and pyrolysis

Using powder-sized fractions, X-ray diffraction (XRD) tests were conducted on all samples to determine the mineral composition and assess its control on pore structure. The XRD test was conducted using the Shimadzu MAXimaX XRD-7000 machine, with the methods and procedures shown in Appendix A.

Total organic carbon (TOC) and pyrolysis analyses were performed on all seven samples by GeoMark Research. Methods and procedures for TOC and pyrolysis are shown in Appendix B. TOC is the measurement of the amount of organic carbon present in the sample. Pyrolysis analysis determines values for S1, S2, S3, and T_{max}. S1 values indicate the residual hydrocarbons contained within the rock. S2 values display the remaining hydrocarbon generation potential. S3 values show the remaining carbon dioxide within the rock. The maximum temperature of hydrocarbon generation from S2 analysis is termed as $T_{max.}$

3.3 Vacuum Saturation

Edge-accessible porosity, bulk density and particle density were first to be obtained through vacuum saturation tests. Vacuum-pulling assisted saturation tests were conducted first on whole core, and then plug and cubic samples. Samples were placed in a 60-degrees Celsius oven for at least two days to remove the water in the connected pore space. Samples were then cooled down in the desiccator for 30 min and weighed. Samples were then placed into a closed chamber connected to a vacuum that is custom designed (Figure 9). Initial evacuation of the chamber reduced the pressure to <0.2 Torr at about 30 min and remain at this level for at least 8 hrs. For the DIW run, then CO_2 at 30 psi was injected into the chamber for 30 minutes to replace any air in the pore space of the samples then evacuated using the vacuum for at least another 8

hrs. A fluid (DIW or DT2) was then filled into the chamber until the sample was completely submerged. Another pulse of CO_2 was then injected into the chamber again for 30 minutes to help force the fluid into the pore space of the sample. The sample was left in chamber for another 3-4 hrs before being removed from the chamber and weighed both in air & under the fluid for bulk density calculations through Archimedes' principle. The sample was then placed inside the 60°C oven for at least 2 days and weighed again to account for any sample loss from the whole testing process.

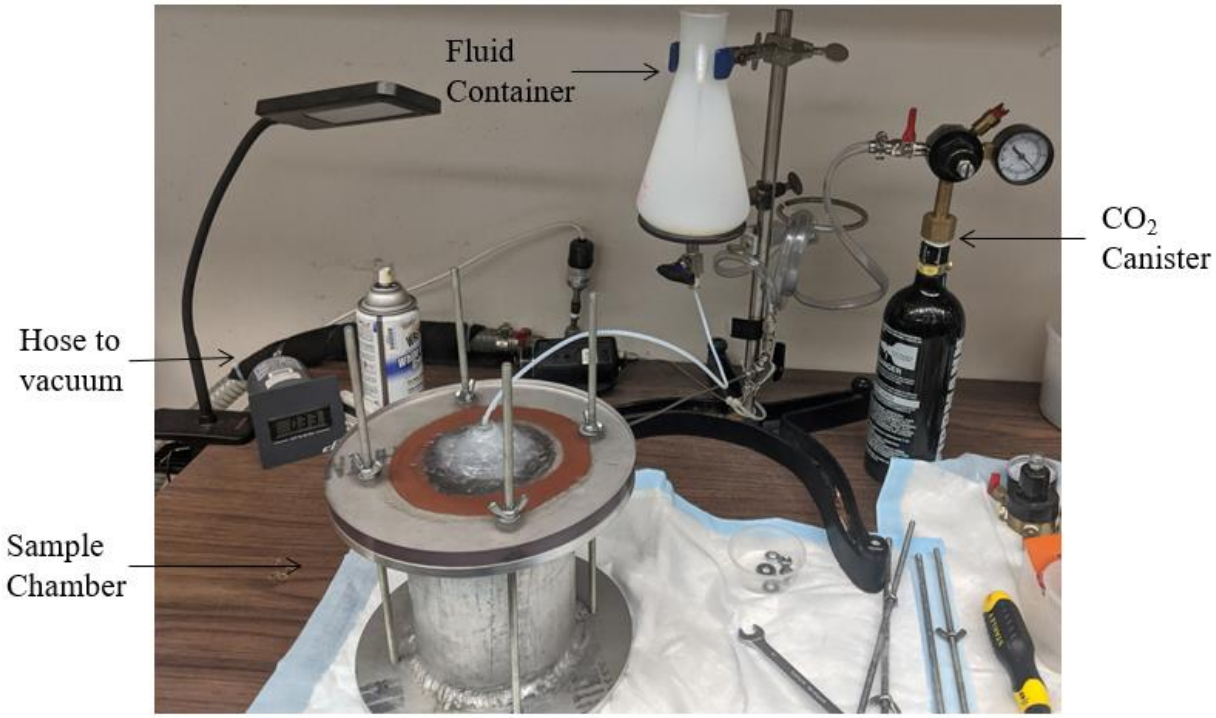

Figure 9: Custom-designed vacuum saturation apparatus.

3.4 Mercury Intrusion Capillary Pressure (MICP)

MICP analysis was performed on a piece of 1 cm cube for all seven samples to determine pore structure characteristics using the Micromeritics Autopore IV 9520 machine. Measurements

determined through MICP include bulk density, particle density, porosity, pore throat size distribution, permeability, and tortuosity. Mercury is a non-wetting fluid for most rocks and requires an elevated pressure to be forced into the pore space of the rock (Hu et al, 2015). As pressure is increased incrementally up to 60,000 psi, the mercury can invade pore space controlled by increasingly smaller pore throats. The pore throat radius invaded by mercury is inversely proportional to the applied pressure (Gao and Hu, 2013). Pore throat diameters can be measured from 45 μm to 3 nm using the Washburn equation (Equation 1; Washburn, 1921). From the MICP results, permeability and tortuosity is calculated using Equation 2 (Katz and Thompson, 1987) and Equation 3 (Hager, 1998; Webb, 2001; Hu et al., 2015), respectively.

$$\Delta P = -\frac{2\gamma \cos\,\theta}{r} \quad \text{Eq. 1}$$

where

ΔP = External pressure (psi);

γ = Surface tension of mercury (dynes/cm);

θ = Contact angle between porous media and mercury (degrees);

r = Pore throat radius (μm).

$$k = \left(\frac{1}{89}\right)\left(\frac{(L_{max})^3}{L_c}\right)\varphi S(L_{max}) \quad \text{Eq. 2}$$

where

k = permeability (μm^2);

L_{max} = Pore throat diameter at maximum hydraulic conductance (μm);

L_c = Pore throat diameter at the threshold pressure (μm);

φ = Porosity (fractional);

$S(L_{max})$ = Mercury saturation at L_{max} (fractional).

$$\tau = \sqrt{\frac{p}{24k(1+pV_{tot})}\int_{n=r_c,max}^{n=r_c,min} n^2 f_y(r_c)dr_c} \quad \text{Eq. 3}$$

where

τ = Tortuosity;

ρ = Density of mercury(g/cm^3);

$\int_{n=r_c,min}^{n=r_c,max} n^2 f_y(r_c)dr_c$ = Pore throat volume distribution by pore throat size.

A modified version of the Washburn equation developed by Wang et al. (2016), shown in Equation 4, was used to account for an increase of contact angle and surface tension with a decreasing pore throat radius.

$$\Delta P = -\frac{2\gamma\mathrm{Hg(r)}\cos\ \theta Hg(r)}{r} \quad \text{Eq. 4}$$

where

γHg and θHg are functions of R.

With respect to the MICP analyses, samples were first placed in a 60°C oven for at least 48 hrs and then moved into a desiccator to cool down to room temperature. Then the sample was placed inside a penetrometer that was evacuated before the mercury was released to surround the sample to calculate the bulk density. Pressure was then increased incrementally from 5 psi until a pressure of 60,000 psi was reached to measure the mercury intrusion at each pressure increment. Then mercury extrusion was measured as the pressure was dropped incrementally.

3.5 Fluid Imbibition and Vapor Absorption

The measurement of pore connectivity in a sample is achieved from imbibition and vapor absorption tests. Only the bottom face of oven-dried samples was submerged into a fluid (DIW or DT2) and weights were recorded over time. Capillary pressure drives imbibition by displacing the nonwetting air with the wetting fluid (Gao and Hu, 2011). Slopes from the cumulative imbibition vs. time in log-log scales are used to assess the pore connectivity of each sample tested towards the fluid. For a wetting fluid into well-connected pore network, the cumulative imbibition can be expressed by Equation 5.

$$I(t) = St^{0.5} \qquad \text{Eq. 5}$$

where

I(t) = Cumulative imbibition (mm);

S = Sorptivity ($m/sec^{0.5}$);

t = Time (min).

About the experimental procedure of imbibition tests, the cubic sample was placed into a 60-degrees Celsius oven in order to remove any fluids that may be present. Then the sample was placed inside a desiccator for at least 30 min while the sample returned to room temperature. Weights were recorded using the Radwag AS 60/220.R2. balance (with a readability of 0.01 mg) for the sample, the sample holder, the petri dish, and the fluid contained depending on the test (DIW or DT2) before the test started. The sample was placed in the sample holder and hung from the balance until the bottom exposed surface of the cube sample contacted the liquid solution being used inside the petri dish (Figure 10). Weights were recorded by a computer for various time intervals and durations depending on the test. For DIW tests lasted for 6 hrs and 24 hrs, and DT2 tests would last for 4 hrs for its better wettability than DIW. Afterwards, the sample, sample holder, petri dish and its liquid solution were weighed to determine how much fluid imbibed or flowed into the sample.

Vapor absorption was conducted similarly to imbibition however the same cubic sample was hung over the fluid in the petri dish without making a direct contact with the fluid. Fluid from the petri dish was transported by vapor absorption and capillary condensation into the hanging sample (Hu et al., 2001). Tests for vapor absorption were run for 48 hrs using both DIW and DT2.

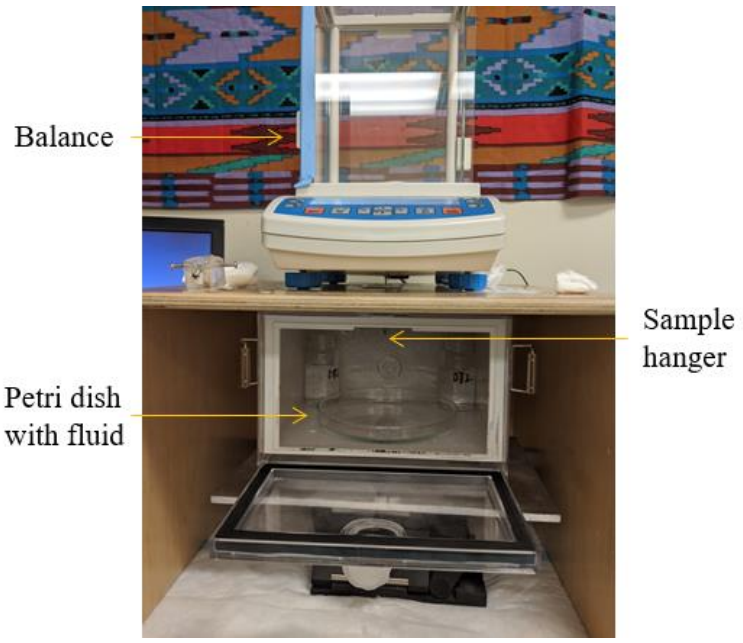

Figure 10: Fluid imbibition and vapor absorption apparatus.

3.6 Liquid Pycnometry

As the vacuum saturation approach will not work with small samples less than 5 mm, "apparent" bulk density was calculated through the liquid pycnometry experiments using two different fluids (DIW and DT2). Sample sizes GRI+, A, GRI, B, and C for each sample were placed into the 60 degrees oven for up to two days, then 2 g of sample was weighed out and placed into a 10-mL pycnometer. The pycnometer and sample were weighed and then fluid (DIW or DT2) was filled to the top pycnometer and weighed. The pycnometer was then emptied and filled with just the fluid to the top and weighed again. Using the weight of the pycnometer with sample, pycnometer with sample and fluid, and pycnometer and fluid only, the apparent bulk density can be calculated using Equation 6.

$$\rho_b = m_1/(m_2 - m_3 + m_1)/\rho_f \qquad \text{Eq. 6}$$

where

ρ_b = Apparent bulk density (g/cm^3);

m_1 = Weight of sample (g);

m_2 = Weight of pycnometer and fluid (g);

m_3 = Weight of pycnometer, fluid, and sample (g);

ρ_f = Fluid density (g/cm^3).

3.7 Particle Density

Particle density was measured using the AccyPyc II 1340 of Micromeritics Instruments on sample sizes of GRI+ and A. About 10 g of sample was weighed out and placed inside the sample chamber located on the top of the AccuPyc II 1340 (Figure 11). Sample weight was entered using the keypad of the instrument. The sample chamber was then filled with helium at a pressure of 200 psi to determine the sample volume. The particle density was then calculated by the AccuPyc II 1340 (Micromeritics Instrument Corporation, 2020).

Figure 11: AccuPyc II 1340 control module with keypad on the left and analysis module on the right.

3.8 Well Log Analysis

Rock properties can be measured from well logs to provide insight to reservoir characteristics in the surrounding area and can be correlated to nearby wells. Raster and digital logs were provided by Texland Petroleum for our two wells being studied. The IHS software Petra was used for calculations and analyses of digital logs. Calculations made from digital logs can provide additional data for the pertrophysical properties such as porosity, water saturation, and permeability at a formation scale that is much larger than the laboratory scale.

The average of the neutron and density porosity logs were used to determine the true porosity (Equation 7).

$$\phi_t = \frac{NPHI+DPHI}{2} \qquad \text{Eq. 7}$$

where

Φ_t = Average porosity (%);

NPHI = Neutron porosity (%);

DPHI = Density porosity (%).

The water saturation at a particular depth can be calculated using the Archie equation (Equation 9; Archie, 1942). The water saturation is important to understand the fluid contained within the pore space. The higher the water saturation, the lower the amount of hydrocarbon that can be contained within the pore space of the rock.

$$S_w = \left(\frac{R_w}{R_t * \varphi^m}\right)^{1/n} \quad \text{Eq. 8}$$

where

S_w = Water saturation (%);

R_W = Water resistivity (ohm-m);

R_t = True resistivity (ohm-m);

Φ = Porosity (%);

m = cementation factor;

n = saturation exponent.

The deep resistivity curve was used for true resistivity and the previously calculated average porosity was used for porosity determination. Constant values of 2 were used for both the cementation factor and the saturation exponent. The water resistivity at a formation depth

was calculated using Arp's equation and determined to be 0.03 ohm-m for both wells (Equation 9; Doveton, 1999). In order to calculate water resistivity at formation depth, temperature at formation depth from raster logs is needed as well as laboratory tested water resistivity at room temperature (Core Laboratories, 1972).

$$Rw_2 = Rw_1 \frac{T_1+6.77}{T_2+6.77} \quad \text{Eq. 9}$$

where

Rw_2 = Water resistivity at formation depth (ohm-m);

Rw_1 = Measured water resistivity (ohm-m);

T_1 = Temperature at measured water resistivity Rw_1 (Fahrenheit);

T_2 = Temperature at formation depth (Fahrenheit).

Permeability can be determined from log data using Equation 10 (Timur, 1968). This equation determines permeability through porosity and water saturation by requiring that the formation be in an irreducible water saturation.

$$k = \left(\frac{93*{\varphi_t}^{2.2}}{Sw}\right)^2 \quad \text{Eq, 10}$$

where

k = Permeability (mD).

Chapter 4: Results

4.1 X-ray Diffraction (mineralogy)

The mineralogy from XRD analyses of each sample is shown in Table 4. All seven samples are carbonate rocks composing of quartz, dolomite, and anhydrite. Quartz percentages for all samples only range from 0.4 to 4.3%. Dolomite percentages for samples Anderson 2 6355 and Anderson 1 6403 range from 90 to 92.4%, and anhydrite percentages ranging from 3.3 to 9.6%. Dolomite percentages for samples Anderson 2 6335 and Anderson 2 6367-6402 vary from 46.1 to 69.0% and anhydrite percentages differ from 30.1 to 53.0%. Mineral content for each sample is displayed in Figure 12. In addition, carbonate percentages from pyrolysis analyses closely matched dolomite percentages from XRD analysis.

Table 4: Mineralogy results of each sample from XRD analyses.

Sample ID	Quartz (wt%)	Dolomite (wt%)	Anhydrite (wt%)
Anderson 1-6403	4.3±0.3	92.4±6.4	3.3±0.3
Anderson 2-6335	0.9±0.1	61.6±3.9	37.5±2.4
Anderson 2-6355	0.4±0.1	90.0±6.1	9.6±0.7
Anderson 2-6367	1.0±0.1	69.0±4.5	30.1±2.0
Anderson 2-6376	0.7±0.2	61.2±4.0	38.1±2.5
Anderson 2-6385	0.9±0.2	46.1±3.2	53.0±3.6
Anderson 2-6402	0.7±0.2	51.9±3.7	47.4±3.4

Figure 12: Stacked bar chart with each sample's mineral content.

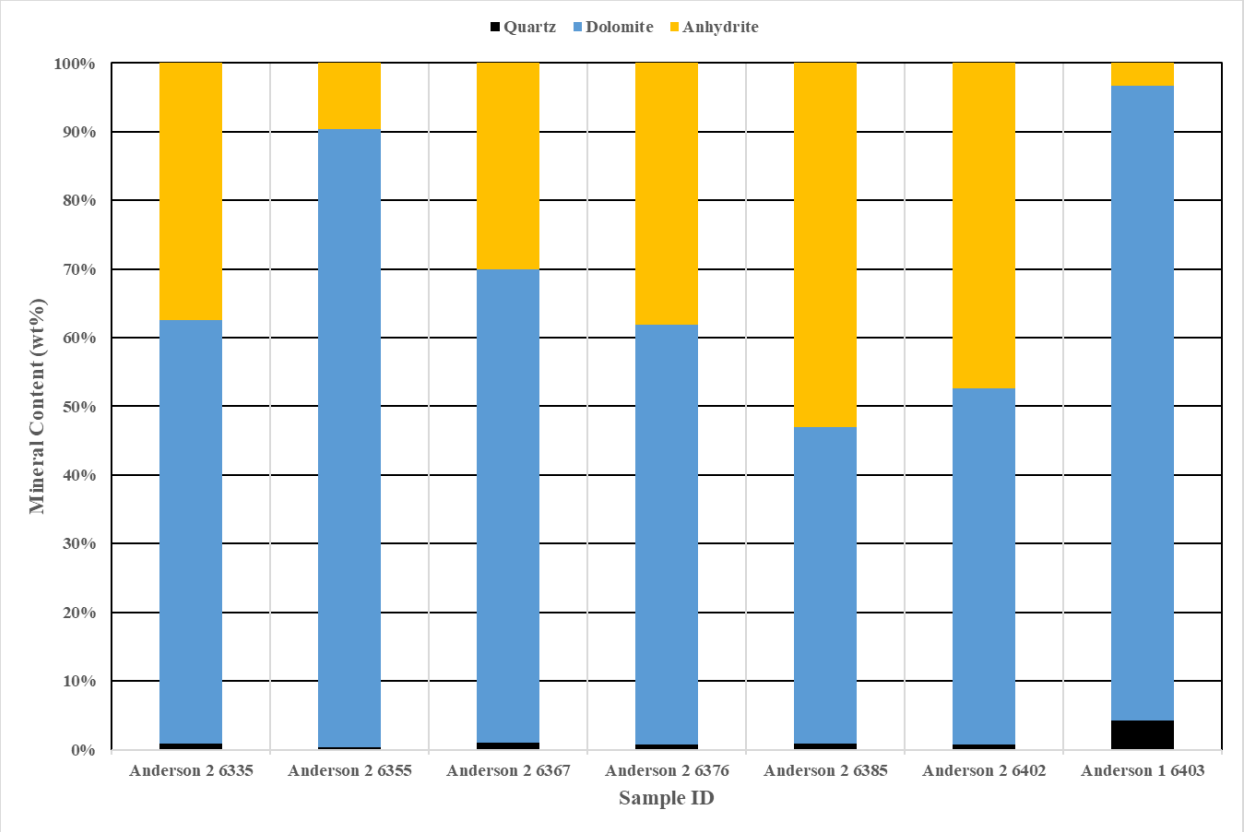

4.2 TOC and Pyrolysis

Geochemistry data from LECO TOC and HAWK pyrolysis analyses for all 7 samples are shown in Table 5. TOC weight percentages range from 0.06% for sample Anderson 2-6385 to 0.51% for sample Anderson 1-6403. S1 values from pyrolysis analysis range from 0.03 mg HC/g for sample Anderson 2-6385 to 0.16 mg HC/g for Anderson 1 6403. S2 values vary from 0.04 mg HC/g for sample Anderson 2-6402 to 0.77 mg HC/g for sample Anderson 1-6403. S3 values differ from 0.34 mg CO_2/g in samples Anderson 2-6335 and 2-6402 to 0.51 mg CO_2/g in Anderson 1-6402. Kerogen types are determined from the Pseudo Van Krevelen plot of oxygen index vs. hydrogen index (Figure 13) and kerogen quality plot of TOC vs. S2 (Figure 14). Both plots show all samples to be gas prone Type III kerogen. With their oxygen indices larger than

200, Anderson 2 samples plotted too far to the right to be shown in Figure 13 and adjustments made to include the samples jeopardized the quality of the graph. Normalized oil content and vitrinite reflectance was plotted against depth to determine hydrocarbon maturity (Figure 15). All samples were shown to be immature or early oil generation except for sample Anderson 2-6402 shown in the oil/gas production window in the normalized oil content plot possibly due to contamination.

Table 5: TOC and pyrolysis data of Anderson #1 and #2 samples.

Sample ID	Carbonate (wt%)	TOC (wt%)	S1 (mg HC/g)	S2 (mg HC/g)	S3 (mg CO_2/g)	Tmax (°C)	Vitrinite Reflectance (%Ro)	Hydrogen Index (S2x100/TOC)	Oxygen Index (S3x100/TOC)	Production Index (S1/S1+S2)	Normalized Oil Content S1/TOC
Anderson 1-6403	**83.6**	**0.51**	**0.16**	**0.77**	**0.51**	**429**	**0.56**	**152**	**101**	**0.17**	**32**
Anderson 2-6335	**73.1**	**0.14**	**0.05**	**0.10**	**0.34**	**435**	**0.67**	**70**	**239**	**0.33**	**35**
Anderson 2-6355	**93.2**	**0.14**	**0.05**	**0.10**	**0.42**	**425**	**0.49**	**69**	**292**	**0.33**	**35**
Anderson 2-6367	**73.9**	**0.09**	**0.04**	**0.06**	**0.41**	**430**	**0.58**	**69**	**475**	**0.40**	**46**
Anderson 2-6376	**68.7**	**0.08**	**0.03**	**0.09**	**0.37**	**434**	**0.65**	**110**	**452**	**0.25**	**37**
Anderson 2-6385	**52.8**	**0.06**	**0.05**	**0.05**	**0.38**	**423**	**0.45**	**75**	**596**	**0.50**	**78**
Anderson 2-6402	**55.6**	**0.40**	**0.07**	**0.04**	**0.34**	**430**	**0.58**	**103**	**876**	**0.64**	**180**

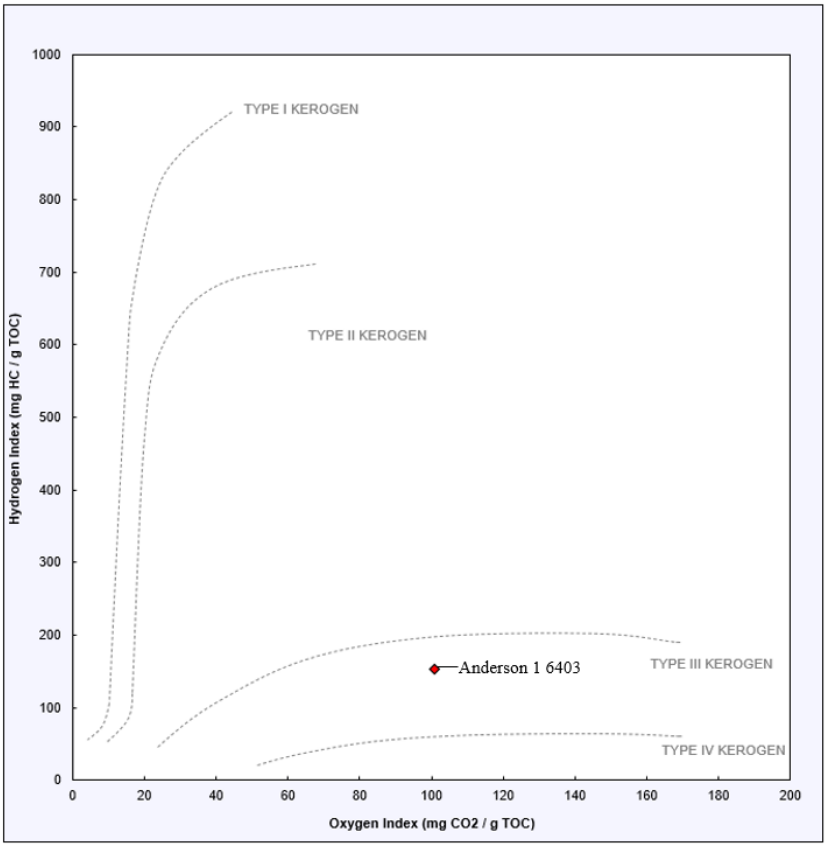

Figure 13: Pseudo Van Krevelen plot for kerogen types.

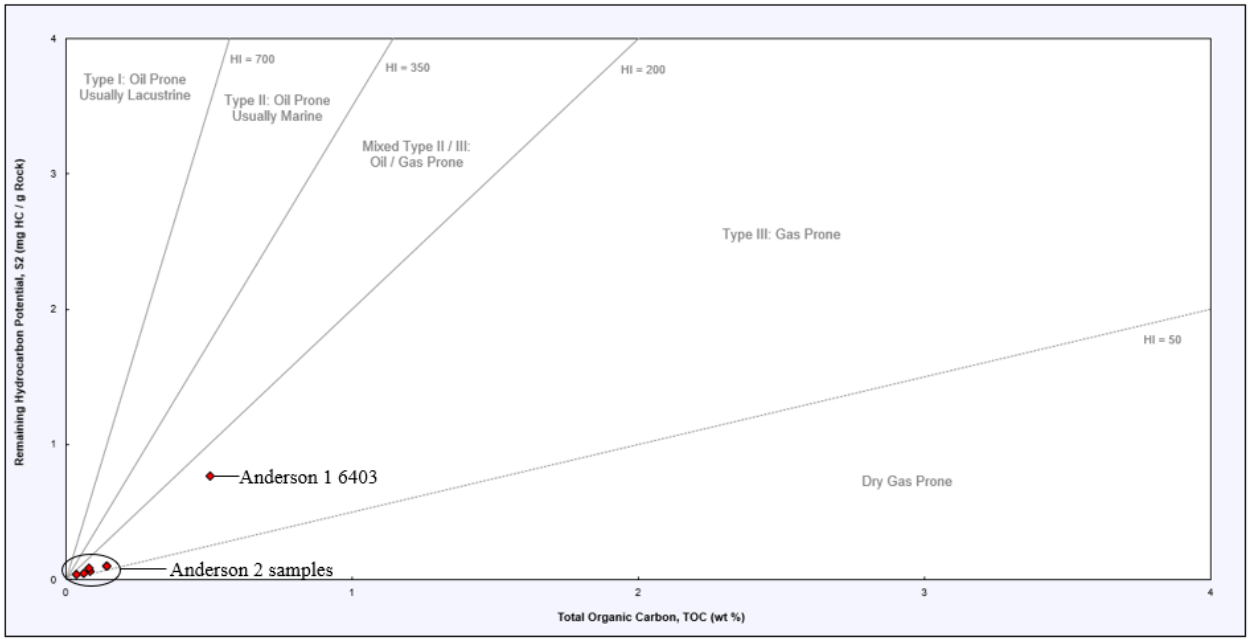

Figure 14: TOC (wt%) vs. S2 (mg HC/g rock) plot for kerogen types.

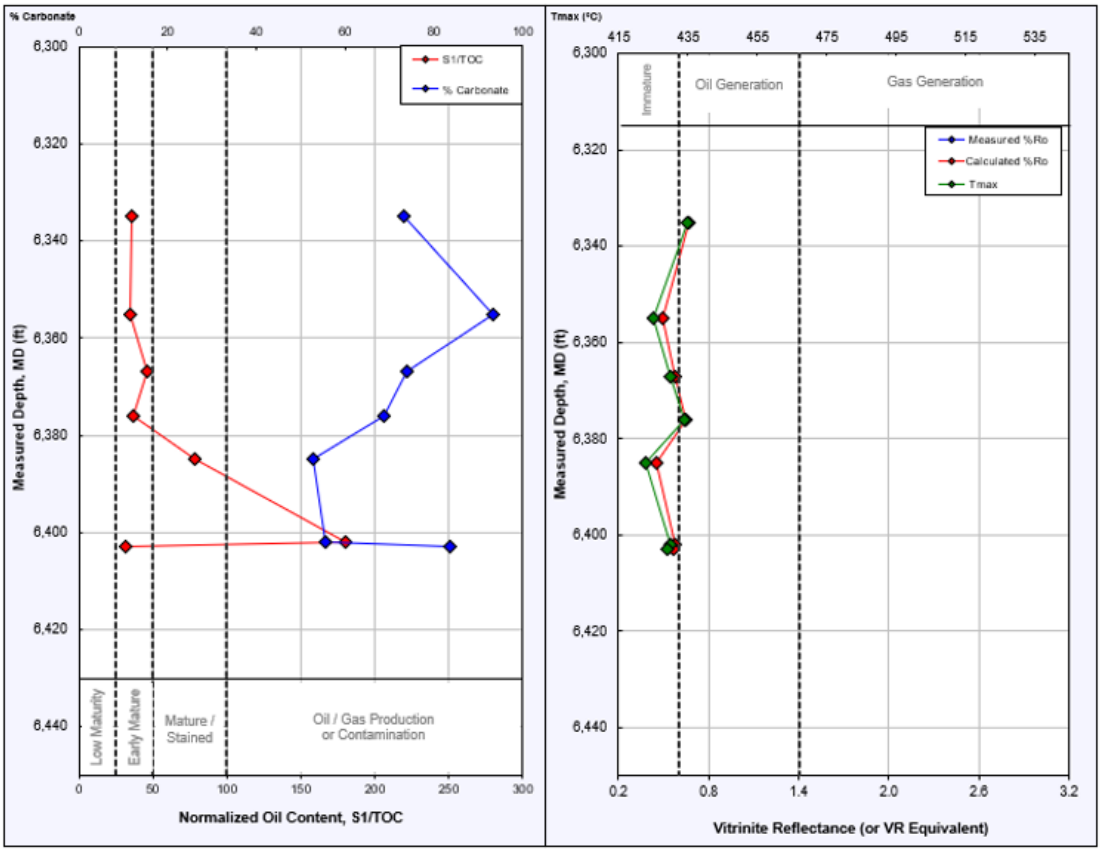

Figure 15: Anderson 1 and 2 well samples normalized oil content (left) and vitrinite reflectance (right) by depth.

4.3 Vacuum Saturation

Bulk density, particle density, and edge-accessible porosity calculated from vacuum saturation for all 7 samples are shown in Table 6. Whole core, plugs, and cubes for all samples were tested using DIW. Edge-accessible porosity values range from 0.228 to 1.53% for whole cores, 0.371 to 3.32% for plugs, and 0.551 to 4.45% for cubes with sample Anderson 1 6403 (the only carbonaceous mudstone in 7 facies) showing the highest, but only slightly larger, porosity. Porosity values tend to increase as the sample sizes are decreased.

Table 6: Porosity, particle density and bulk density results from vacuum saturation.

Sample ID	Sample type	Equivalent (sphere) diameter (cm)	Porosity (%)	Bulk density (g/cm^3)	Particle density (g/m^3)
Anderson 1-6403	**Whole core**	9.29	1.529	2.633	2.674
	Plug	2.72±0.415	3.315±0.031	2.558±0.093	2.646±0.097
	1-cm cube	1.23±0.018	4.447±0.486	2.525±0.180	2.643±0.201
Anderson 2-6335	**Whole core**	9.91±0.035	1.464±0.134	2.717±0.026	2.736±0.030
	Plug	3.22±0.117	1.290±0.218	2.741±0.013	2.777±0.015
	1-cm cube	1.26±0.037	1.771±0.458	2.596±0.218	2.644±0.228
Anderson 2-6355	**Whole core**	9.76	0.727	2.681	2.700
	Plug	3.30±0.113	2.820±0.881	2.673±0.032	2.751±0.026
	1-cm cube	1.24±0.041	3.570±0.705	2.570±0.172	2.665±0.185
Anderson 2-6367	**Whole core**	9.38±0.003	0.228±0.019	2.757±0.003	2.764±0.003
	Plug	3.15±0.025	0.371±0.155	2.757±0.022	2.768±0.018
	1-cm cube	1.25±0.018	0.551±0.121	2.588±0.156	2.603±0.156
Anderson 2-6376	**Whole core**	10.15	0.347	2.716	2.726
	Plug	3.29±0.069	0.983±.0347	2.686±0.046	2.735±0.064
	1-cm cube	1.27±0.012	1.431±0.319	2.613±0.161	2.651±0.182
Anderson 2-6385	**Whole core**	8.76	0.33	2.771	2.780
	Plug	2.89±0.063	0.469±0.090	2.745±0.023	2.758±0.025
	1-cm cube	1.21±0.038	1.058±0.243	2.697±0.161	2.726±0.167
Anderson 2-6402	**Whole core**	9.71	0.926	2.728	2.753
	Plug	2.91±0.338	1.518±0.147	2.702±0.034	2.744±0.037
	1-cm cube	1.21±0.035	1.320±0.326	2.652±0.197	2.688±0.206

4.4 Mercury Intrusion Capillary Pressure (MICP)

A variety of pore structure properties including bulk density, porosity, pore-throat size distribution, permeability, and tortuosity can be obtained through MICP tests. The results from MICP analyses performed on all seven samples are shown in Table 7. Porosity values from MICP analyses range from 0.24-3.94% and the total pore area vary from 0.001-0.467 m^2/g. Bulk density values differ from 2.684-2.869 g/cm^3. An example of inflection points, determined by peaks in intrusion pressure relating to the pore-throat diameter connecting pore networks, is shown in Figure 16.

Pore-throat diameters can be qualitatively related to various pore types (Hu et al., 2017): 100-1 μm relate to micro-fractures and laminations in the rock, 0.05-1 μm relate to intergranular pores, 0.01-0.05 μm relate to intragranular pores, 0.005-0.01 μm relate to organic matter-hosted pores, and 0.0028-0.005 μm relate to inter-clay platelet pores. Pore-throat size distribution results from MICP analyses are shown in Table 8 and Figure 17. Intergranular pores are the dominant pore type for all samples tested. MICP tests for sample Anderson 2-6335 will be re-analyzed.

Table 7: Compilation of MICP results.

Sample ID	Total Intrusion Volume (cm^3/g)	Total pore area (m^2/g)	Bulk density (g/cm^3)	Particle density (g/cm^3)	Porosity (%)	Permeability (mD)	Pore-throat interval	Pore Volume (%)	Permeability (mD)	Tortuosity (D0/De)
Anderson 1-6403	0.015	0.440	2.689	2.800	3.94	3.90	10-45 µm	0.073	2.283E+00	5.10
							1-10 µm	0.136	1.711E-01	18.6
							0.1-1 µm	0.446	3.160E-03	137
							10-100 nm	0.361	1.001E-03	244
							5-10 nm	0	0	0
							2.8-5 nm	0	0	0
Anderson 2-6335	0.001	0.000	2.845	2.852	0.24	10.35	100-250 µm	0.210	1.906E+01	3.51
							10-100 µm	0.755	5.435E+00	6.58
							1-10 µm	0.036	0	0
							0.1-1 µm	0	0	0
							10-100 nm	0	0	0
							5-10 nm	0	0	0
							2.8-5 nm	0	0	0
Anderson 2-6355	0.010	0.383	2.771	2.851	2.43	0.89	10-45 µm	0.021	7.116E-01	4.43
							1-10 µm	0.019	2.132E-01	8.09
							0.1-1 µm	0.704	1.450E-03	98.1
							10-100 nm	0.234	0	0
							5-10 nm	0	0	0
							2.8-5 nm	0	0	0
Anderson 2-6367	0.001	0.002	2.833	2.840	0.24	1.51	10-45 µm	0.255	1.445E+00	3.50
							1-10 µm	0.591	1.891E-01	9.68
							0.1-1 µm	0.154	3.503E-03	71.1
							10-100 nm	0	0	0
							5-10 nm	0	0	0
							2.8-5 nm	0	0	0

Table 7 Continued:

Sample ID	Total Intrusion Volume (cm3/g)	Total pore area (m2/g)	Bulk density (g/cm3)	Particle density (g/cm3)	Porosity (%)	Permeability (mD)	Pore-throat region	Pore Volume (%)	Permeability (mD)	Tortuosity (D0/De)
Anderson 2-6376	0.005	0.467	2.812	2.850	1.30	2.67	10-45 µm	0.113	4.135E-01	9.29
							1-10 µm	0.144	2.109E-02	41.2
							0.1-1 µm	0.227	6.063E-03	76.8
							10-100 nm	0.517	3.048E-05	1083
							5-10 nm	0	0	0
							2.8-5 nm	0	0	0
Anderson 2-6385	0.003	0.126	2.830	2.851	0.73	1.53	10-45 µm	0.182	2.104E+00	3.24
							1-10 µm	0.321	3.803E-01	7.61
							0.1-1 µm	0.273	5.923E-03	61.0
							10-100 nm	0.224	1.018E-04	465
							5-10 nm	0	0	0
							2.8-5 nm	0	0	0
Anderson 2-6402	0.003	0.167	2.864	2.891	0.95	2.13	10-45 µm	0.136	1.978E+00	3.90
							1-10 µm	0.204	1.966E+01	12.36
							0.1-1 µm	0.205	1.024E-03	171
							10-100 nm	0.434	7.691E-05	625
							5-10 nm	0	0	0
							2.8-5 nm	0	0	0

A)

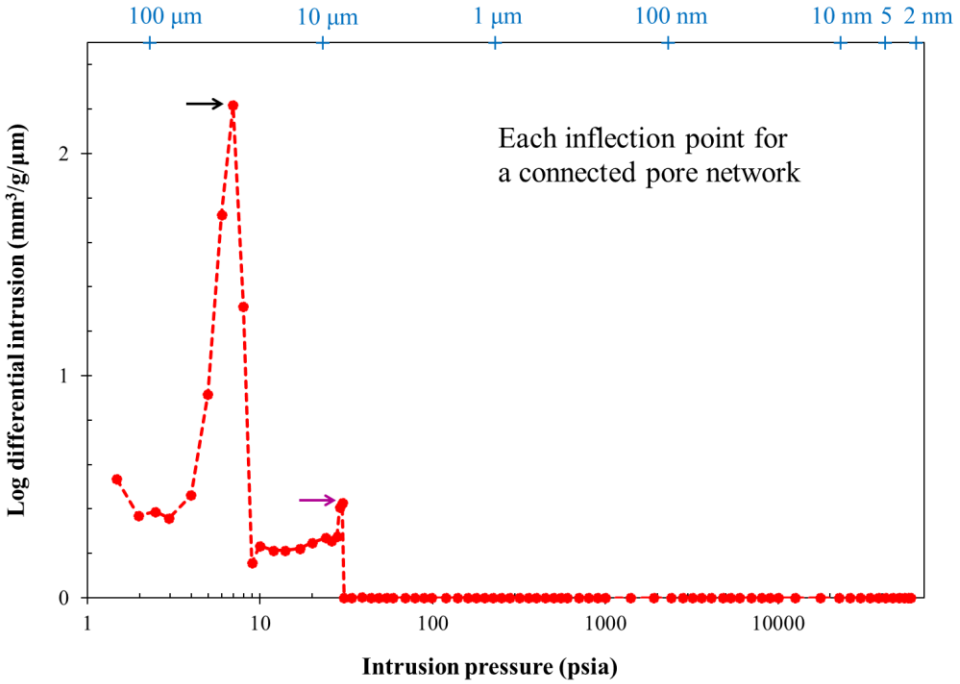
100 µm
10 µm
1 µm
100 nm
10 nm
5
2 nm
Each inflection point for
a connected pore network
Log differential intrusion (mm³/g/µm)
2
1
0
1
10
100
1000
10000
Intrusion pressure (psia)

B)

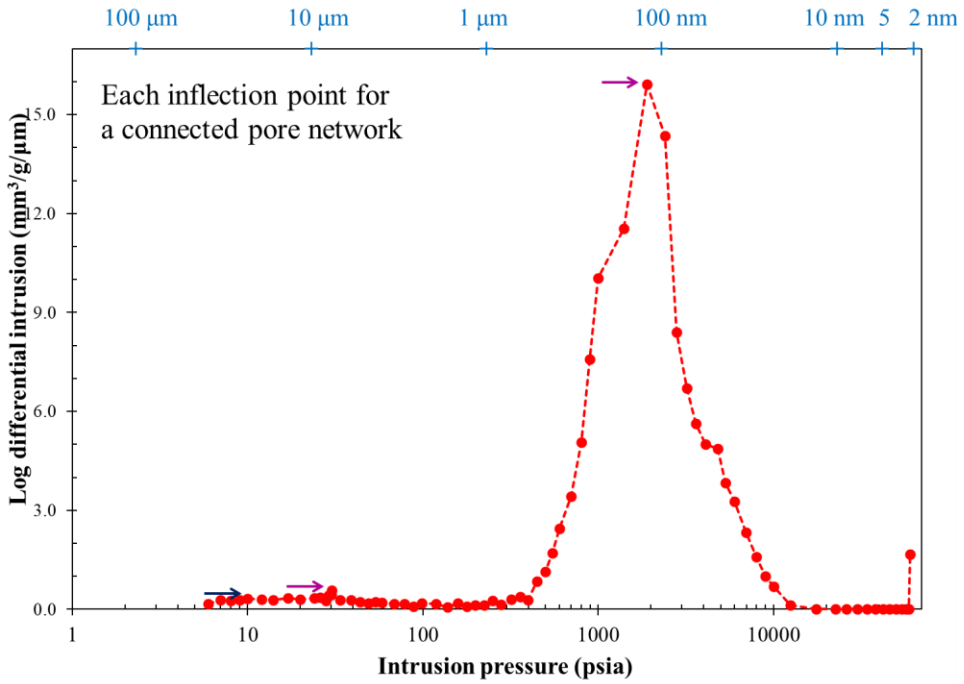
100 µm
10 µm
1 µm
100 nm
10 nm
5
2 nm
Each inflection point for
a connected pore network
Log differential intrusion (mm³/g/µm)
15.0
12.0
9.0
6.0
3.0
0.0
1
10
100
1000
10000
Intrusion pressure (psia)

C)

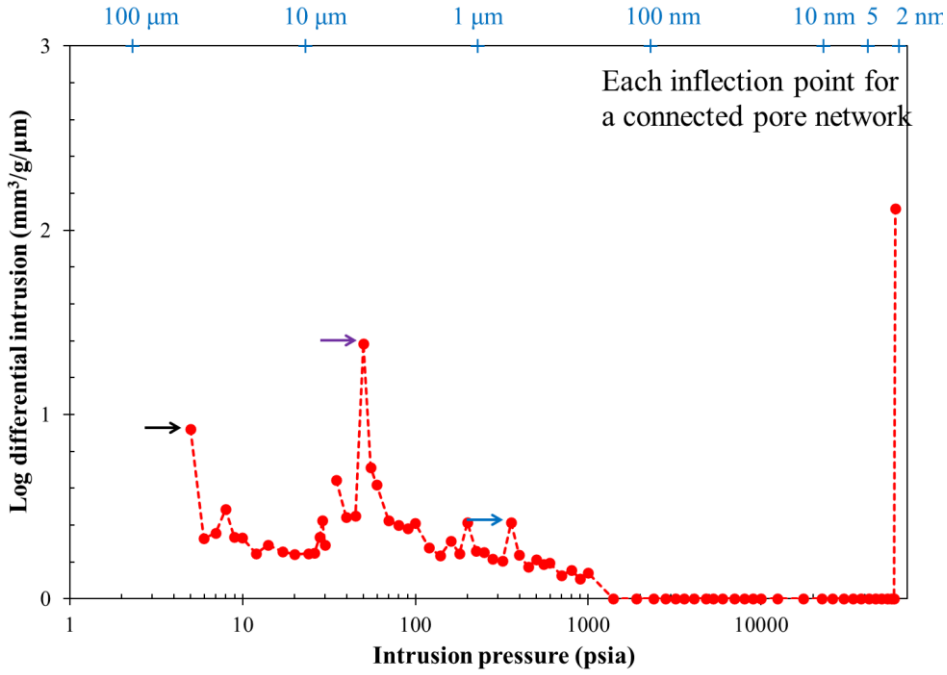
100 µm
10 µm
1 µm
100 nm
10 nm
5
2 nm
Each inflection point for
a connected pore network
Log differential intrusion (mm³/g/µm)
Intrusion pressure (psia)
0
1
2
3
1
10
100
1000
10000

D)

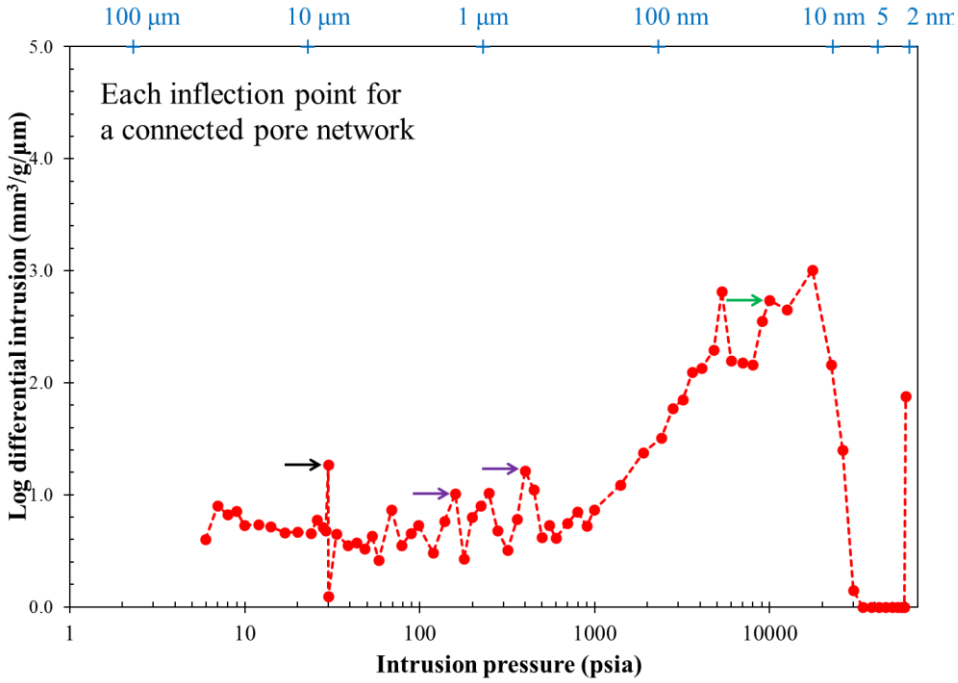
100 µm
10 µm
1 µm
100 nm
10 nm
5
2 nm
Each inflection point for
a connected pore network
Log differential intrusion (mm³/g/µm)
Intrusion pressure (psia)
0.0
1.0
2.0
3.0
4.0
5.0
1
10
100
1000
10000

E)

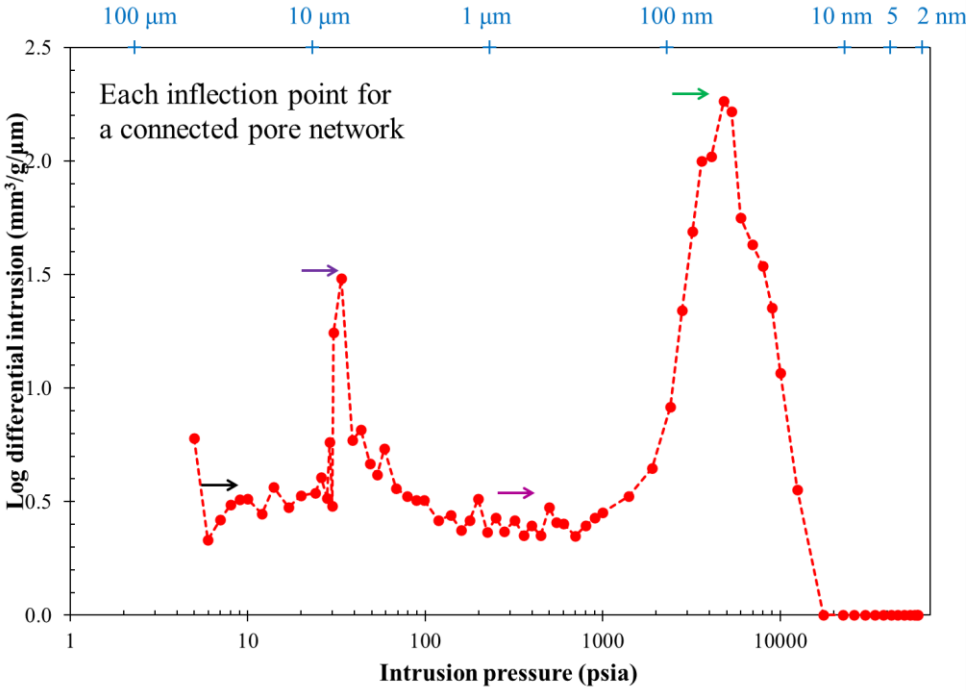
100 µm
10 µm
1 µm
100 nm
10 nm
5
2 nm
Each inflection point for
a connected pore network
Log differential intrusion (mm³/g/µm)
Intrusion pressure (psia)
0.0
0.5
1.0
1.5
2.0
2.5
1
10
100
1000
10000

F)

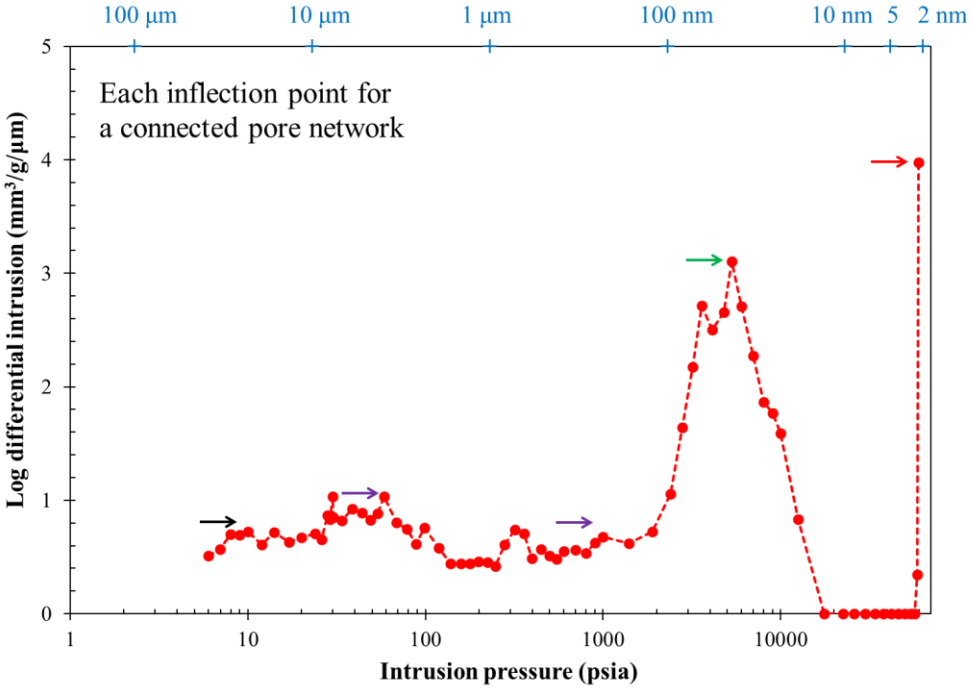
100 µm
10 µm
1 µm
100 nm
10 nm
5
2 nm
Each inflection point for
a connected pore network
Log differential intrusion (mm³/g/µm)
Intrusion pressure (psia)
0
1
2
3
4
5
1
10
100
1000
10000

G)

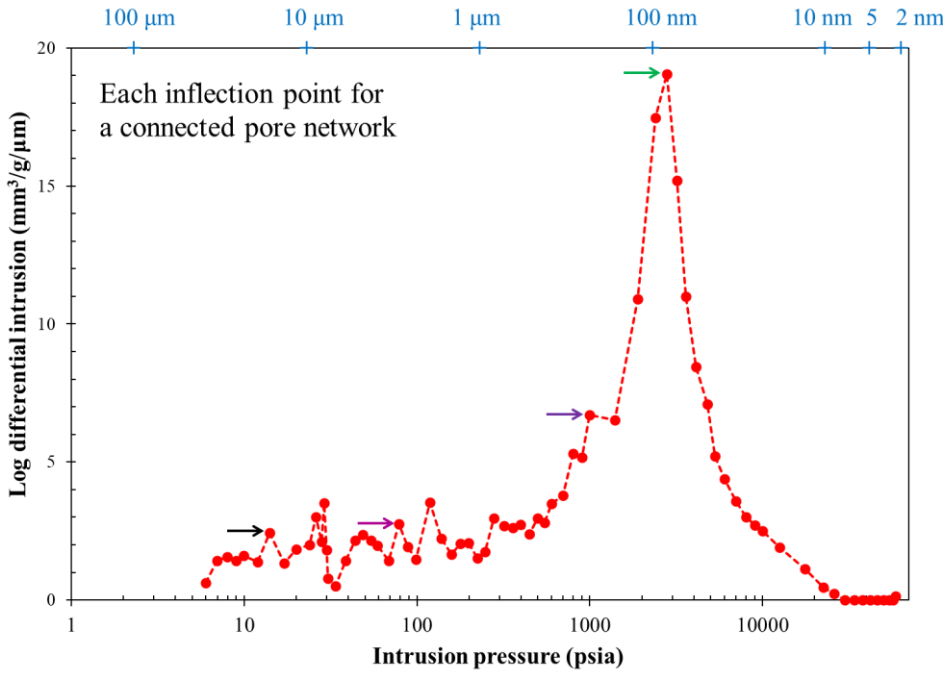

Figure 16: MICP plot of Anderson 2-6335 (A), Anderson 2-6355 (B), Anderson 2-6367 (C), Anderson 2-6376 (D), Anderson 2-6385 (E), Anderson 2-6402 (F), and Anderson 1-6403 (G) with arrows showing inflection points. Pore-throat sizes correlated to the intrusion pressure are displayed on the 2nd X-axis.

Table 8: Pore-throat size distribution from MICP analyses.

Sample ID	Pore-throat size interval (µm)				
	10-45	**1-10**	**0.1-1**	**0.05-0.1**	**0.01-0.05**
Anderson 1-6403	7.3	13.6	44.6	22.1	14
Anderson 2-6335	96.5	3.6			
Anderson 2-6355	2.1	1.9	70.4	15.4	8.1
Anderson 2-6367	25.5	59.1	15.4		
Anderson 2-6376	11.3	14.4	22.7	10.2	41.5
Anderson 2-6385	18.2	32.1	27.3	22.4	
Anderson 2-6402	13.6	20.4	20.5	15.8	27.6
Anderson 1-6403	7.3	13.6	44.6	22.1	14

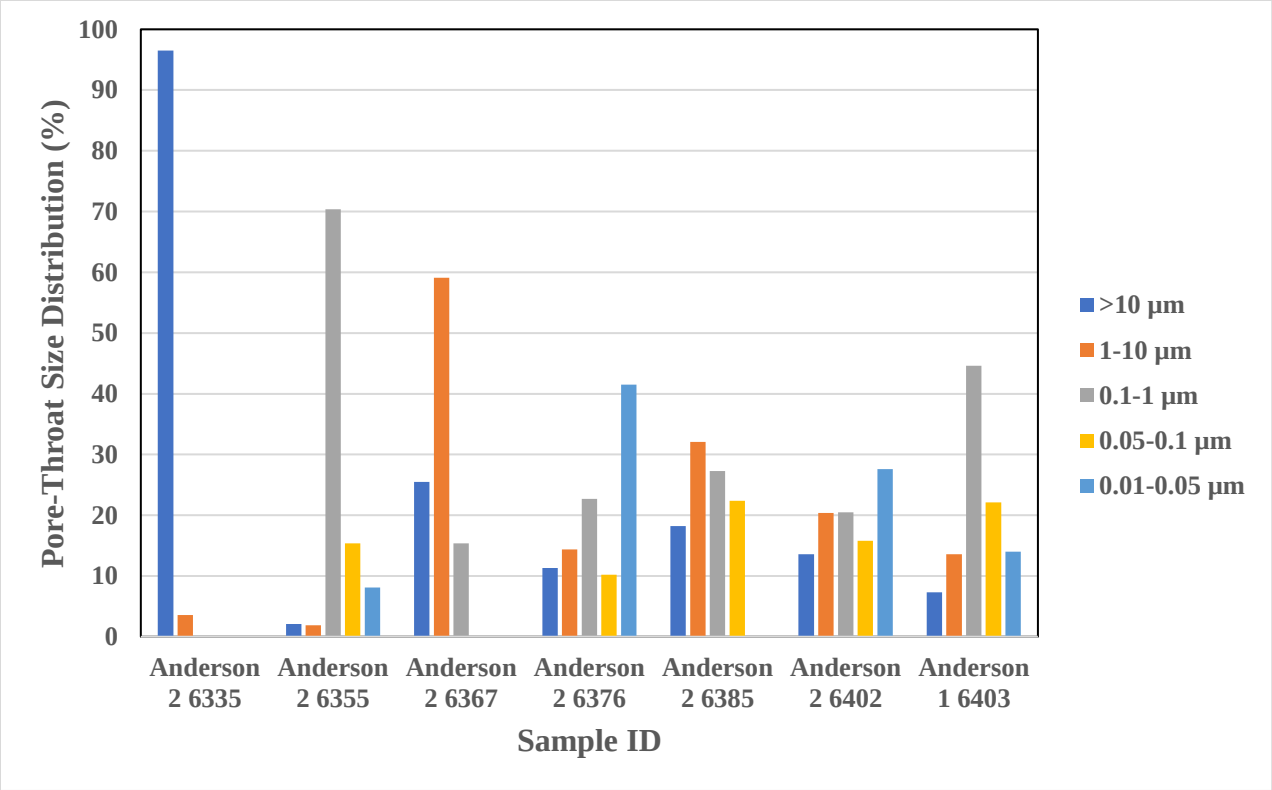

Figure 17: Pore-throat size distribution from MICP analyses.

4.5 Fluid Imbibition and Vapor Absorption

Fluid Imbibition

Cube sized samples for all seven samples were used for imbibition with DIW and vapor absorption with DIW and DT2. Imbibition experiments were run for a duration of 6 hrs and 24 hrs to assess pore connectivity. Plots of imbibition show the log time (min) vs. log cumulative imbibition (mm). Typically, 2 to 4 slopes showing different stages of fluid interaction with the sample (Yang et al., 2017). Stage I represented by Type I slope signifies the sample touching the fluid's surface during the first few seconds of the experiment. Stage II shown by Type II slope correlates to the fluid imbibed into the sample's edge accessible pores through either microfractures or laminations. Stage III indicated by Type III slope denotes the fluid migration through the pore network of the sample. Stage IV marked by Type IV slope is the final stage of the experiment when the fluid reaches the top of the sample (Hu et al., 2001).

Type III slopes which represent the fluid migration through the pore networks are used to determine pore connectivity of sample's interior region. Averages of Type III slopes for each imbibition run on each sample are displayed in Table 9 as well as the connectivity classification. Type III slope values of 0.47 or greater indicate high pore connectivity, values in between 0.47 and 0.30 show intermediate pore connectivity, and values less than 0.30 show low pore connectivity (Hu et al., 2012). Samples Anderson 2-6335, 2-6367, 2-6376, and 2-6402 display a low connectivity and samples Anderson 2-6355, 2-6385, and Anderson 1-6403 show an intermediate connectivity. Imbibition plots are shown in Figures 18 (A-M).

Table 9: Pore connectivity slope results from DIW imbibition.

Sample ID	Type III slope	Connectivity classification
Anderson 1-6403	0.306±0.018	Intermediate
Anderson 2-6335	0.203±0.078	Low
Anderson 2-6355	0.351±0.066	Intermediate
Anderson 2-6367	0.271±0.043	Low
Anderson 2-6376	0.252±0.043	Low
Anderson 2-6385	0.453±0.190	Intermediate
Anderson 2-6402	0.275	Low

A)

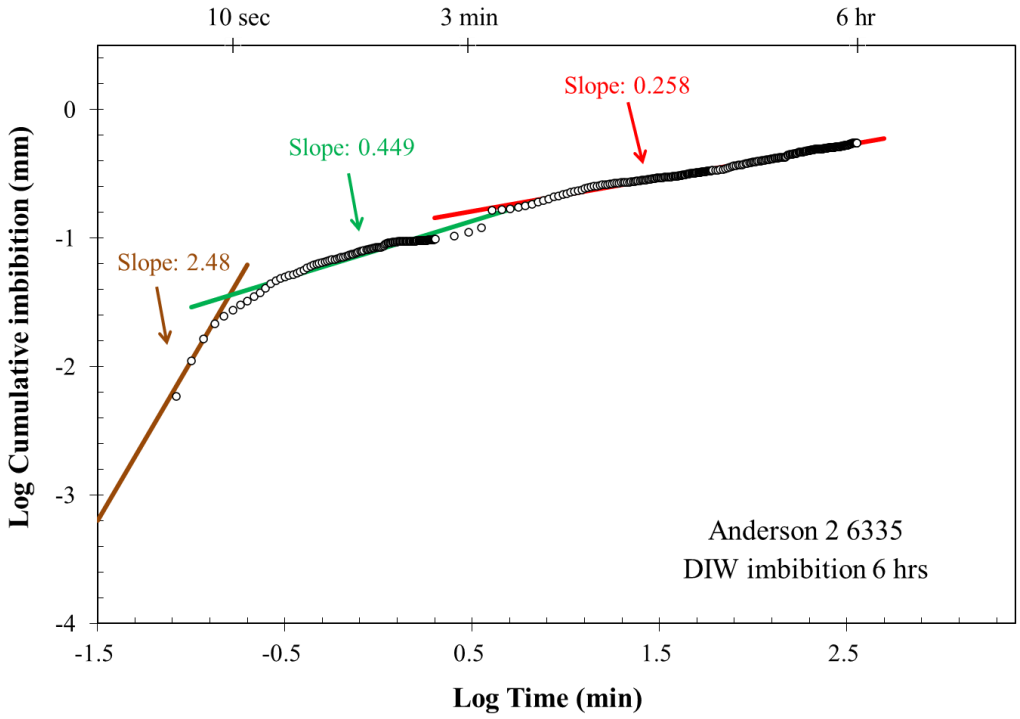
10 sec
3 min
6 hr
Slope: 0.258
Slope: 0.449
Slope: 2.48
0
-1
-2
-3
-4
Log Cumulative imbibition (mm)
Anderson 2 6335
DIW imbibition 6 hrs
-1.5
-0.5
0.5
1.5
2.5
Log Time (min)

B)

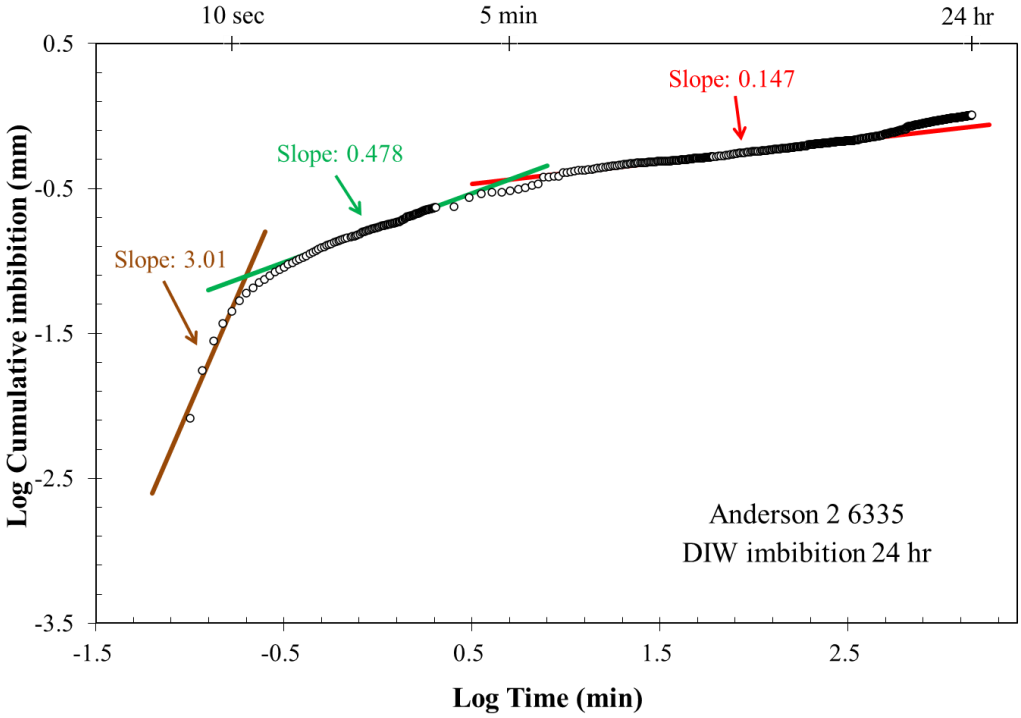
10 sec
5 min
24 hr
Slope: 0.147
Slope: 0.478
Slope: 3.01
0.5
-0.5
-1.5
-2.5
-3.5
Log Cumulative imbibition (mm)
Anderson 2 6335
DIW imbibition 24 hr
-1.5
-0.5
0.5
1.5
2.5
Log Time (min)

C)

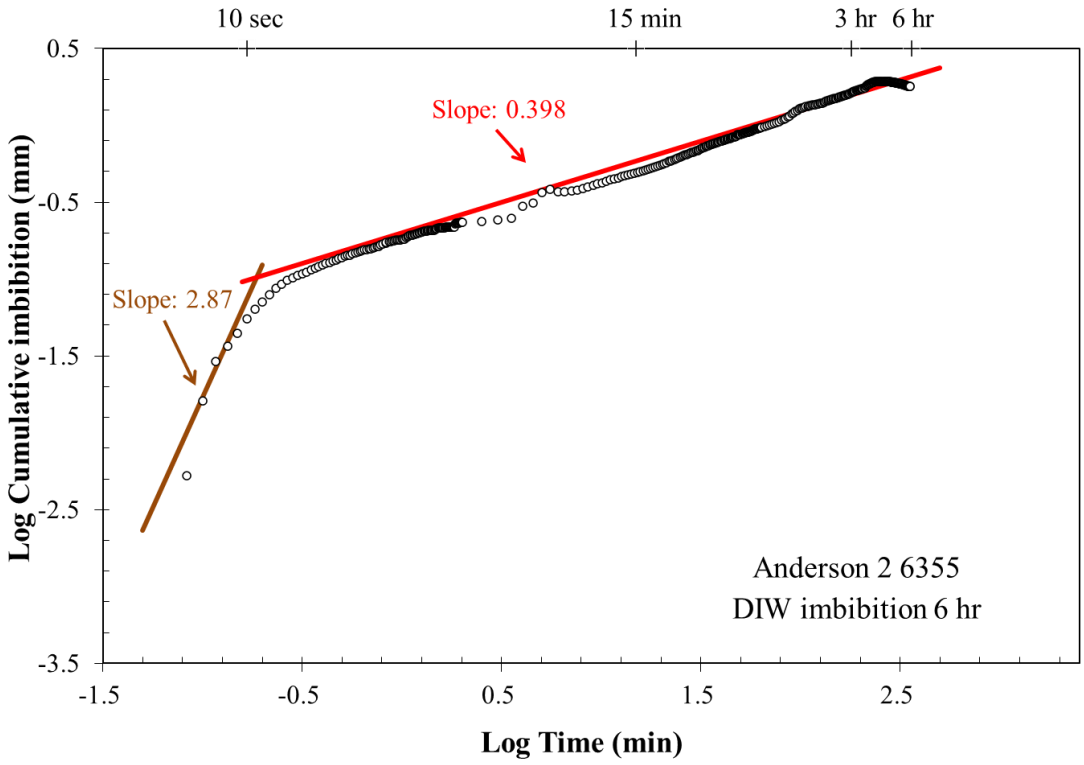
10 sec
15 min
3 hr
6 hr
0.5
-0.5
-1.5
-2.5
-3.5
Slope: 0.398
Slope: 2.87
Log Cumulative imbibition (mm)
Anderson 2 6355
DIW imbibition 6 hr
-1.5
-0.5
0.5
1.5
2.5
Log Time (min)

D)

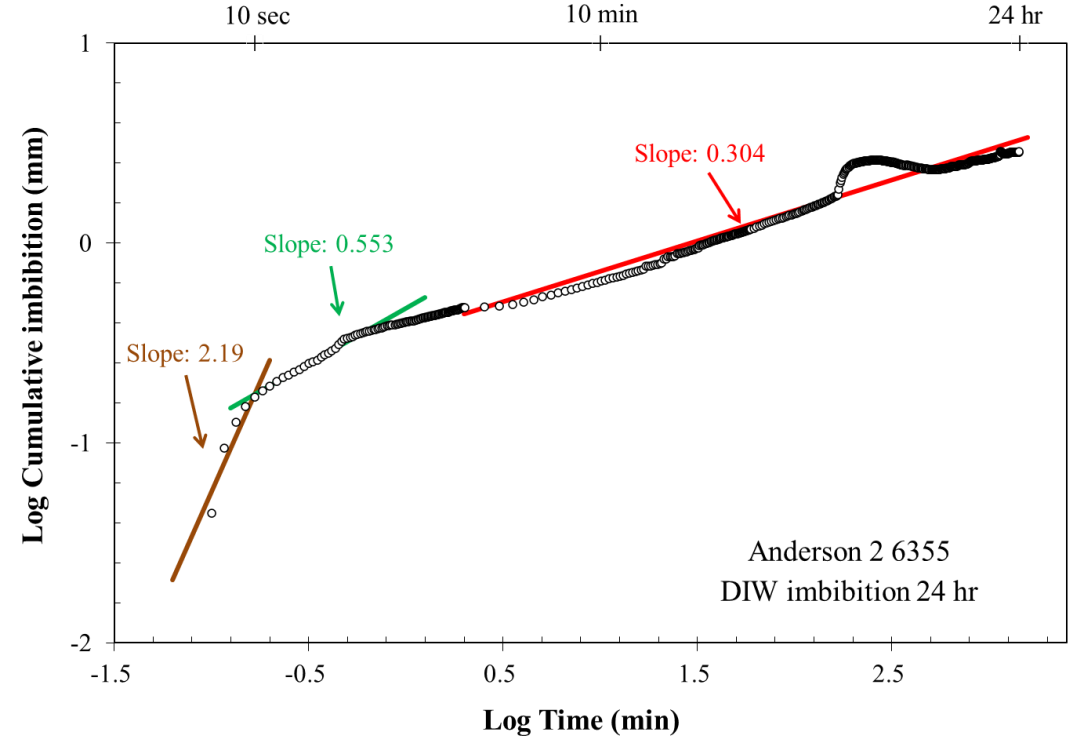
10 sec
10 min
24 hr
1
0
-1
-2
Slope: 0.304
Slope: 0.553
Slope: 2.19
Log Cumulative imbibition (mm)
Anderson 2 6355
DIW imbibition 24 hr
-1.5
-0.5
0.5
1.5
2.5
Log Time (min)

E)

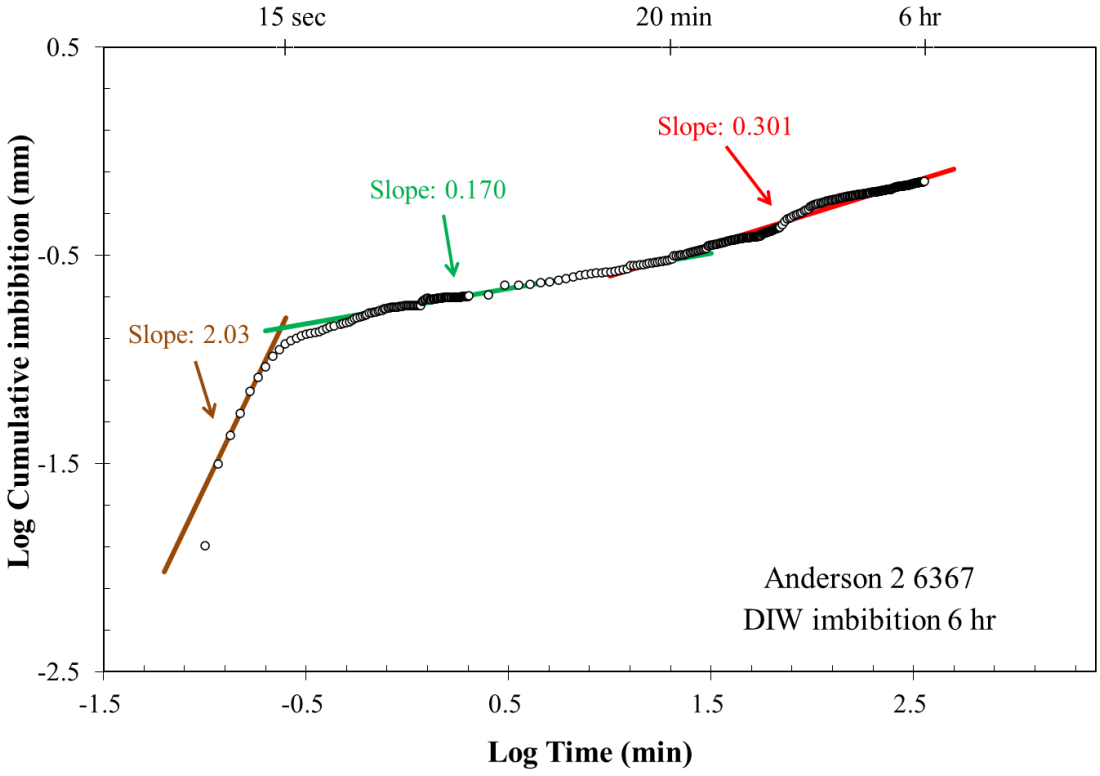
15 sec
20 min
6 hr
0.5
-0.5
-1.5
-2.5
Log Cumulative imbibition (mm)
Slope: 0.301
Slope: 0.170
Slope: 2.03
Anderson 2 6367
DIW imbibition 6 hr
-1.5
-0.5
0.5
1.5
2.5
Log Time (min)

F)

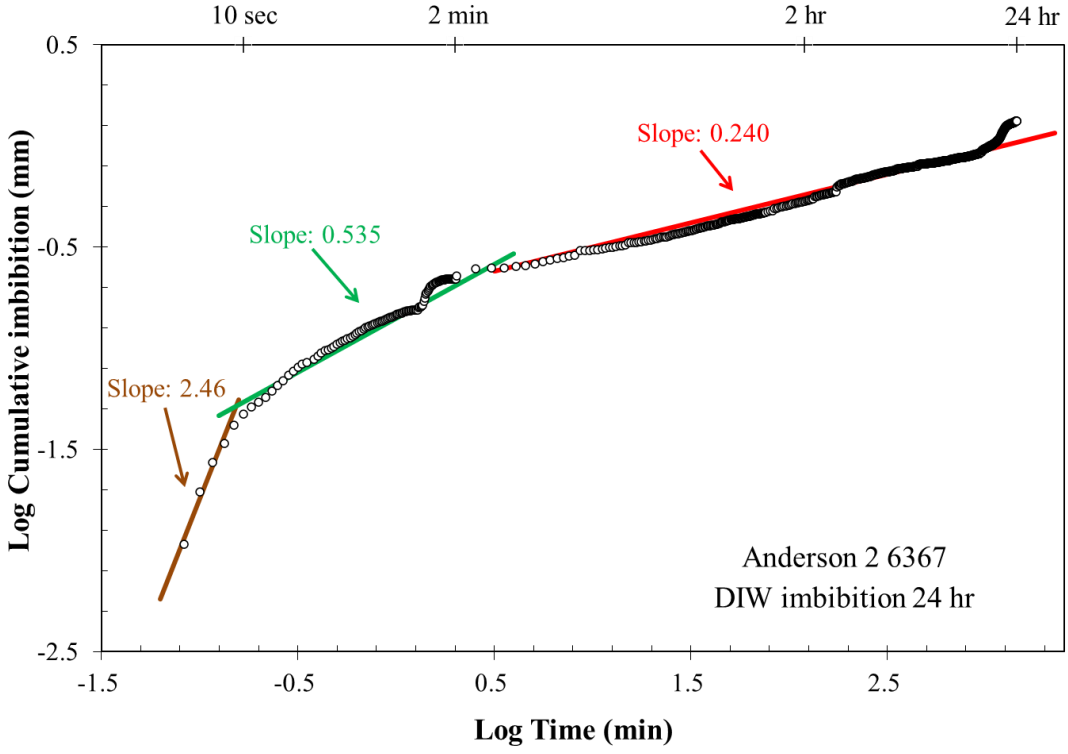
10 sec
2 min
2 hr
24 hr
0.5
-0.5
-1.5
-2.5
Log Cumulative imbibition (mm)
Slope: 0.240
Slope: 0.535
Slope: 2.46
Anderson 2 6367
DIW imbibition 24 hr
-1.5
-0.5
0.5
1.5
2.5
Log Time (min)

G)

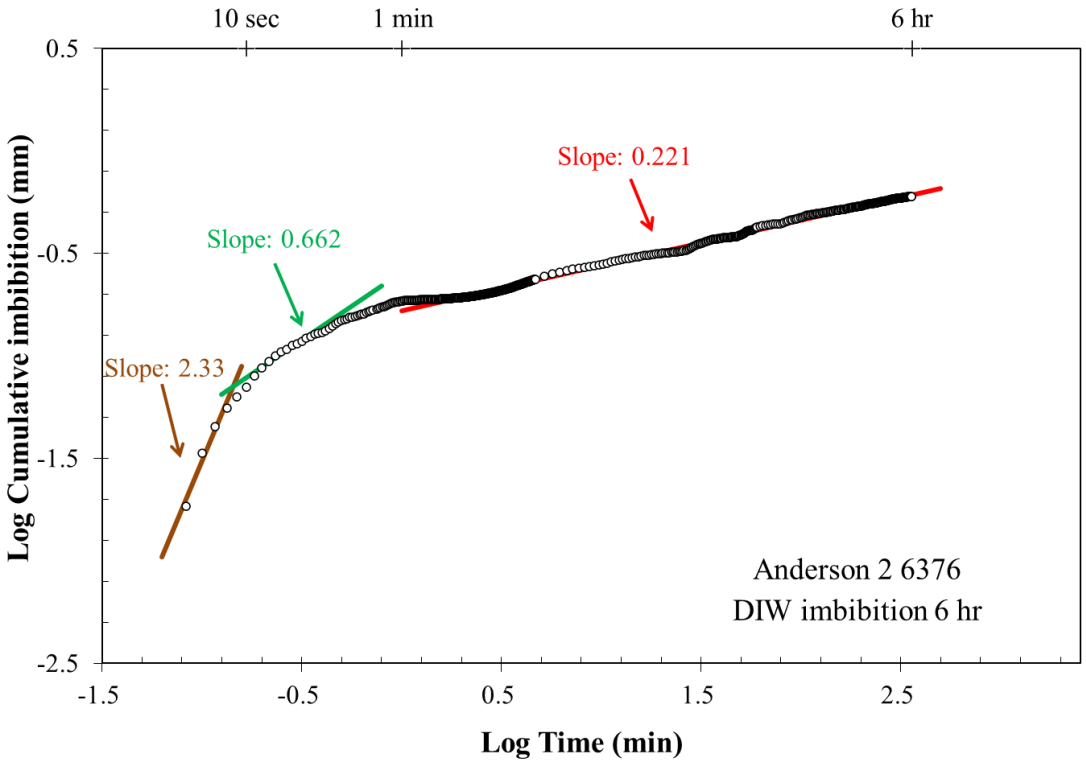
10 sec
1 min
6 hr
0.5
-0.5
-1.5
-2.5
Log Cumulative imbibition (mm)
Slope: 0.221
Slope: 0.662
Slope: 2.33
Anderson 2 6376
DIW imbibition 6 hr
-1.5
-0.5
0.5
1.5
2.5
Log Time (min)

H)

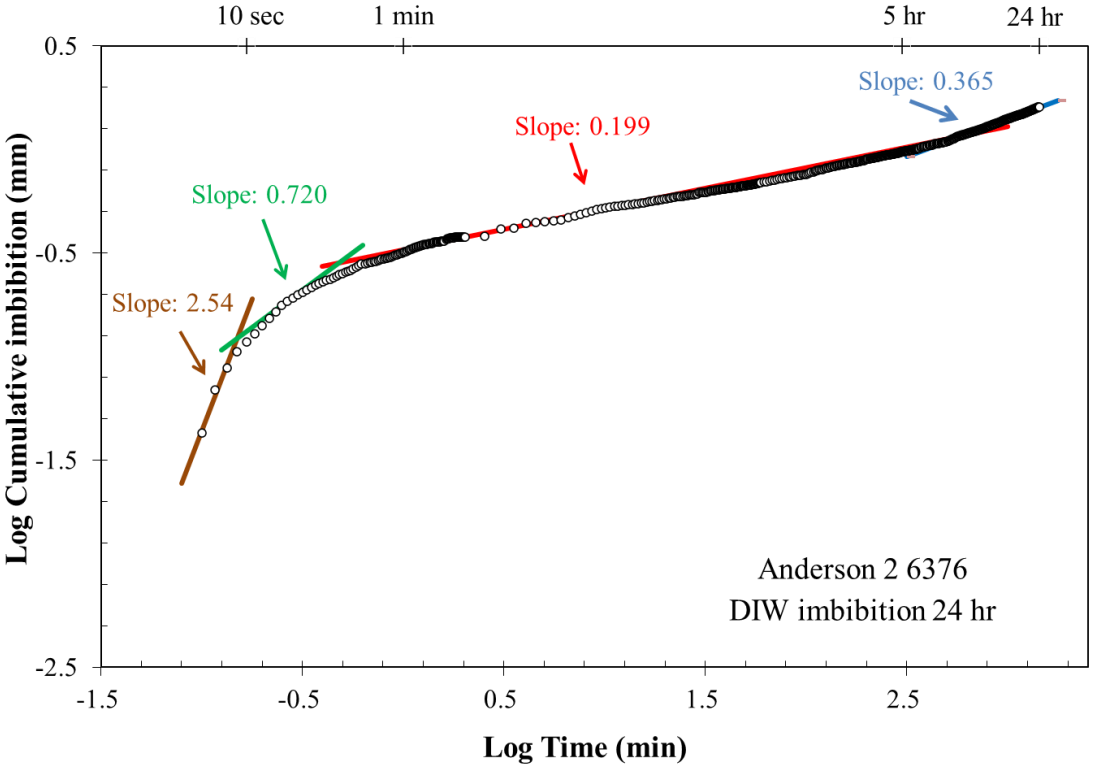
10 sec
1 min
5 hr
24 hr
0.5
-0.5
-1.5
-2.5
Log Cumulative imbibition (mm)
Slope: 0.365
Slope: 0.199
Slope: 0.720
Slope: 2.54
Anderson 2 6376
DIW imbibition 24 hr
-1.5
-0.5
0.5
1.5
2.5
Log Time (min)

I)

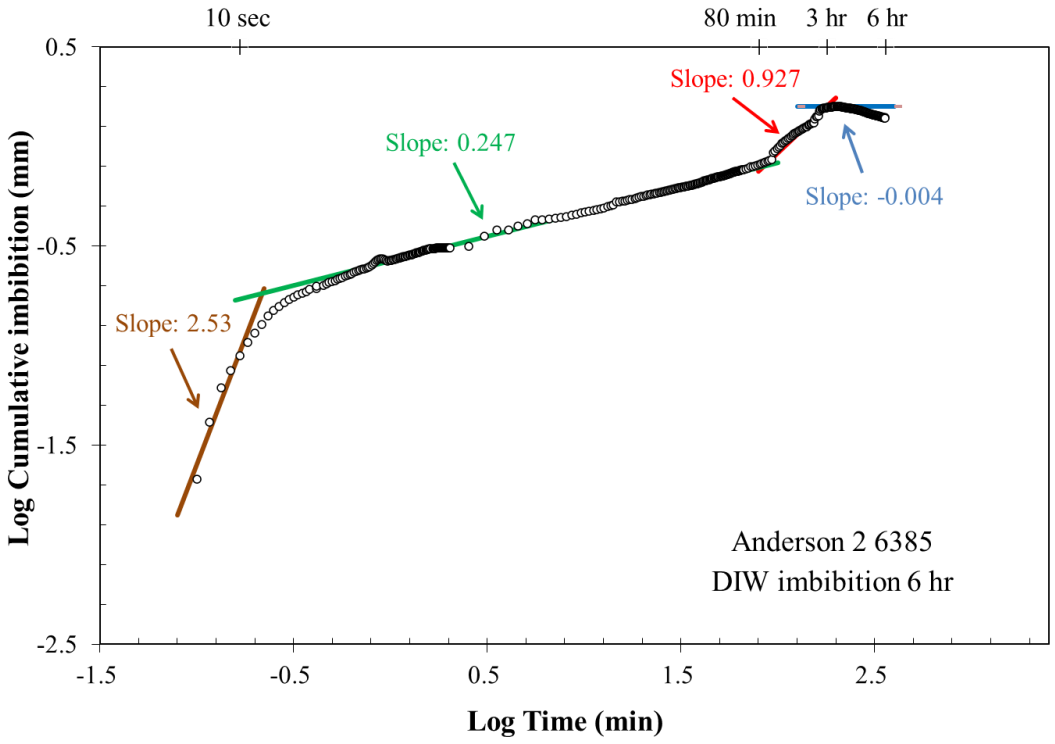
10 sec
80 min
3 hr
6 hr
0.5
-0.5
-1.5
-2.5
Slope: 0.927
Slope: 0.247
Slope: -0.004
Slope: 2.53
Anderson 2 6385
DIW imbibition 6 hr
-1.5
-0.5
0.5
1.5
2.5
Log Cumulative imbibition (mm)
Log Time (min)

J)

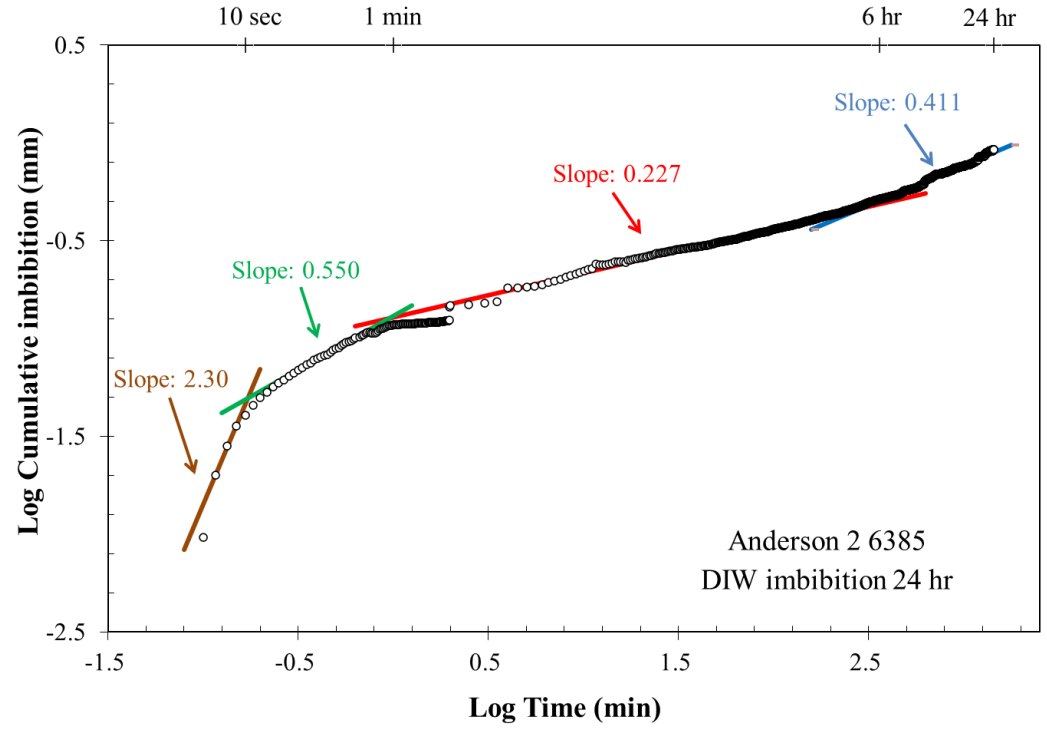
10 sec
1 min
6 hr
24 hr
0.5
-0.5
-1.5
-2.5
Slope: 0.411
Slope: 0.227
Slope: 0.550
Slope: 2.30
Anderson 2 6385
DIW imbibition 24 hr
-1.5
-0.5
0.5
1.5
2.5
Log Cumulative imbibition (mm)
Log Time (min)

K)

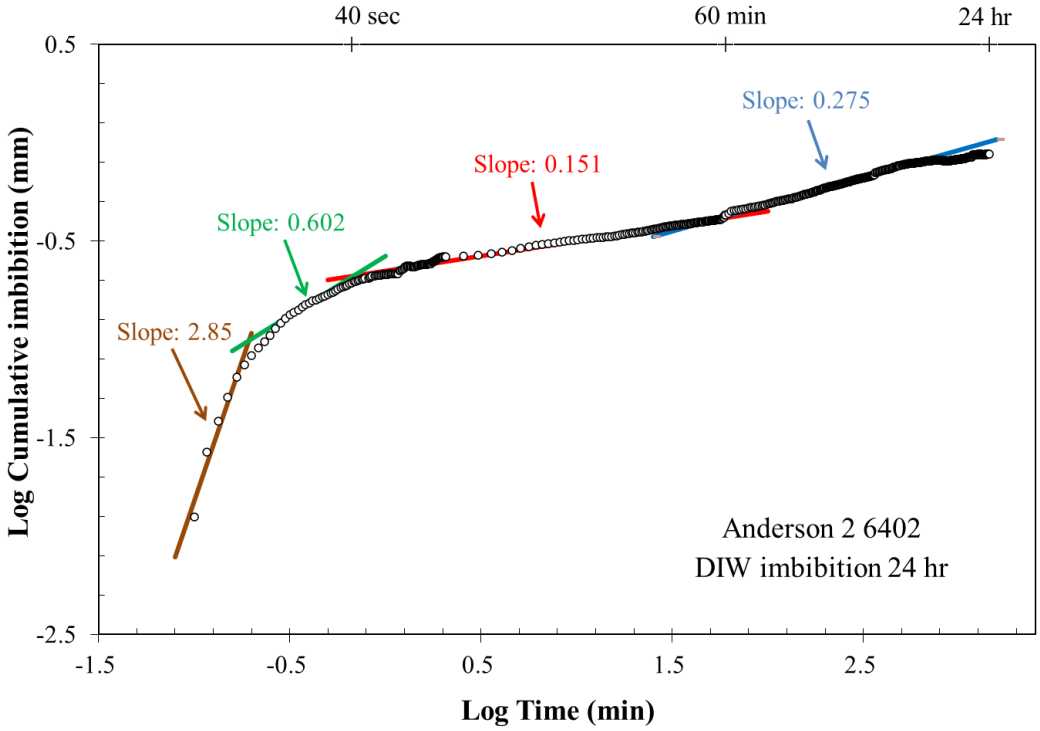
40 sec
60 min
24 hr
0.5
-0.5
-1.5
-2.5
Log Cumulative imbibition (mm)
Slope: 0.275
Slope: 0.151
Slope: 0.602
Slope: 2.85
Anderson 2 6402
DIW imbibition 24 hr
-1.5
-0.5
0.5
1.5
2.5
Log Time (min)

L)

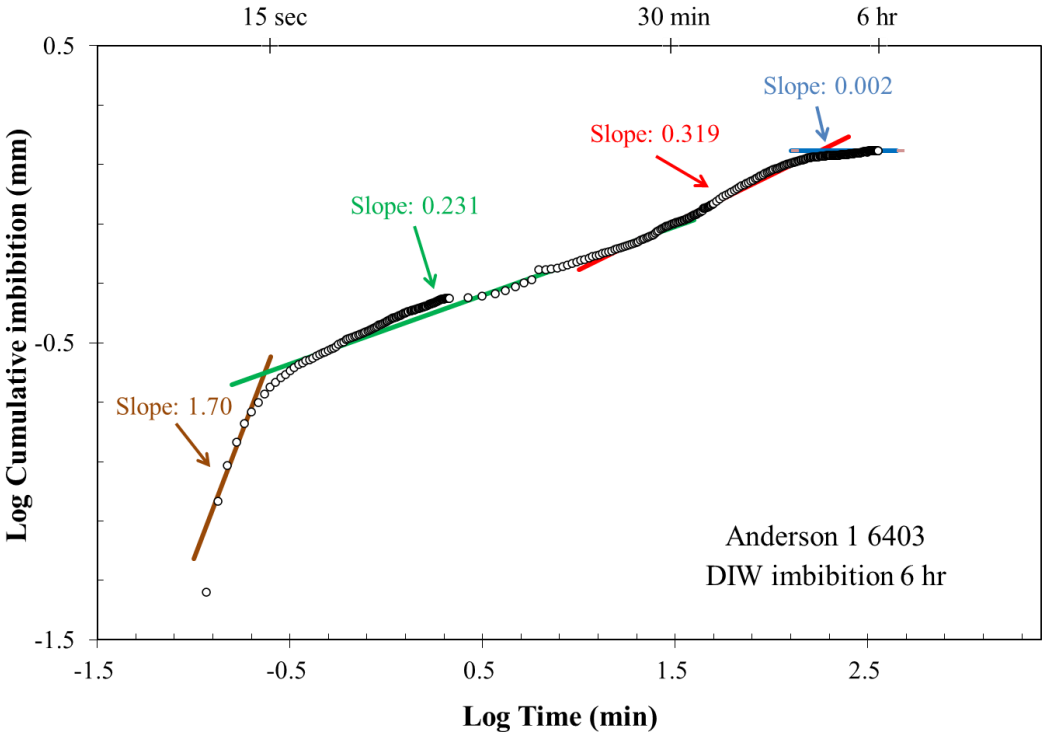
15 sec
30 min
6 hr
0.5
-0.5
-1.5
Log Cumulative imbibition (mm)
Slope: 0.002
Slope: 0.319
Slope: 0.231
Slope: 1.70
Anderson 1 6403
DIW imbibition 6 hr
-1.5
-0.5
0.5
1.5
2.5
Log Time (min)

M)

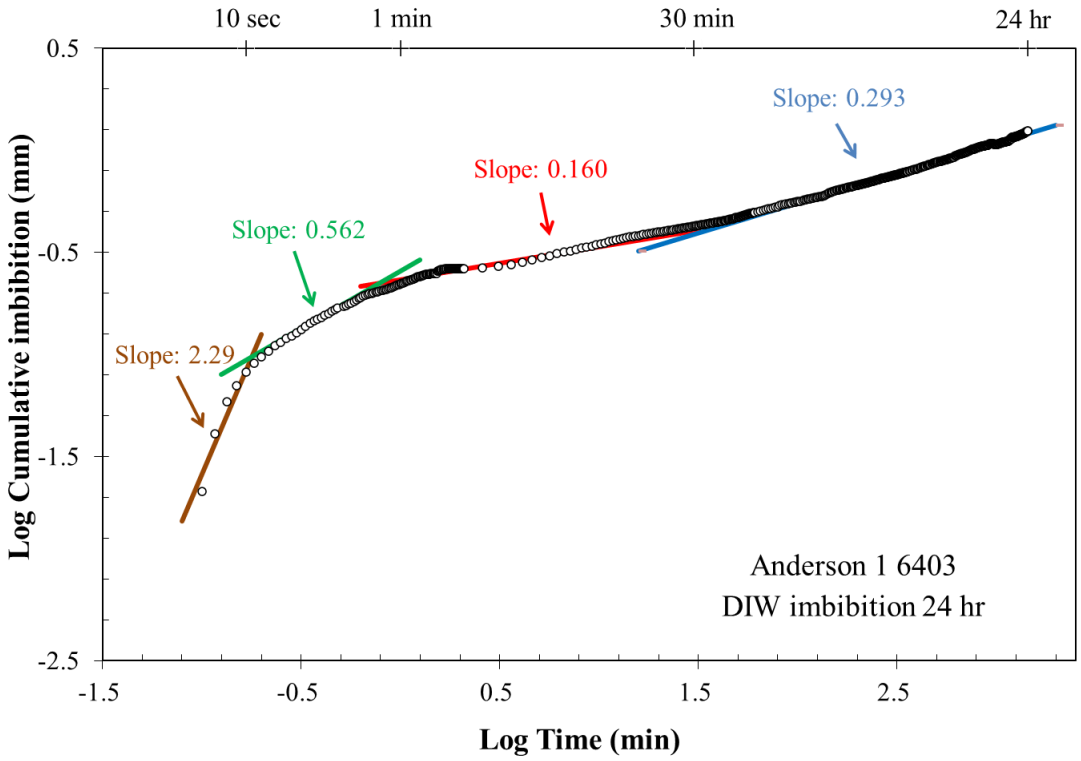

Figure 18: DIW imbibition slopes for Anderson 2-6335 (A-B), Anderson 2-6355 (C-D), Anderson 2-6367 (E-F), Anderson 2-6376 (G-H), Anderson 2-6385 (I-J), Anderson 2-6402 (K), Anderson 1-6403 (L-M).

Vapor Absorption

Using DIW and DT2, vapor absorption experiments were run on all samples except for Anderson 1-6403. Capillary pressure is the primary way fluid migrates through the sample during imbibition tests, however during vapor absorption tests, fluid absorbs into and through the sample via vapor transport and capillary condensation. Type III slopes from vapor absorption using DIW and DT2 are displayed in Table 10. Type III slopes using DIW range from 0.501-0.689 and range from 0.254-0.646 using DT2. Vapor absorption plots are shown in Figures 19-20.

Table 10: Type III slopes from vapor absorption tests for two fluids.

Sample ID	Type III slope-DIW	Type III slope-DT2
Anderson 2-6335	0.691	0.398
Anderson 2-6355	0.592	-
Anderson 2-6367	0.542	-
Anderson 2-6376	0.502	0.646
Anderson 2-6385	0.512	0.424
Anderson 2-6402	0.625	0.676

A)

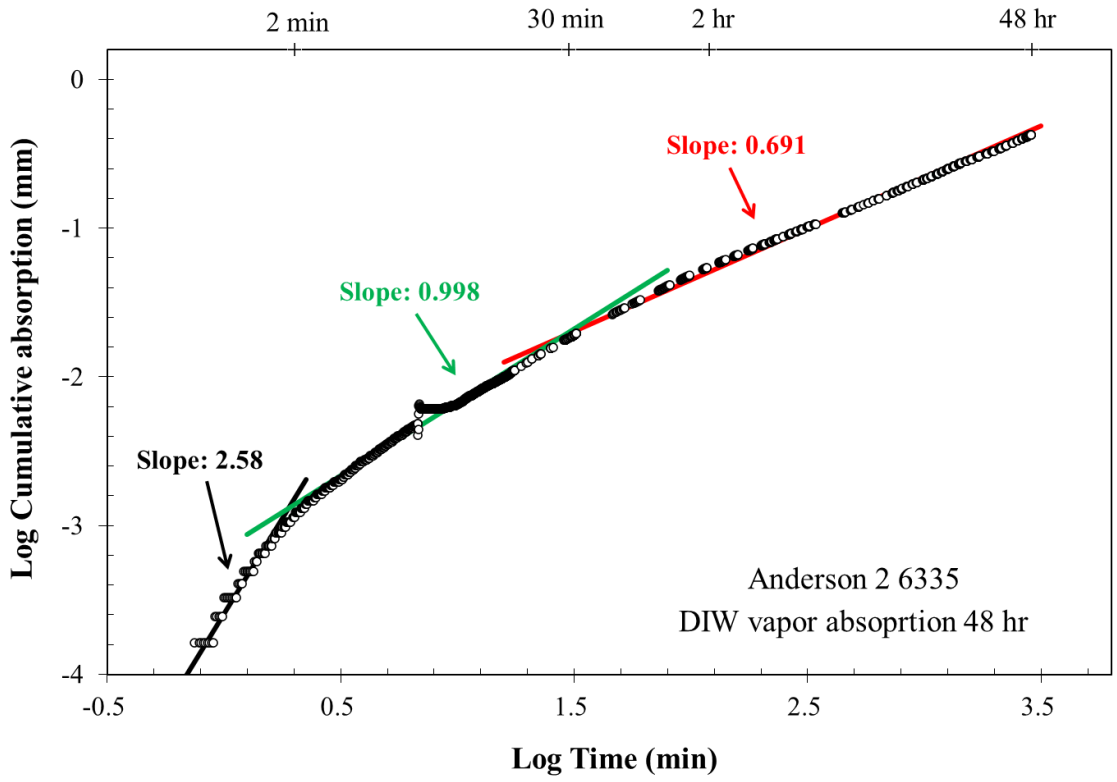
2 min
30 min
2 hr
48 hr
0
-1
-2
-3
-4
Log Cumulative absorption (mm)
Slope: 0.691
Slope: 0.998
Slope: 2.58
Anderson 2 6335
DIW vapor absoprtion 48 hr
-0.5
0.5
1.5
2.5
3.5
Log Time (min)

B)

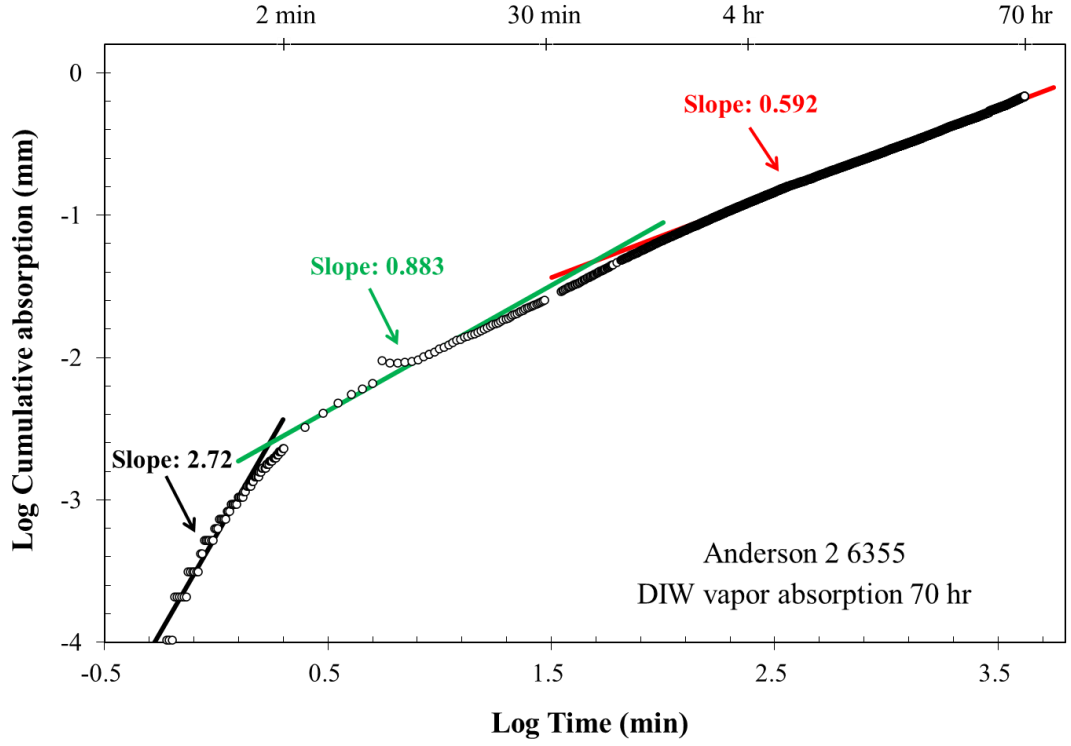
2 min
30 min
4 hr
70 hr
0
-1
-2
-3
-4
Log Cumulative absorption (mm)
Slope: 0.592
Slope: 0.883
Slope: 2.72
Anderson 2 6355
DIW vapor absorption 70 hr
-0.5
0.5
1.5
2.5
3.5
Log Time (min)

C)

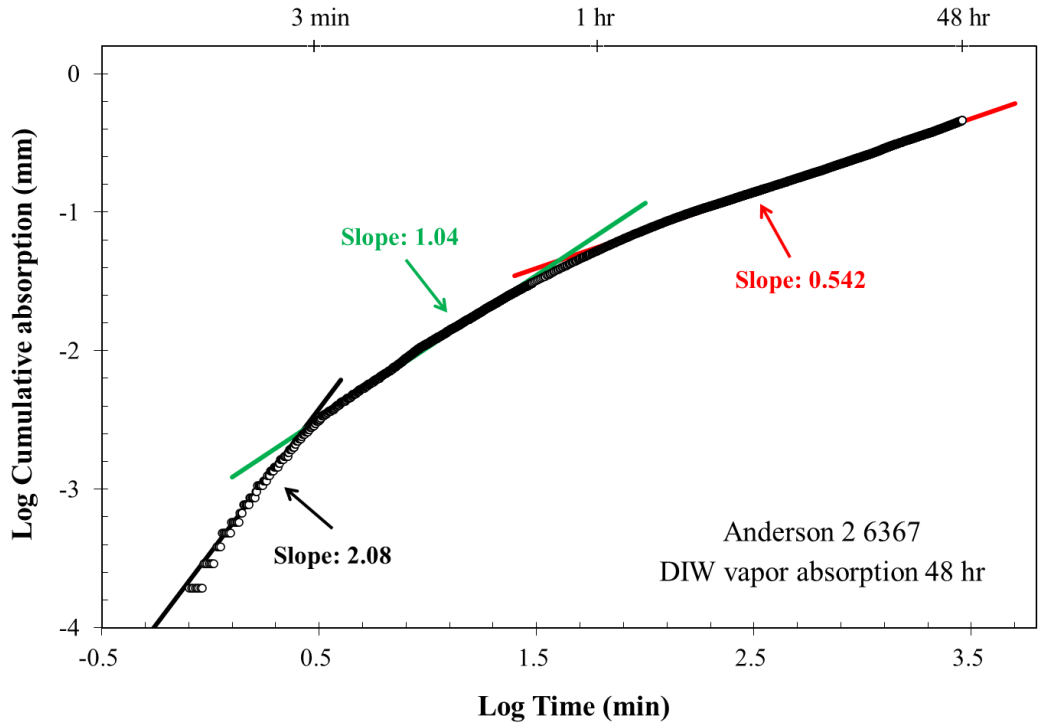
3 min
1 hr
48 hr
0
-1
-2
-3
-4
Log Cumulative absorption (mm)
Slope: 1.04
Slope: 0.542
Slope: 2.08
Anderson 2 6367
DIW vapor absorption 48 hr
-0.5
0.5
1.5
2.5
3.5
Log Time (min)

D)

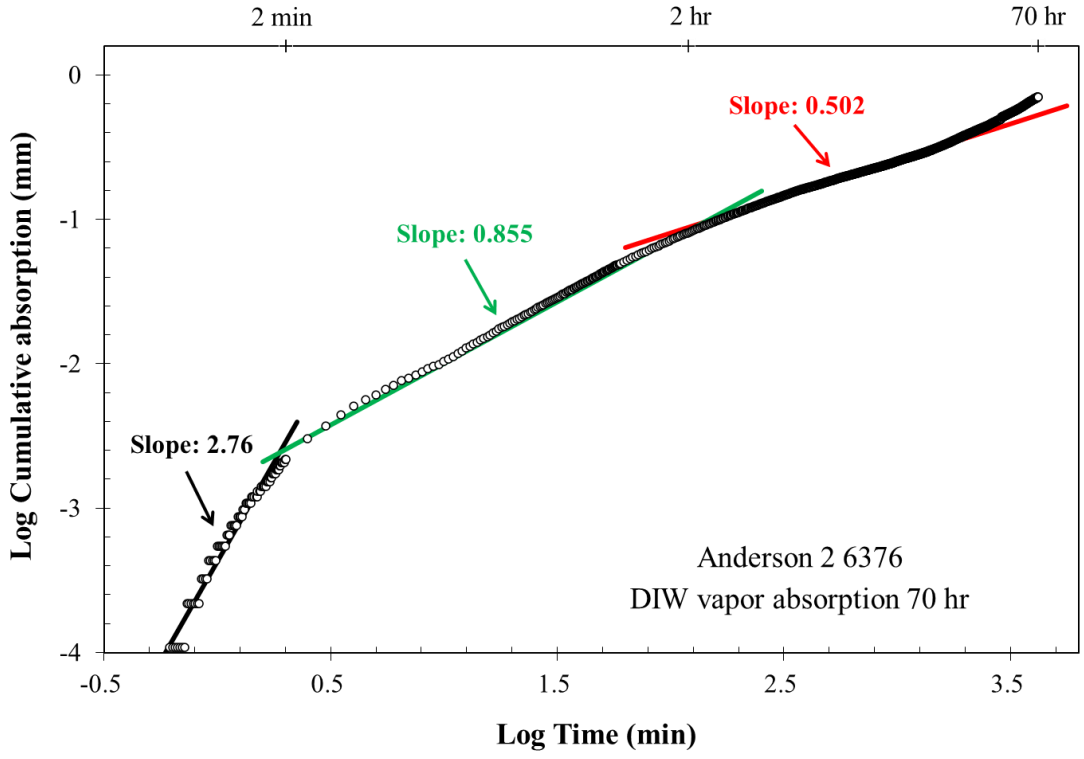
2 min
2 hr
70 hr
0
-1
-2
-3
-4
Log Cumulative absorption (mm)
Slope: 0.502
Slope: 0.855
Slope: 2.76
Anderson 2 6376
DIW vapor absorption 70 hr
-0.5
0.5
1.5
2.5
3.5
Log Time (min)

E)

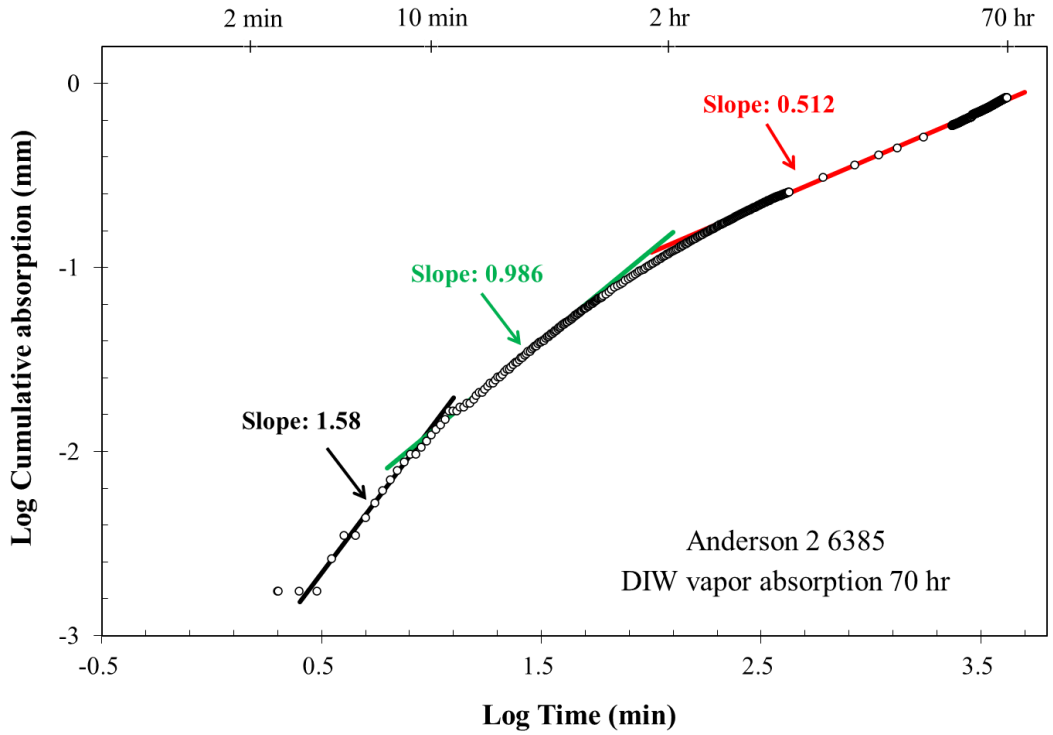

F)

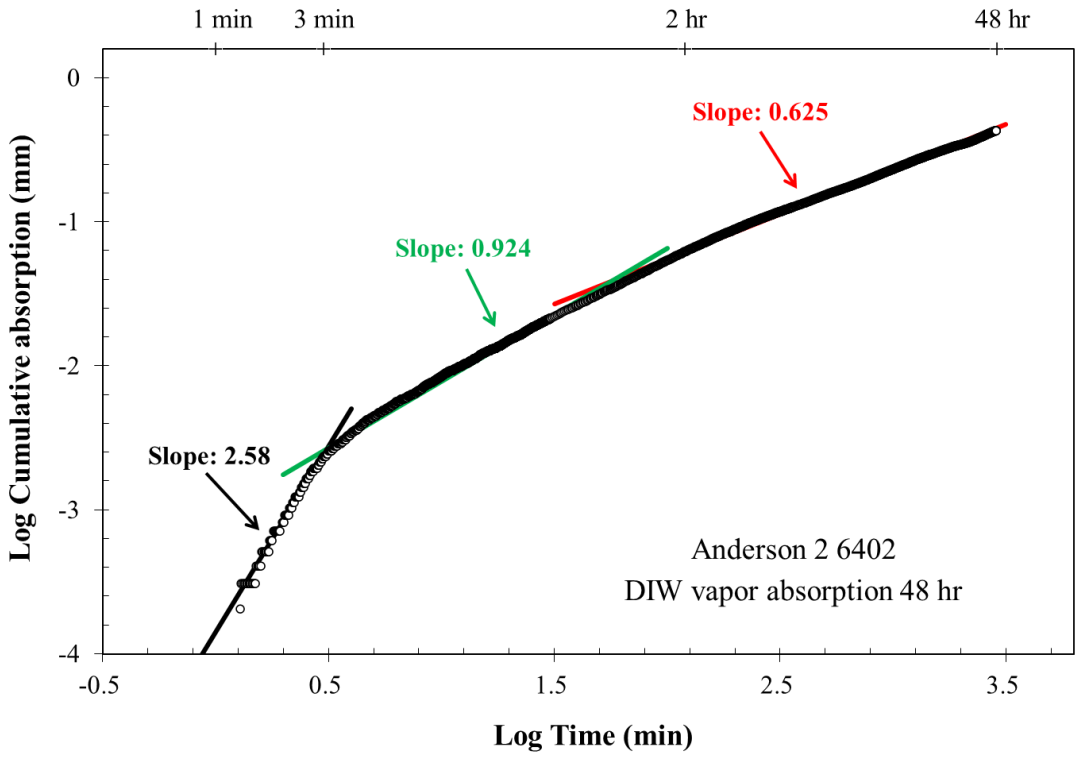

Figure 19: DIW vapor absorption slopes for Anderson 2-6335 (A), Anderson 2-6355 (B), Anderson 2-6367 (C), Anderson 2-6376 (D), Anderson 2-6385 (E), and Anderson 2-6402 (F).

A)

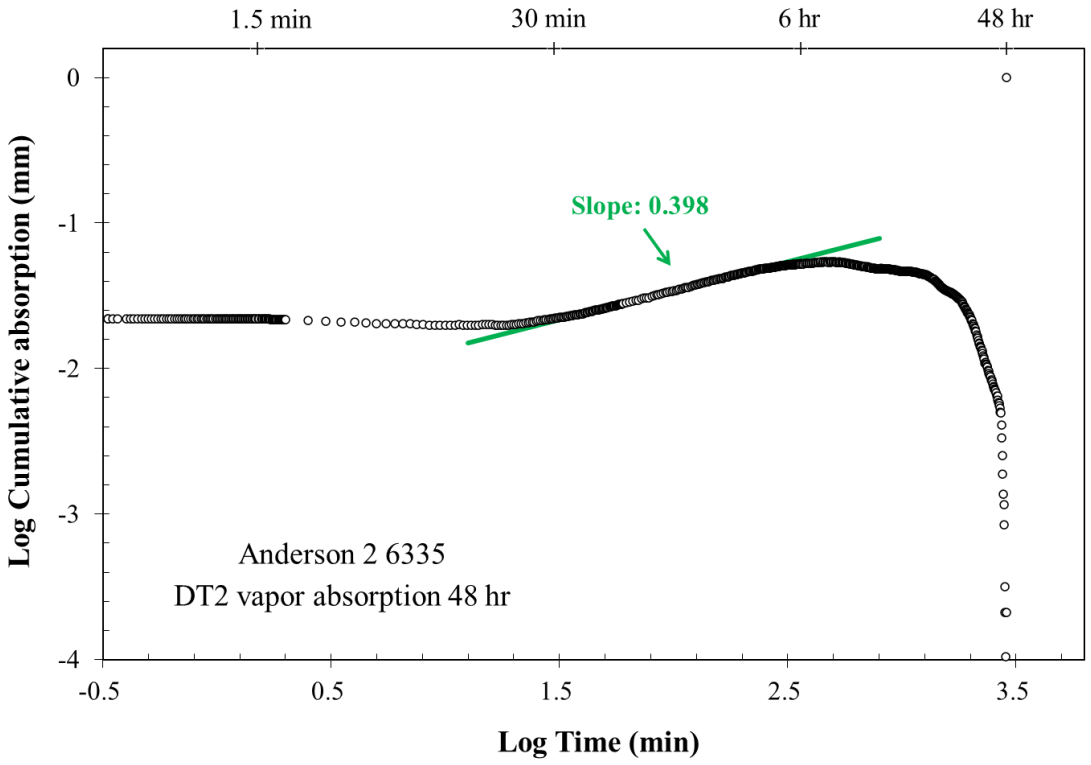
1.5 min
30 min
6 hr
48 hr
0
-1
-2
-3
-4
Log Cumulative absorption (mm)
Slope: 0.398
Anderson 2 6335
DT2 vapor absorption 48 hr
-0.5
0.5
1.5
2.5
3.5
Log Time (min)

B)

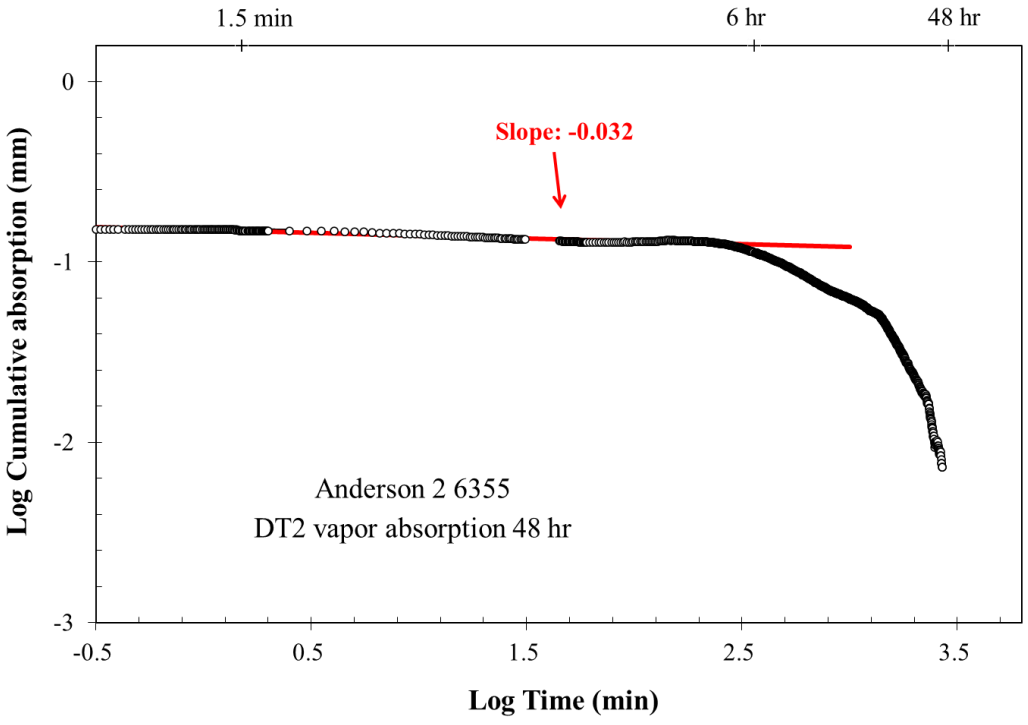
1.5 min
6 hr
48 hr
0
-1
-2
-3
Log Cumulative absorption (mm)
Slope: -0.032
Anderson 2 6355
DT2 vapor absorption 48 hr
-0.5
0.5
1.5
2.5
3.5
Log Time (min)

C)

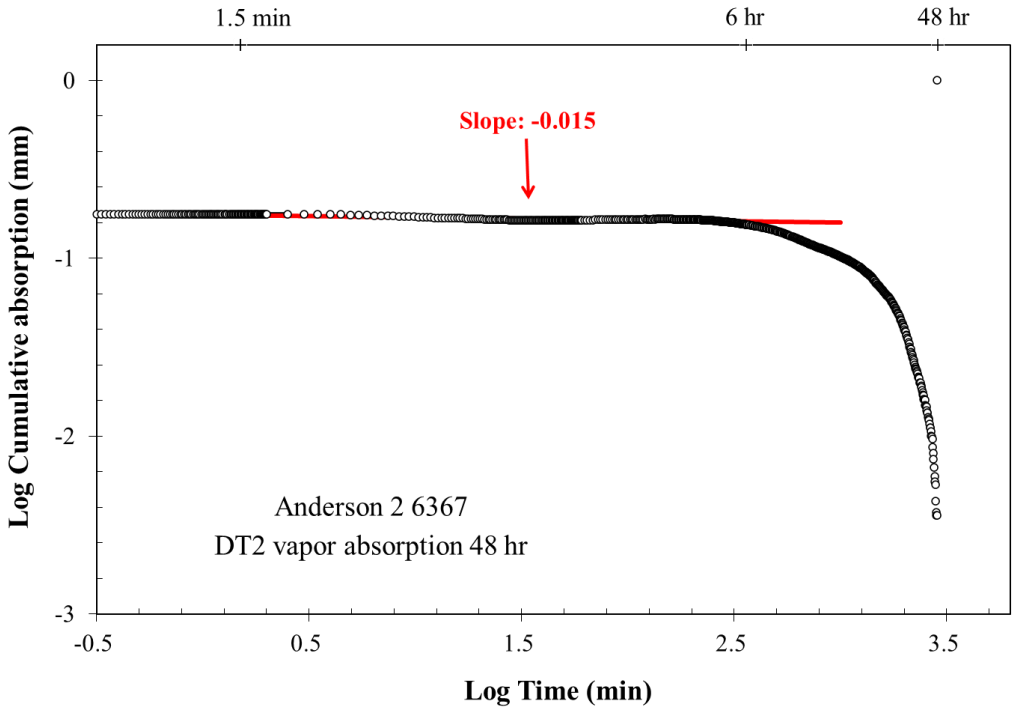
1.5 min
6 hr
48 hr
0
-1
-2
-3
Slope: -0.015
Anderson 2 6367
DT2 vapor absorption 48 hr
Log Cumulative absorption (mm)
-0.5
0.5
1.5
2.5
3.5
Log Time (min)

D)

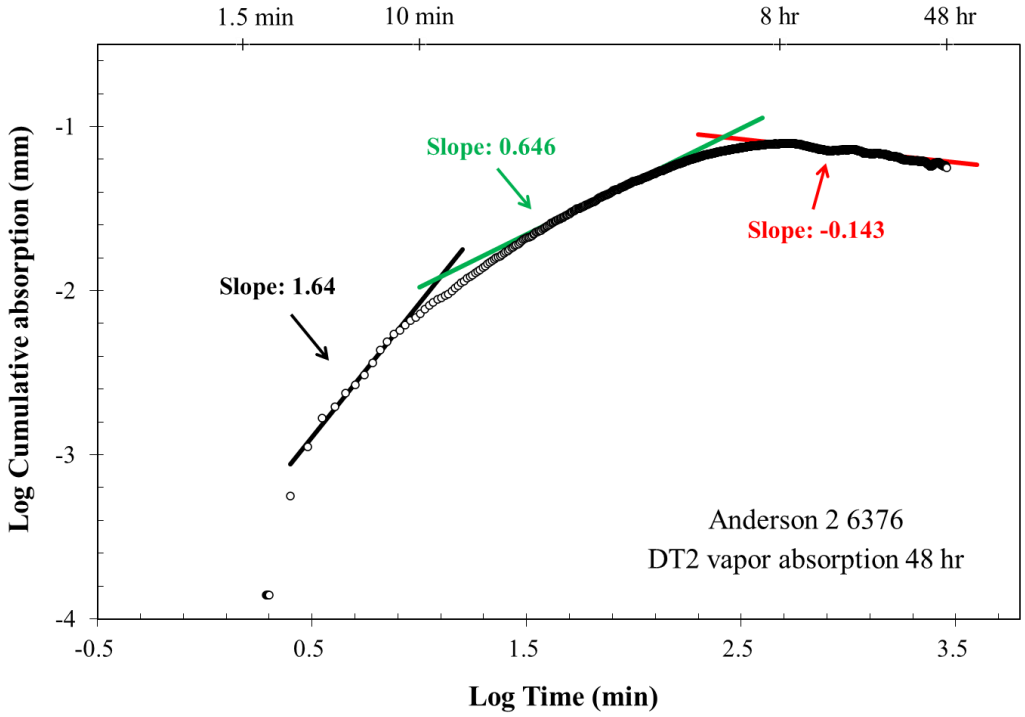
1.5 min
10 min
8 hr
48 hr
-1
-2
-3
-4
Slope: 0.646
Slope: -0.143
Slope: 1.64
Anderson 2 6376
DT2 vapor absorption 48 hr
Log Cumulative absorption (mm)
-0.5
0.5
1.5
2.5
3.5
Log Time (min)

E)

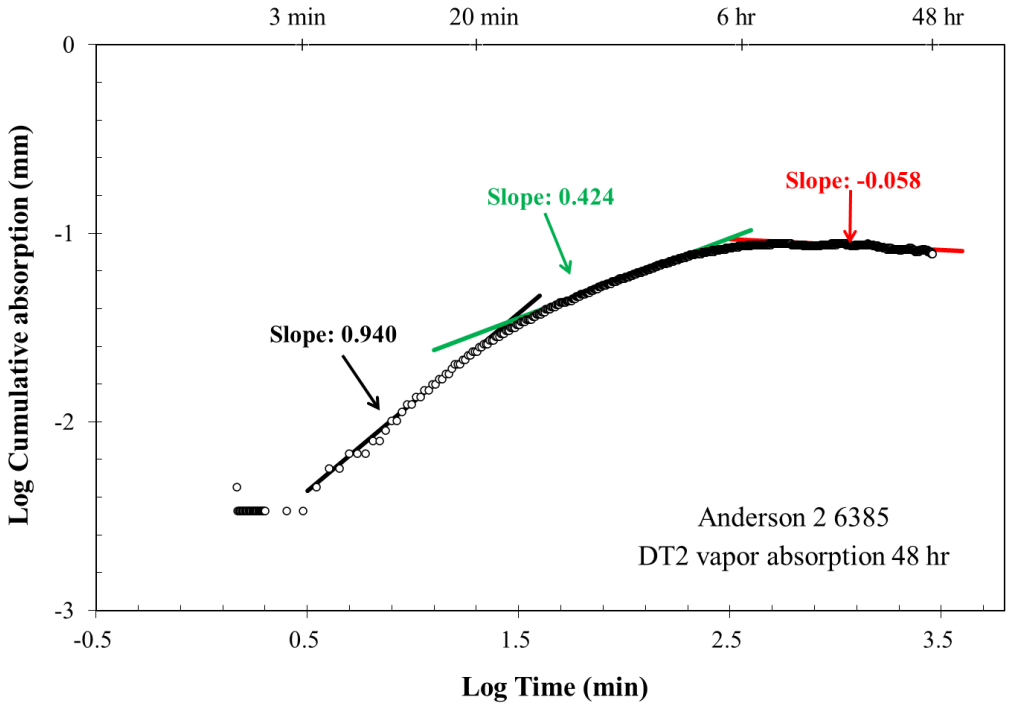

F)

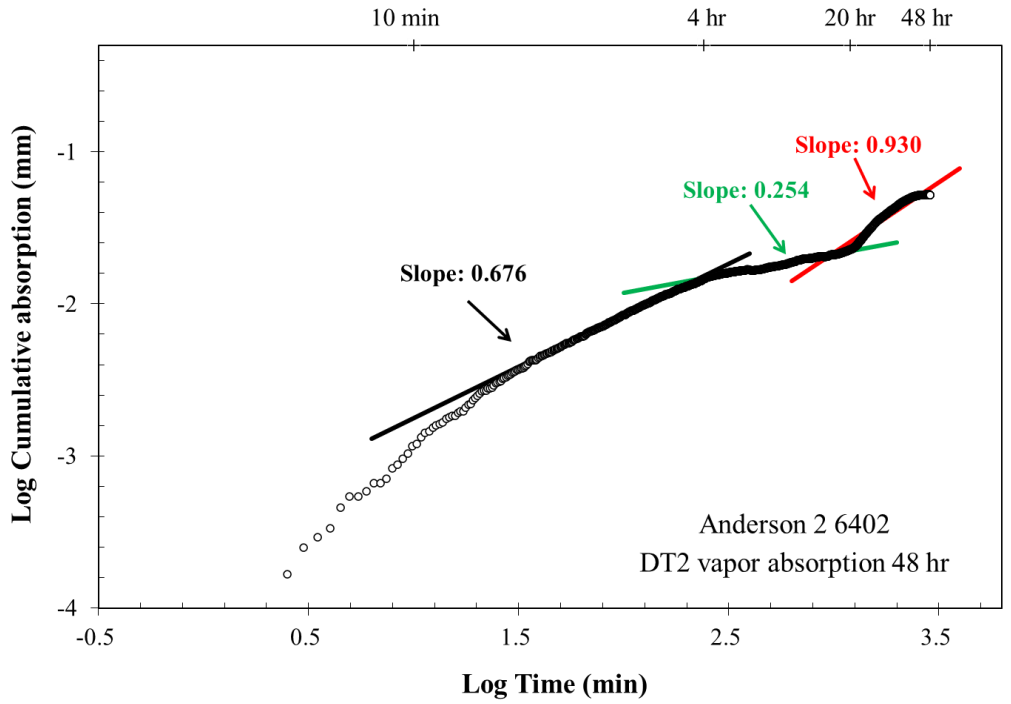

Figure 20: DT2 vapor absorption slopes for Anderson 2-6335 (A), Anderson 2-6355 (B; probably with experimental issues), Anderson 2-6367 (C; probably with experimental issues of strong evaporation and low wettability of DT2), Anderson 2-6376 (D), Anderson 2-6385 (E), and Anderson 2-6402 (F).

4.6 Liquid Pycnometry

"Apparent" bulk density calculations from liquid pycnometry are shown in Table 11. Samples Anderson 2-6355, 2-6385, 2-6402, and Anderson 1-6403 were tested using DIW and DT2 fluids. Granular sample sizes used for these samples include GRI+, A, GRI, B and C. The average apparent bulk density was calculated from three tests for each sample size. Bulk density values decrease for all samples as the sample size decreases from GRI+ to size C.

Table 11: Apparent bulk density results from liquid pycnometry.

Sample ID	Size designation	Size	Equivalent spherical diameter (µm)	Apparent bulk density (g/cm^3)	
				DIW	DT2
Anderson 1-6403	GRI+	1.70 - 2.36 mm	2030	2.779±0.177	2.799±0.033
	Size A	841 - 1700 µm	1271	2.904±0.058	2.894±0.064
	GRI	500 - 841 µm	671	2.779±0.096	2.759±0.050
	Size B	177 - 500 µm	339	2.579±0.012	2.799±0.006
	Size C	75 - 177 µm	126	2.356±0.077	2.619±0.029
Anderson 2-6355	GRI+	1.70 - 2.36 mm	2030	2.829±0.013	2.833±0.053
	Size A	841 - 1700 µm	1271	2.649±0.040	2.795±0.007
	GRI	500 - 841 µm	671	2.846±0.036	2.857±0.025
	Size B	177 - 500 µm	339	2.744±0.050	2.803±0.093
	Size C	75 - 177 µm	126	2.612±0.124	2.765±0.061
Anderson 2-6385	GRI+	1.70 - 2.36 mm	2030	2.780±0.079	2.942±0.070
	Size A	841 - 1700 µm	1271	2.759±0.120	2.864±0.052
	GRI	500 - 841 µm	671	2.817±0.052	2.838±0.084
	Size B	177 - 500 µm	339	2.864±0.025	2.939±0.144
	Size C	75 - 177 µm	126	2.795±0.088	2.712±0.094
Anderson 2-6402	GRI+	1.70 - 2.36 mm	2030	2.888±0.063	2.833±0.036
	Size A	841 - 1700 µm	1271	2.801±0.004	2.979±0.065
	GRI	500 - 841 µm	671	2.709±0.050	2.925±0.050
	Size B	177 - 500 µm	339	2.937±0.108	2.994±0.122
	Size C	75 - 177 µm	126	2.720±0.104	2.631±0.082

4.7 Particle Density

Particle density was determined for all samples using the AccuPyc II 1340, and their results for sample sizes GRI+ and A are shown in Table 12. The particle densities range from 2.828 g/cm^3 for sample Anderson 1-6403 to 2.902 g/cm^3 for sample Anderson 2-6385, consistent with the reported mineral densities of 2.8-3.1 for dolomite, 2.71 for calcite, and 2.97 g/cm^3 for anhydrite.

Table 12: Average particle density results.

Sample ID	Size designation	Size	Equivalent spherical diameter (μm)	Average particle density (g/cm^3)
Anderson 1-6403	GRI+	1.70 - 2.36 mm	2030	2.828±0.0004
	Size A	841 - 1700 μm	1271	2.836±0.006
Anderson 2-6335	GRI+	1.70 - 2.36 mm	2030	2.863±0.0004
	Size A	841 - 1700 μm	1271	2.866±0.005
Anderson 2-6355	GRI+	1.70 - 2.36 mm	2030	2.860±0.001
	Size A	841 - 1700 μm	1271	2.857±0.003
Anderson 2-6367	GRI+	1.70 - 2.36 mm	2030	2.852±0.005
	Size A	841 - 1700 μm	1271	2.851±0.003
Anderson 2-6376	GRI+	1.70 - 2.36 mm	2030	2.857±0.0007
	Size A	841 - 1700 μm	1271	2.858±0.004
Anderson 2-6385	GRI+	1.70 - 2.36 mm	2030	2.893±0.005
	Size A	841 - 1700 μm	1271	2.902±0.002
Anderson 2-6402	GRI+	1.70 - 2.36 mm	2030	2.876±0.004
	Size A	841 - 1700 μm	1271	2.864±0.003

4.8 Well Log Analysis

Petrophysical properties such as porosity, permeability, and water saturation were determined through well log analyses. These log-derived values were compared with initial core data performed on the samples by Core Laboratories as well as values from experiments performed in this thesis. Core data depths were adjusted to match log data using porosity curves. Log and core data curves for each well are displayed in 6 Tracks (Table 13). Facies depths, formation top of the upper Clear Fork, core and log data for Anderson 1 and Anderson 2 are

displayed in Figure 21 and Figure 22, respectively. The porosity in Track 2 is the average of the neutron and the density porosities.

Table 13: Well log track data.

Track 1	**Track 2**	**Track 3**	**Track 4**	**Track 5**	**Track 6**
Gamma Ray	Neutron Porosity	Deep Resistivity	Core Porosity	Water Saturation	Timur Permeability
Caliper	Density Porosity			Core Oil Saturation	Core Permeability
	Average Porosity			Core Water Saturation	Core Grain Density

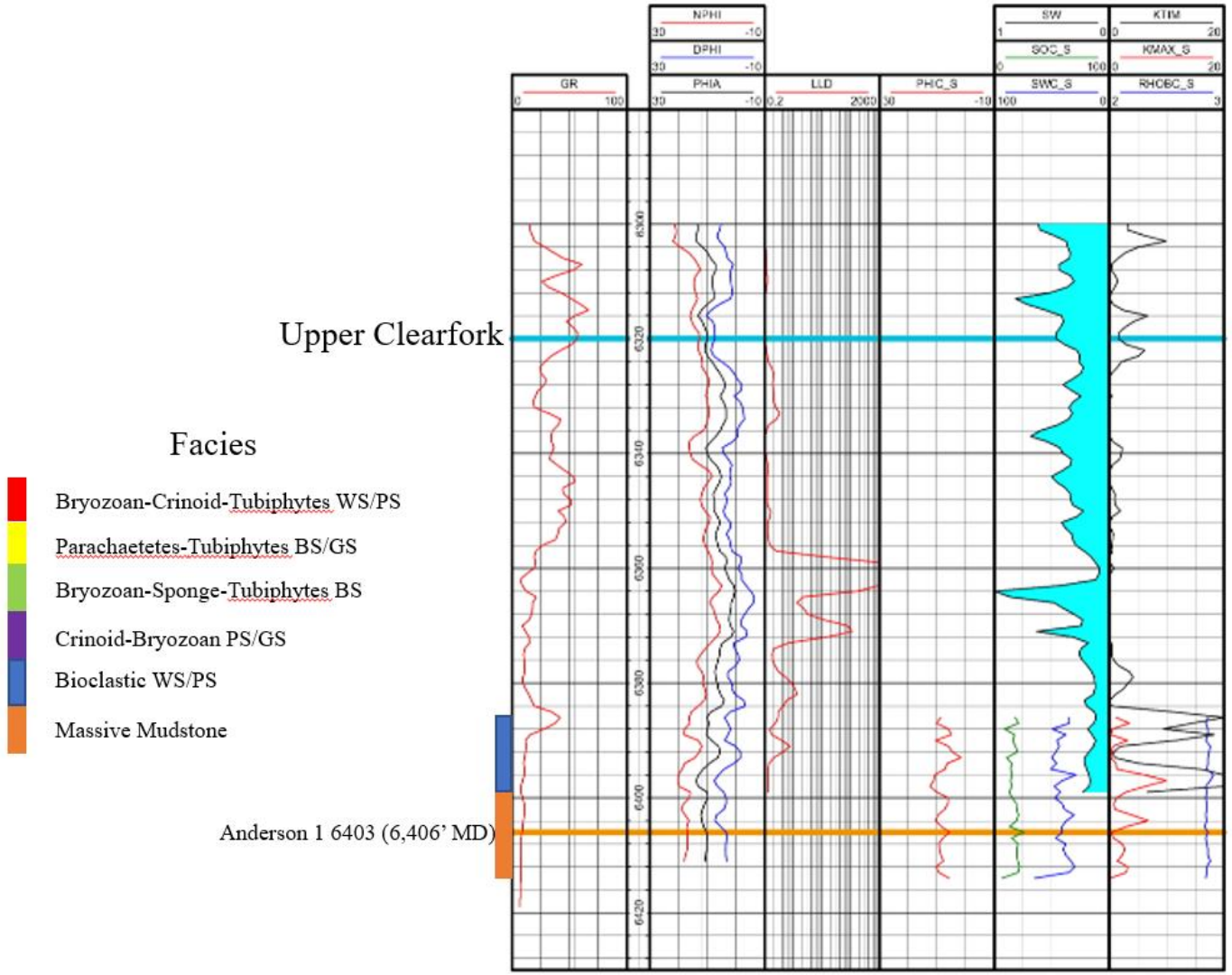

Figure 21: Anderson 1 well log and core data curves (WS: wackestone; PS: packstone; BS: Boundstone; GS: Grainstone) (core depths adjusted to match log curves).

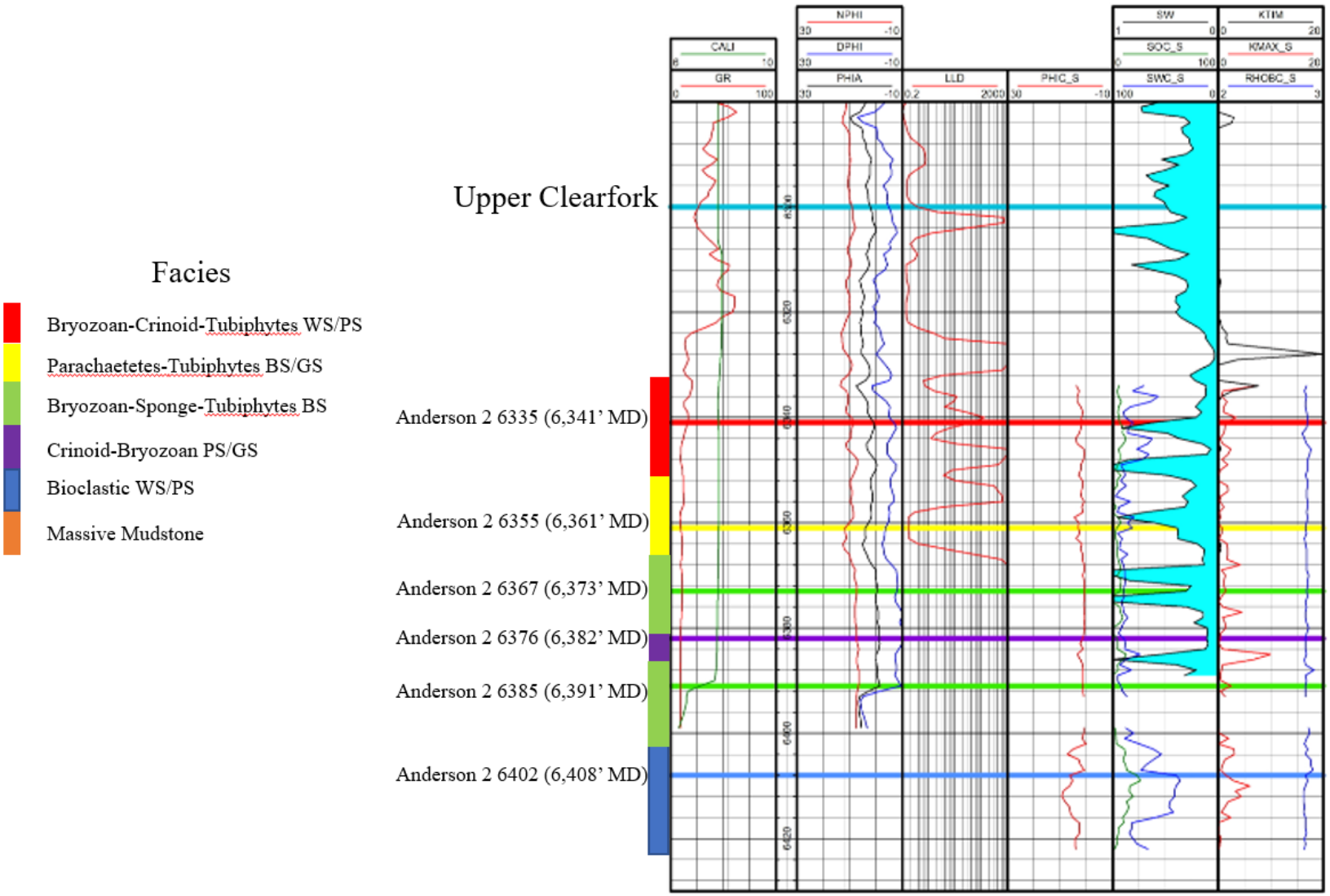

Figure 22: Anderson 2 well log and core data curves (core depths adjusted to match log curves).

Chapter 5: Discussion

5.1 Mineralogy & Porosity

XRD analyses show that all samples contain 45%+ dolomite with samples Anderson 2 6355 and Anderson 1-6403 containing 90%+ dolomite with less than 10% anhydrite. Mineral content can play a significant role in porosity values, as Mosley (1990) described anhydrite replacement in filling up pore space. Reef unit facies consisting of bryozoan-sponge-tubiphytes boundstone, bryozoan-crinoid packstone/grainstone, parachaetetes-tubiphytes boundstone/grainstone, crinoid-bryozoan-tubiphytes wackestone/packstone were most affected by replacement anhydrite to have a lowered porosity. Fore-slope unit facies consisting of bioclastic wackestone/packstone and massive carbonaceous mudstone displayed higher porosity (Mosley, 1990); however, our sample Anderson 2-6402 from the bioclastic wackestone/packstone facies exhibit a large value of 47% anhydrite and consequently less than 2% porosity. Scatter plots are created to show the correlation between mineral content and porosity with facies type indicated (Figure 23). The plot shows a trend of decreasing porosity with increasing anhydrite content.

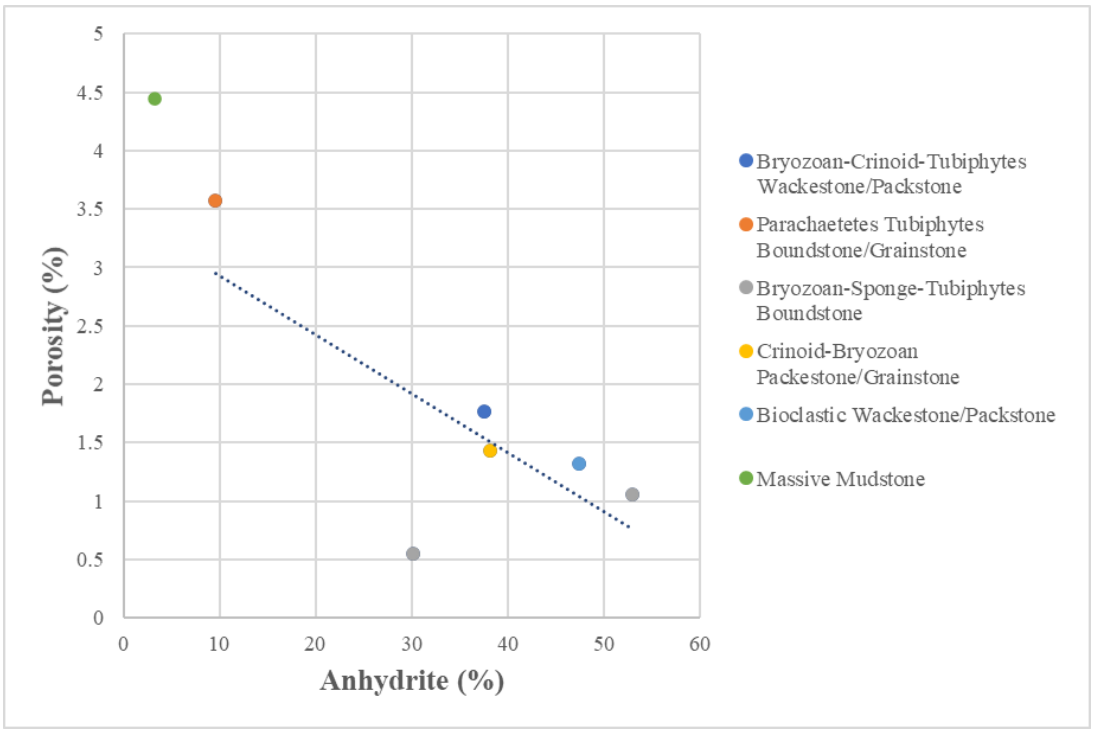

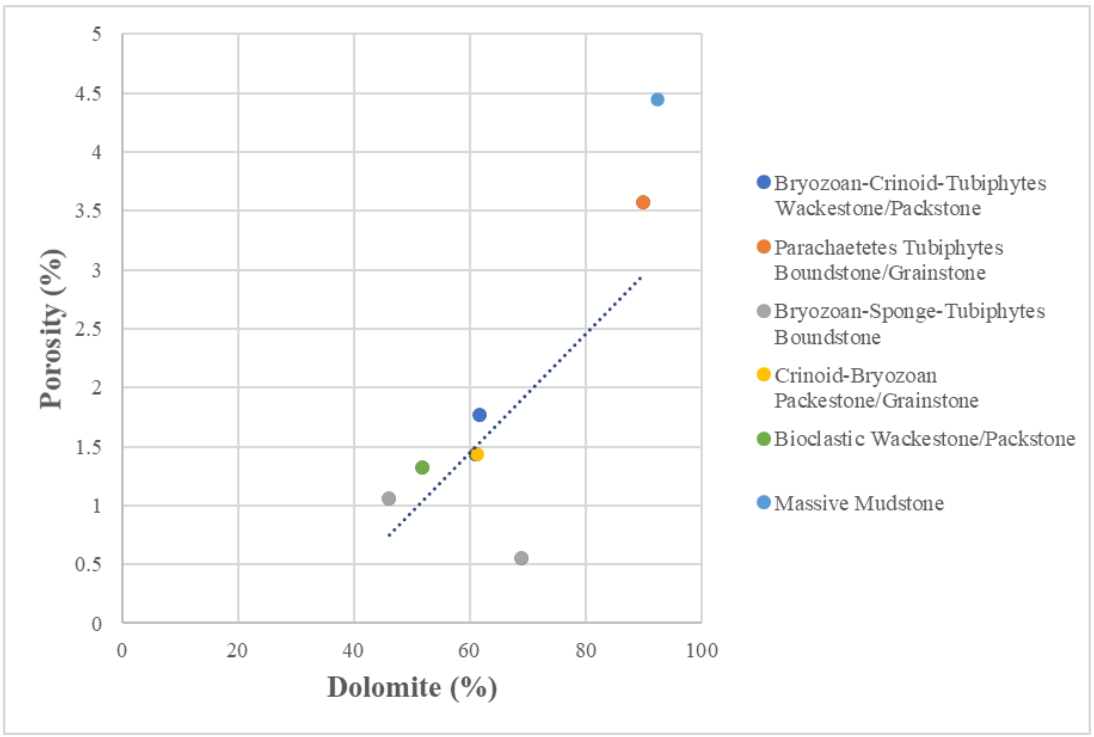

Figure 23: Porosity vs. mineral content; anhydrite (A) and dolomite (B) with trendlines and facies type indicated.

5.2 Geochemistry

Low TOC values from geochemical analyses indicate that all samples are organic-lean carbonate rocks. Sample Anderson 1-6403 exhibits the highest TOC percentage but only at a value of 0.51 wt% TOC. All samples were determined to have gas prone type III kerogen; however, this interpretation is to be taken with caution due to the organic-lean nature of the samples tested. Values of vitrinite reflectance range from 0.45-0.67% indicating most of the upper Clear Fork to be immature or just at the start of the oil generation window. The normalized oil content also agrees that the samples are early mature except for sample Anderson 2-6385 shown to be mature and the Anderson 2-6402 shown to be in oil/gas production. It is possible that these samples could have been stained or contaminated to show these results as other methods show these samples to be immature.

5.3 Porosity Results from Different Approaches

Porosity results from vacuum saturation, MICP, and log analyses are shown in Table 14. A difference of less than 2% from these three different methods show a good agreement on porosity except for the log-derived porosity for sample Anderson 1-6403. MICP and vacuum saturation results matched most closely with an absolute difference of less than 1.6%. Logs measure further from the wellbore than lab-derived sidewall core data explaining the larger variance in porosity values. Porosity values range at 0.24-3.94% from MICP analyses and 0.55-4.45% from vacuum saturation, lower than the porosity values of 4.10-6.80% determined by Griffin (2017) in the Northwest Shelf Clear Fork equivalent carbonate reservoirs of the, Paddock and Blinebry. Lower porosity values are likely due to higher anhydrite mineral content within the study intervals in this study. Negative values of log-derived porosity could be related to high anhydrite mineral content causing negative density porosity values on a limestone matrix log.

Table 14: Porosity results from vacuum saturation (cubes), MICP (cubes), and log curves (cubic feet volume).

Sample ID	Porosity (%)		
	Vacuum saturation	MICP	Log curves
Anderson 1 6403	4.45	3.94	10.13
Anderson 2 6335	1.77	0.24	0.75
Anderson 2 6355	3.57	2.43	4.05
Anderson 2 6367	0.55	0.24	-0.46
Anderson 2 6376	1.43	1.3	-1.30
Anderson 2 6385	1.06	0.73	-1.53
Anderson 2 6402	1.32	0.95	-

5.4 Permeability

Log-derived permeability was determined from the Timur equation with the use of porosity and resistivity log curves. A good match between log derived permeability and core permeability is made difficult due to the resistivity log only covering intervals of two of the samples tested through MICP. Permeability values determined from the dominant pore-throat size (>100 nm) were used to compare with log derived permeability in Table 15. Permeability values from MICP analyses range from 1.95-172*10^{-3} mD, except for Anderson 2-6335 which will re-run for MICP (as discussed above in MICP section); in addition, porosity-permeability under stressed conditions will be performed for this and other samples. Permeability results show a low ability for fluid flow through the pore networks on the samples tested. Anhydrite content did not appear to effect permeability of the samples tested.

Table 15: Permeability values from MICP and log curves.

Sample ID	Permeability (mD)		
	MICP	Core Labs	Log Derived Permeability
Anderson 1-6403	1.50E-02	4.00E-01	-
Anderson 2-6335	5.44E+00	1.40E+00	1.00E-05
Anderson 2-6355	1.95E-03	7.60E-01	4.31E-02
Anderson 2-6367	1.72E-01	1.50E+00	-
Anderson 2-6376	2.35E-02	4.10E-01	-
Anderson 2-6385	1.31E-01	2.50E+00	-
Anderson 2-6402	4.85E-02	1.50E+00	-

5.5 Pore Connectivity

From fluid imbibition, Anderson 2-6335, 2-6367, 2-6376, and 2-6402 display low pore connectivity while Anderson 2-6355, 2-6385, and Anderson 1-6403 show an intermediate pore connectivity with DIW. From vapor absorption, all samples displayed high pore connectivity with DIW and samples Anderson 2-6335 and 2-6385 exhibit an intermediate pore connectivity, Anderson 2-6335 reveals low pore connectivity, and Anderson 2-6376 indicates high pore connectivity with DT2. Higher connectivity slopes for vapor absorption is related to capillary condensation in multiple dimensions whereas imbibition tests are limited to the imbibing front. Pore connectivity slope vs. mineral content are displayed in Figures 24-25, which show no apparent trend with the samples tested.

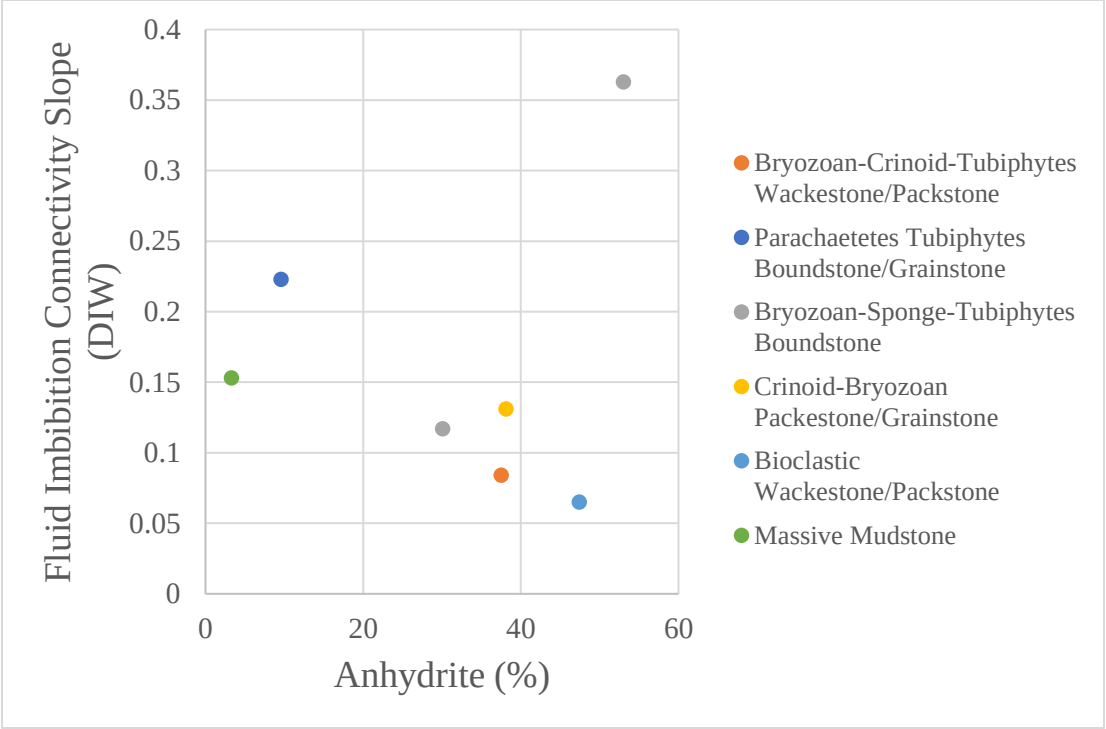

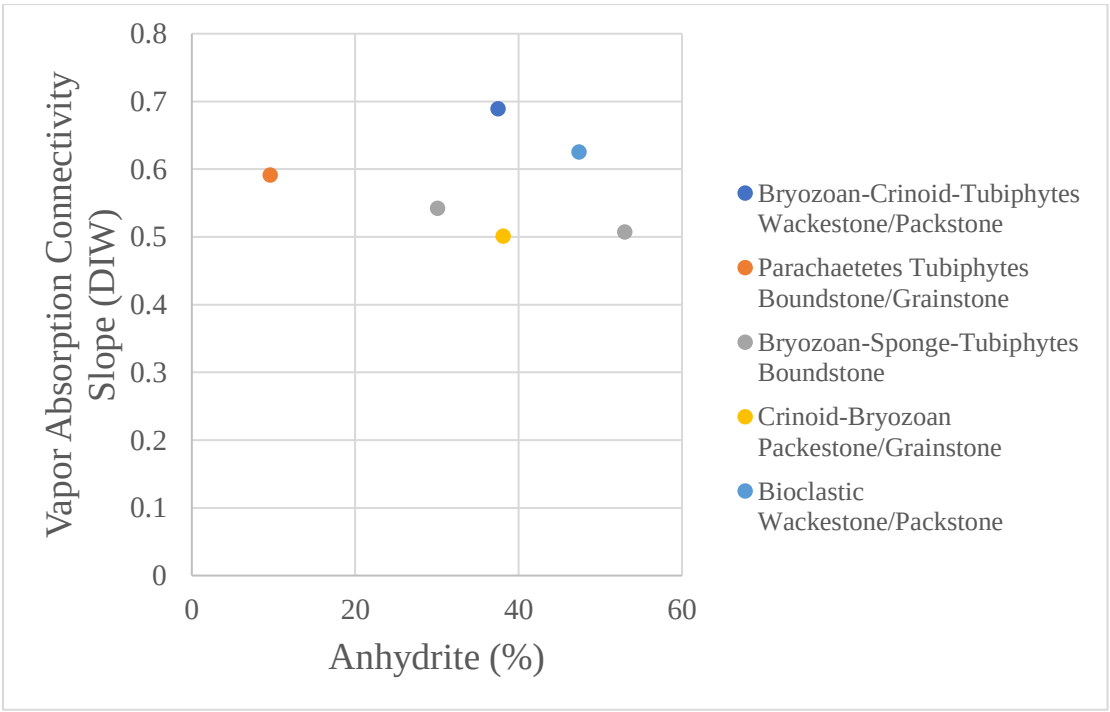

Figure 24: Anhydrite mineral content vs. connectivity slopes from fluid imbibition (top) and vapor absorption using DIW (bottom).

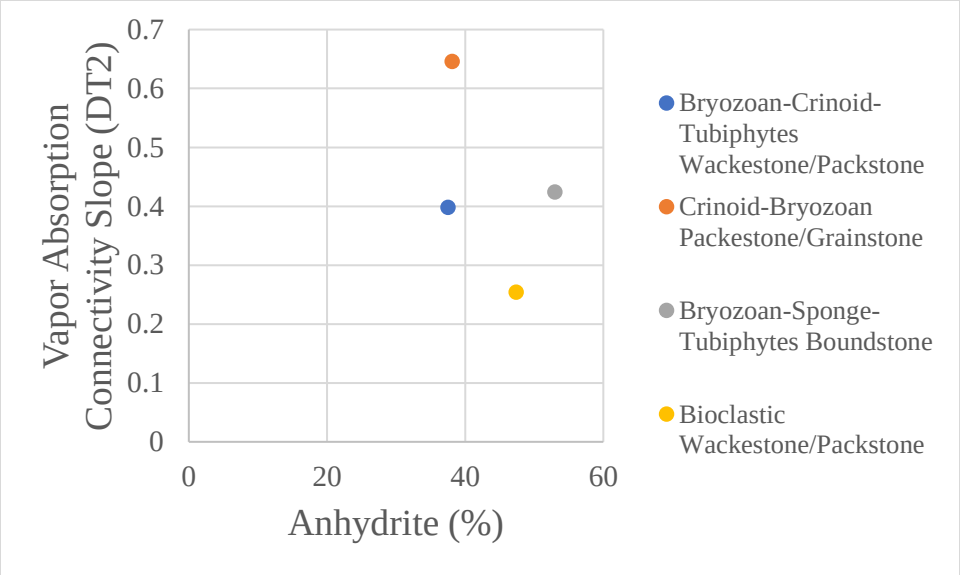

Figure 25: Anhydrite mineral content vs. connectivity slope from vapor absorption using DT2.

5.6 Density

Density values were determined from MICP analyses and vacuum saturation with DIW. Bulk and particle density values for cubic samples are displayed in Table 16. All density results from MICP analyses are higher than vacuum saturation results with differences up to 0.249 g/cm^3. MICP particle densities more closely match core particle density and particle density determined using the AccuPyc II 1340 with values in the 2.83-2.85 g/cm^3 range. Mineral content vs. the bulk and particle density from MICP analysis are displayed in Figure 26 and Figure 27, respectively. The figures indicate a decrease in bulk and particle density with a decrease in anhydrite mineral content. This is expected as anhydrite has a larger density of 2.97 g/cm^3 compared to dolomite which has a density 2.84 g/cm^3. This trend is less clear with particle density likely due to the relationship of particle and bulk density to porosity, displaying larger differences in more porous samples.

Table 16: Bulk density and particle density results from MICP (cube) and vacuum saturation (cube).

Sample ID	Bulk density (g/cm^3)		Particle density (g/cm3)	
	Vacuum saturation	MICP	Vacuum saturation	MICP
Anderson 1 6403	2.525	2.689	2.643	2.800
Anderson 2 6335	2.596	2.845	2.644	2.852
Anderson 2 6355	2.570	2.771	2.665	2.851
Anderson 2 6367	2.588	2.833	2.603	2.840
Anderson 2 6376	2.613	2.812	2.651	2.850
Anderson 2 6385	2.697	2.830	2.726	2.851
Anderson 2 6402	2.652	2.864	2.688	2.891

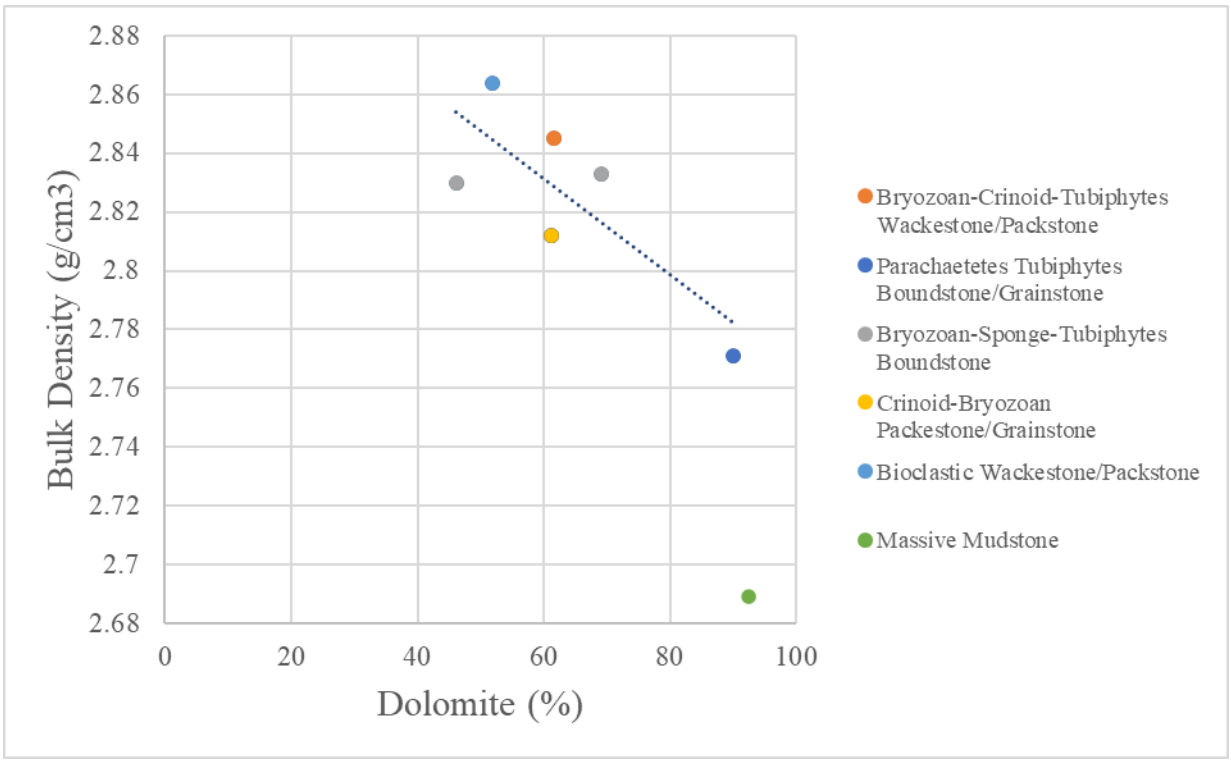

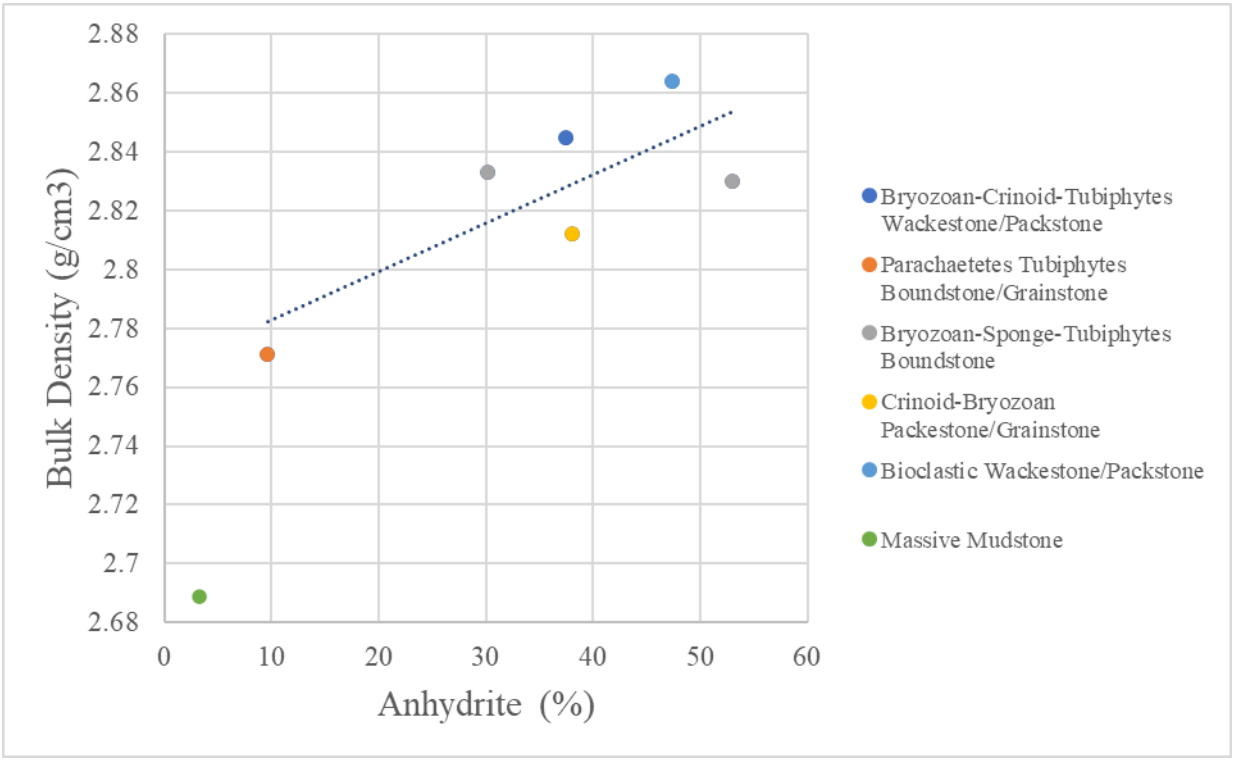

Figure 26: Bulk density vs. mineral content: dolomite (top) and anhydrite (bottom).

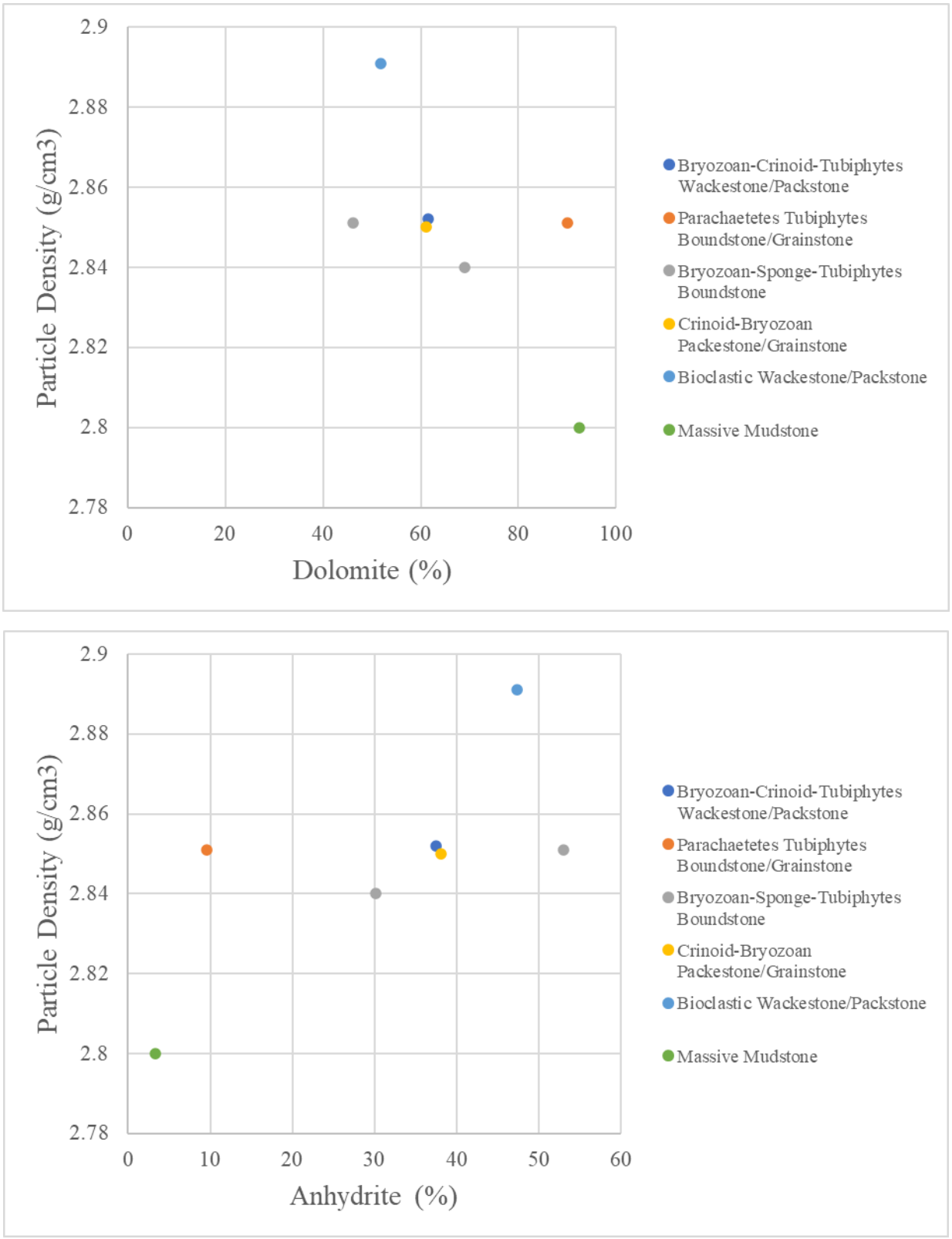

Figure 27: Particle density vs. mineral content: dolomite (top) and anhydrite (bottom).

Chapter 6 Conclusions and Recommendations

6.1 Conclusions

Samples from a variety of facies were chosen within the upper Clear Fork in the Northern Shelf to study the mineralogy and facies effect on petrophysical properties such as porosity, permeability, and imbibition-absorption behavior. Results on seven samples from the Palm Sunday field were compared from various experiments, including XRD, pyrolysis, core analyses, vacuum saturation, MICP, liquid pycnometry, fluid imbibition and vapor absorption. The results from these experiments are described below:

- All samples are predominately composed of dolomite and anhydrite with only a minor amount of quartz.
- All samples are determined to be organic-lean with low TOC and on the borderline of immature and oil generation.
- Higher porosity values are found in samples with lower anhydrite mineral content; Higher porosity values are found in the fore-slope unit facies; massive carbonaceous mudstone and bioclastic wackestone/packestone facies.
- Anhydrite lowered porosity within the reef unit. Replacement anhydrite is reported to fill in pore spaces in the reef unit facies: bryozoan-sponge-tubiphytes boundstone, bryozoan-crinoid packstone/grainstone, parachaetetes-tubiphytes boundstone/grainstone, crinoid-bryozoan-tubiphytes wackestone/packstone.
- Porosity values increase as sample sizes are decreased, indicating a low pore connectivity of upper Clear Fork formation, which is also indicated from fluid imbibition tests.
- All samples exhibit intergranular pores to be the dominant pore type with all pore-throats >10 nm.

- Permeability values range from 76.9-172 nD in the dominant pore-throat region for each sample at >100nm.
- Log-derived porosity from the average of the neutron and density porosity curves match well with porosity derived from MICP and vacuum-saturation tests.
- Though only based on limited samples, Timur's equation for permeability generally matches well with permeability from core data and MICP permeability results.
- Log-derived water saturation underestimates water saturation values from core data.
- MICP density measurements of 1 cm-sized cubes match well with the core density data of 2.54 cm diameter plugs. Vacuum saturation density measurements do not match as well with either method. MICP results for bulk density values range from 2.689-2.864 g/cm^3 and particle density values vary from 2.800-2.891 g/cm^3. A relation of increasing density with increasing anhydrite in the samples is present.

6.2 Recommendations

The Clear Fork Formation has one of the lowest recovery efficiencies among the carbonate reservoirs in the Permian Basin. In order to improve the recovery efficiency, further understanding of the petrophysical properties and mineralogy by facies type as well as facies variability is necessary. Further characterization of the pore types could be achieved with scanning electron microscopy imaging. Independent analyses of bulk and particle densities for a range of granular-sized samples for effective porosity as a function of sample size will help to tease out the pore connectivity of these rocks. More samples from the upper Clear Fork interval would improve the understanding of the petrophysical properties associated with each facies type. Further analyses of the upper Clear Fork could lead to improving recovery efficiencies as more wells are drilled.

References

Archie, G. E. 1942. The electrical resistivity log as an aid in determining some reservoir characteristics. Journal of Petroleum Technologies. 5: 54-62.

Core Laboratories. 1972. A Survey of the Subsurface Saline Water of Texas. Texas Water Development Board v. 2, p. 162. https://www.twdb.texas.gov/publications/reports/numbered_reports/doc/R157/R157V2.pdf

Dorobek, S. L. 1995. Synorogenic carbonate platforms and reefs in foreland basins: controls on stratigraphic evolution and platform/reef morphology. Stratigraphic Evolution of Foreland Basins: SEPM Special Publication 52.

Doveton, J. H. 1999. Basics of Oil and Gas Log Analysis. Kansas Geological Survey, p. 24.

Gao, Z., & Hu, Q. 2013. Estimating permeability using median pore-throat radius obtained from mercury intrusion porosimetry. Journal of Geophysics and Engineering. 10, 025014. DOI:10.1088/1742-2132/10/2/025014.

Griffin, M. 2017. Petrophysical Properties of the Yeso, Abo, and Cisco Formations in the Permian Basin in New Mexico, U.S.A. M.S. Thesis, the University of Texas at Arlington, USA.

Hager, J. 1998. Steam drying of porous media. Ph.D. Thesis, Department of Chemical Engineering, Lund University, Sweden.

Holtz, M. H., and C. M. Garrett 1990. Geologic and engineering characterization of Leonardian carbonate oil reservoirs: A framework for strategic recovery practices in four oil plays. *in* Permian Basin oil and gas fields Innovative ideas in exploration and development, West Texas Geological Society Publication, 90-87.

Hu, Q. H., Ewing, R. P., and Dultz, S. 2012. Pore connectivity in natural rock. Journal of Contaminant Hydrology. 133: 76-83.

Hu, Q. H., Persoff, R. P., and Rowe, H. D. 2015. Low nanopore connectivity limits gas production in the Barnett Formation. Journal of Geophysical Research: Solid Earth. 120(12): 8073-8087.

Hu, Q. H., Persoff, R. P., Wang, J.S.Y. 2001. Laboratory measurement of water imbibition into low-permeability welded tuff. Journal of Hydrology. 242(1-2): 64-78.

Hu, Q. H., Zhang, Y. X., Meng, X. H., Li, Z., Xie, Z. H., Li, M. W. 2017. Characterization of multiple micro-nano pore networks in shale oil reservoirs of Paleogene Shahejie Formation in Dongying Sag of Bohai Bay Basin, East China. Petroleum Exploration and Development. 44(5): 720-730.

Jeary, G. L. 1978. Leonardian Strata in Northern Midland Basin of West Texas, *in* Energy quest for the southwest: West Texas Geological Society, Southwest Section of American Association of Petroleum Geologists, Transactions Annual Meeting, Midland, Texas, 30-47.

Katz, A., and Thompson, A. 1987. Prediction of rock electrical conductivity from mercury injection measurements. Journal of Geophysical Research: Solid Earth, v. 92, p. 599-607.

Lucia, F. J. 1969. Recognition of evaporite-carbonate shoreline sedimentation. AAPG Bulletin 53.3: 729-730.

Mazzullo, S. J. 1982. Stratigraphy and depositional mosaics of lower Clear Fork and Wichita Groups (Permian), northern Midland basin, Texas. AAPG Bulletin 66.2: 210-227.

McGillis, K. A., and Presley, M. W. 1981. Tansill, Salado, and Alibates Formations: upper Permian evaporite/carbonate strata of the Texas Panhandle. Vol. 81. No. 8. Bureau of Economic Geology, University of Texas at Austin.

Micromeritics Instrument Corporation. 2020. AccuPyc II 1340 Pycnometer Fully Automatic Density Analyzer.

Mosley, B. R. 1990. Deposition and Diagenesis of the Upper Clear Fork (Leonardian) Shelf Margin, Palm Sunday Field, Hockley County, Texas. M.S. Thesis, The University of Texas at Arlington, USA.

Oriel, S. S., Myers, D. A., and Crosby, E. J. 1967. West Texas Permian basin region. Paleotectonic Investigations of the Permian System in the United States: U.S. Geological Survey Professional Paper 515, 21-60.

Robinson, K. 1988. Petroleum geology and hydrocarbon plays of the Permian Basin petroleum province West Texas and southeast New Mexico. No. 88-450-Z. US Geological Survey Open-File Report 88-450-Z, 53 pp. https://doi.org/10.3133/ofr88450Z.

Ruppel, S. C., and Harrington, R. R. 2012. Facies and sequence stratigraphy: Critical tools for reservoir framework definition, Fullerton Clear Fork reservoir, Texas. *AAPG Bulletin*: 5-48.

Silver, B. A., and Todd, R. G. 1969. Permian cyclic strata, northern Midland and Delaware basins, west Texas and southeastern New Mexico. AAPG Bulletin 53.11: 2223-2251.

Tang, C. M. 2015. Permian Basin. *Encyclopædia Britannica*, Encyclopædia Britannica, Inc., www.britannica.com/place/Permian-Basin. Accessed 1 April 2020.

Timur, A. 1968. An investigation of permeability, porosity, and residual water saturation relationships for sandstone reservoirs. The log Analyst, 9: 8-17.

Tyler, N., and Banta, N. J. 1989. Oil and gas resources remaining in the Permian Basin: targets for additional hydrocarbon recovery: The University of Texas at Austin. Bureau of Economic Geology Geological Circular 89.4: 20.

Wang, S., Javadpour, F., and Feng, Q. H. 2016. Confinement correction to mercury intrusion capillary pressure of shale nanopores. Scientific Reports, 6: 20160, doi:10.1038/srep20160.

Washburn, E. W. 1921. Note on a method of determining the distribution of pore size in a porous material. Physics, 7: 115-116.

Webb, A. 2001. An introduction to the physical characterization of materials by mercury intrusion porosimetry with emphasis in reduction and presentation of experimental data. Micromeritics Instrument Corporation.

Yang, K-M., and Dorobek, S. L. 1995. The Permian Basin of west Texas and New Mexico: Tectonic history of a “composite” foreland basin and its effects on stratigraphic development." Stratigraphic Evolution of Foreland Basins: SEPM Special Publication 52: 149-174.

Yang, R., Hao, F., He, C. C., Guo, X. S., Ye, J. Z., He, H. Y., Zhang, S. W., and Hu, Q. H. 2017. Experimental investigations on the geometry and connectivity of pore spaces in organic-rich Wufeng and Longmaxi shales. Marine and Petroleum Geology, 84: 225-242.

Appendix A

Laboratory Methods for XRD Analysis at the Shimadzu Center, The University of Texas at Arlington

MaximaX XRD-7000: Shimadzu X-Ray Diffractometer

Sample Preparation

- Prepare your sample by compacting the sample into the sample holder using a glass slide.
- Avoid vertical loading by removing excess sample with the edge of the glass slide.
- Attempt to make your sample as flat and homogenous as possible; once this is completed your sample is ready to be analyzed.

Powder Operations

- Turn the chiller on by pressing the power button (on the face of the chiller), a green light will illuminate.
    - Allow the chiller to sit for ~20 minutes to adjust to the proper temperature.
- Turn the XRD on by pressing the power button on the left hand side. The green power button will illuminate on the front panel of the XRD.

XRD calibration:

- Locate and open the [PCXRD] program on the desktop. The main "XRD-6100/7000" panel will display.
- Click the [Display and Setup] icon, a "door alarm check" window will pop up. Follow the prompt to open and close the XRD door, once complete click "Close". An "IOcon" window will pop up with the message "Now Calibration! If ready OK", Click "OK".
- The XRD is officially calibrated and ready to process your sample.

Setting Analysis Conditions:

- To set the processing conditions go to the "XRD 6100/7000" panel.
- Click on the [Right Gonio Condition] icon to open the [Analysis Condition Edit Program] window.
- Click the blue bar under [Measurement Mode: Standard] to open the [Standard Condition Edit] window.
- Most of the settings in the [Standard Condition Edit] window will be preset. Only a few conditions will need to be changed.
- The following general condition settings will work for a wide array of materials.

It's very important to follow these next steps, double check any settings you change ensuring to follow these guidelines precisely, This will minimize minor mistakes when processing materials and will prevent damage to the detector.

- Scanning condition: Scan Range (deg) = 2°-70° □ Optional Condition: Check the box [Option Enable]
- Beta Attachment: Control Mode: Rotation
  Rotation Speed (rpm): 6
- Slit Condition: Slit Conditions are preset and must be verified on the XRD to ensure the proper slit sizes match the setting listed under the Slit Conditions.
  - Checking the Slits:
    - Open the XRD door, on the left side of the XRD is the X-ray tube, the Divergence Slit is attached to the left side of the divergence soller slits.
    - On the right hand side will be the detector arm which contains a set of Scattering soller slits, the Scattering Slit faces the sample (Left) and the Receiving Slit faces the detector (Right).
    - If they are not the same sizes as what is preset in the [Slit Condition] box change the slit's so the do match.
  - Standard Slit Settings:
    - Divergence Slit: 1.0°
    - Scattering Slit: 1.0°
    - Receiving Slit: 0.3 mm

- Double check your settings and make sure they are correct, if they are click [OK].
- A [File & Sample Condition Edit] window will display; change the [Group name] to match your destination folder name and change [File name] and [Sample Name] to match your sample name, click [New].
  - Later samples can be created by simply changing the file and sample names and clicking [Modify].
- Click [Close] on the [Standard Condition Edit] window.

Starting the XRD Processing:

- Locate and click the [Right Giono Analysis] icon on the [XRD-6100/7000] panel.
- Your current sample name should appear highlighted blue in the upper portion of the [Right Gonio System: Analysis Condition Edit Program] window. Highlight your sample and click [Append], this adds your sample to the list in the bottom portion of the window labeled [Entry for Analysis], click [Start]. Your sample should appear in the bottom of the [Right Giono Analysis & Spooler Program] window, click [Start] in this window. This officially starts the analysis process.
  - Indicators for Analysis: A clicking sound will come from the XRD when the locking mechanism on the sliding door locks. On the face of the XRD a yellow light should illuminate under [X-RAYS ON].

- Leave all software windows open and allow the XRD to process your sample, this should take ~30 minutes.

Completed XRD Processing:

- A complete peak spectrum should appear in the [Right Giono Analysis & Spooler Program] window upon completion.
- The green [Analyzing!] Box should disappear and the yellow [X-RAYS ON] light should turn off.
- If you have more samples to analyze, continue to run your samples in the same manner listed above.

Opening Peak Profile Spectrum:

- Locate and open the icon for the [MDI jade 9] software on the Desktop.
- Under [File], click [Read], locate the folder [xddat] under [favorites]. Locate the folder where your samples are saved.
- In your folder, each sample should have a [.RAW] file, use this file to open your selected spectrum in the [Jade 9] software.

Identifying Minerals in Peak Spectrum:

It's important to have the educated background on the sample you're analyzing. Knowledge regarding the bulk composition and what you're searching for will greatly reduce the amount of time spent IDing the various peaks in the spectrum

- Locate the [Find Peaks] icon on the main tool bar next to the [Floppy Disk/Save] icon, this will identify and mark any statistically significant peaks within the spectrum.
- Choose a mineral database: At the top of the panel to the right of the spectrum window, there will be a drop-down menu choose the [RDB-Minerals] as the database. The RDB-Mineral database should be predominately used to identify most minerals in your spectra.
    - If you cannot find a mineral in the RDB-Minerals database change to the [PDF+4 Minerals] database library but be sure to change back to the RDB database once the mineral is located.
- Begin searching for minerals based on your pre-existing knowledge regarding the sample. When you identify minerals that fit your peak spectrum hit [Enter] on the keyboard, this process will add the minerals to ta compiled list of those minerals which you identified in the spectrum.
- Once you have exhausted your initial hypothetical list of minerals, a helpful tool to use is the [Line Based Search/Match]. Go to the main tool bar and locate [Identify] and select the [Line Based Search] option.

- This tool will compile a list of minerals by searching a selected PDF database for entries with peaks which are statistical matches for the peaks identified within your spectrum.
- Settings:
  - [Two-Theta Error Window] max setting should be no more than 0.24%
  - [Top Hits to List] max setting 80
- Set the parameters and click the blue [Play] icon next to the [X] to run the search and generate a list of possible phases that might fit your spectra. *Note: the line based search should not be used as a primary way to identify the bulk mineral mode of the sample as the software is not consistent when generating phases and will possibly leave out important phases for the spectrum*.

Model Analysis:

- Once all minerals have been ID'd, check that they have been added to the mineral list by pushing [Enter] on the keyboard.
- Click the [%] icon next to the drop-down mineral list located on the toolbar in the middle of the window to begin modal analysis.
  - An overlay will appear with different chart configurations of the modal results, to change the configurations of the chart use the drop-down menu in the chart window.
- To view the modal analysis in text format: locate and click the […] icon near the [%] icon. This will list the minerals by name, chemical formula, and the normalized weight percent for each mineral. It will also state if the mineral is [major], [minor], [trace], or [absent] component in the sample.
- If you would like to remove a mineral from your mineral list at any time, highlight the mineral and press [Delete] on the keyboard. [Absent] phases should be removed from the list by this method.

Analysis Check with Pattern Deconvolution:

- A key that the peak spectrum has been fully fitted and identified is by using the [Pattern Deconvolution] tool which automatically runs with the modal analysis.
  - The pattern deconvolution tool will generate a red overlay spectrum on top of the original white spectrum.
  - This process is generating a [Best Fit Profile] composed of the selected mineral standards from the [Mineral PDF database library] with your sample spectrum.
  - If all minerals have been properly identified, then the red deconvolution overlay will match the peak spectra for each peak. If there are peaks that don't have the red deconvolution overlay, then those peaks have not been identified.
- Continue processing your spectrum until your original spectra and the deconvolution spectra match.

Saving Data:

To save your data,

- Go to [file] and [Save], save your data under [Current work as *.SAV]. This will save all analysis as a separate file.

Appendix B

Laboratory Methods for Total Organic Carbon and Pyrolysis Analysis at GeoMark Research

1. Sample Requirements for a Typical Geochemical Program

For geochemical analysis, a teaspoon (ca. 10 g.) of sample material is needed when TOC, RockEval, vitrinite reflectance and residual hydrocarbon fluid fingerprinting is to be completed. If possible, a tablespoon is preferred. However, it is possible to complete a detailed program with even less sample, although there is dependency on the sample characteristics (e.g., organic richness, abundance of vitrinite, amount of staining). Sample prep includes grinding the sample with mortar and pestle until it passes through a 60-mesh sieve.

2. Total Organic Carbon (TOC) – LECO C230 instrument

Leco TOC analysis requires decarbonation of the rock sample by treatment with hydrochloric acid (HCl). This is done by treating the samples with Concentrated HCl for at least two hours. The samples are then rinsed with water and flushed through a filtration apparatus to remove the acid. The filter is then removed, placed into a LECO crucible and dried in a low temperature oven (110 C) for a minimum of 4 hours. Samples may also be weighed after this process in order to obtain carbonate% based on weight loss.

The LECO C230 instrument is calibrated with standards having known carbon contents. This is completed by combustion of these standards by heating to 1200°C in the presence of oxygen. Both carbon monoxide and carbon dioxide are generated, and the carbon monoxide is converted to carbon dioxide by a catalyst. The carbon dioxide is measured by an IR cell. Combustion of unknowns is then completed and the response of unknowns per mass unit is compared to that of the calibration standard, thereby the TOC is determined.

Standards are analyzed as unknowns every 10 samples to check the variation and calibration of the analysis. Random and selected reruns are done to verify the data. The acceptable standard deviation for TOC is 3% variation from established value.

3. Rock Eval / HAWK Pyrolysis

Approximately 100 mg of washed, ground (60 mesh) whole rock sample is analyzed in the Rock-Eval or HAWK instrument. Organic rich samples are analyzed at reduced weights whenever the S2 value exceeds 40.0 mg/g or TOC exceeds 7-8%. Samples must be re-analyzed at lower weights when these values are obtained at 100 mg.

RE-II Operating Conditions

S1:	300°C for 3 minutes
S2:	300°C to 550°C at 25°C/min; hold at 550°C for 1 minute
S3:	trapped between 300 to 390°

RE-VI Operating Conditions

S1: 300°C for 3 minutes
S2: 300°C to 650°C at 25oC/min;
hold at 650°C for 0 minute
S3: measured between 300 to 400°

HAWK Operating Conditions

S1: 300°C for 3 minutes
S2: 300°C to 650°C at 25°C/min;
hold at 650°C for 0 minute
S3: measured between 300 to 400°

Measurements from Rock-Eval are:

S1: free oil content (mg HC/g rock)
S2: remaining generation potential (mg HC/g rock)
T_{max}: temperature at maximum evolution of S2 hydrocarbons (°C)
S3: organic carbon dioxide yield (mg CO_2/ g rock)

Several useful ratios are also utilized from Rock-Eval and TOC data. These are:

Hydrogen Index (HI):	S2/TOC x 100 (in mg HC/g TOC)
Oxygen Index (OI):	S3/TOC x 100 (in mg CO_2/g TOC)
Normalized Oil Content:	S1/TOC x 100 (in mg HC/g TOC)
S2/S3:	S2/S3 (in mg HC/CO_2)
Production Index (PI):	S1/ (S1+S2)

Instrument calibration is achieved using a rock standard. Its values were determined from a calibration curve to pure hydrocarbons of varying concentrations. This standard is analyzed every 10 samples as an unknown to check the instrument calibration. If the analysis of the 81 standard ran as an unknown does not meet specifications, those preceding data are rejected, the instrument recalibrated, and the samples analyzed again. However, normal variations in the standard are used to adjust any variation in the calibration response. The standard deviation is considered acceptable under the following guidelines:

T_{max}:	+/- 2°C
S1:	10% variation from established value
S2:	10% variation from established value
S3:	20% variation from established value

Analytical data are checked selectively and randomly. Selected and random checks are completed on approximately 10% of the samples. A standard is analyzed as an unknown every 10 samples.

4. Turnaround Time:

The standard turnaround time for sample orders over the past 12 months is approximately 2 to 3 weeks, depending on number of samples in the order.